NAVAL POSTGRADUATE SCHOOL

MONTEREY, CALIFORNIA

THESIS

THE COLD GAS-DYNAMIC SPRAY AND CHARACTERIZATION OF MICROCRYSTALLINE AND NANOCRYSTALLINE COPPER ALLOYS

by

William J. Marple

December 2012

Thesis Advisor:	Luke N. Brewer
Second Reader:	Sebastian Osswald

Approved for public release; distribution is unlimited

THIS PAGE INTENTIONALLY LEFT BLANK

REPORT DOCUMENTATION PAGE			Form Approved OMB No. 0704–0188

Public reporting burden for this collection of information is estimated to average 1 hour per response, including the time for reviewing instruction, searching existing data sources, gathering and maintaining the data needed, and completing and reviewing the collection of information. Send comments regarding this burden estimate or any other aspect of this collection of information, including suggestions for reducing this burden, to Washington headquarters Services, Directorate for Information Operations and Reports, 1215 Jefferson Davis Highway, Suite 1204, Arlington, VA 22202–4302, and to the Office of Management and Budget, Paperwork Reduction Project (0704–0188) Washington DC 20503.

1. AGENCY USE ONLY *(Leave blank)*	2. REPORT DATE December 2012	3. REPORT TYPE AND DATES COVERED Master's Thesis

4. TITLE AND SUBTITLE THE COLD GAS-DYNAMIC SPRAY AND CHARACTERIZATION OF MICROCRYSTALLINE AND NANOCRYSTALLINE COPPER ALLOYS	5. FUNDING NUMBERS JON: RPF5 ACCT: 1776445JON: BAAZV ACCT: 4473425
6. AUTHOR(S) William J. Marple	
7. PERFORMING ORGANIZATION NAME(S) AND ADDRESS(ES) Naval Postgraduate School Monterey, CA 93943–5000	8. PERFORMING ORGANIZATION REPORT NUMBER
9. SPONSORING /MONITORING AGENCY NAME(S) AND ADDRESS(ES) N/A	10. SPONSORING/MONITORING AGENCY REPORT NUMBER

11. SUPPLEMENTARY NOTES The views expressed in this thesis are those of the author and do not reflect the official policy or position of the Department of Defense or the U.S. Government. IRB Protocol number ____N/A____.

12a. DISTRIBUTION / AVAILABILITY STATEMENT Approved for public release; distribution is unlimited	12b. DISTRIBUTION CODE

13. ABSTRACT (maximum 200 words)

This thesis presents research on the cold gas-dynamic spray process—a relatively new technology that may be utilized to create metal coatings in the solid state. While the thermodynamics and fluid mechanics of the cold gas-dynamic spray process are well understood, the effects of feedstock powder microstructure and composition on the deposition process remain largely unknown. In particular, this thesis aims to shed light on these effects as they pertain to common face-centered cubic metals and their alloys—notably copper and brass. Deposition efficiency, coating thickness per pass, hardness, porosity and compositional variance were all characterized as functions of spraying pressure, spraying temperature and feedstock particle composition in each of the materials. This thesis presents evidence that while brass can be deposited using cold gas-dynamic spray, the resulting material does not possess a dense, uniform microstructure. In fact, deposits made with Cu-90/10 wt.% Zn brass have more than 400% more porosity than standard copper coatings, possess extensive microstructural cracking and wide compositional variance from grain to grain.

14. SUBJECT TERMS Cold spray, Cryomilling, Nanocrystalline, Copper, Brass, Stacking Fault Energy, Severe Plastic Deformation	15. NUMBER OF PAGES 117
	16. PRICE CODE

17. SECURITY CLASSIFICATION OF REPORT	18. SECURITY CLASSIFICATION OF THIS PAGE	19. SECURITY CLASSIFICATION OF ABSTRACT	20. LIMITATION OF ABSTRACT
Unclassified	Unclassified	Unclassified	UU

NSN 7540–01–280–5500 Standard Form 298 (Rev. 2–89)
Prescribed by ANSI Std. 239–18

THIS PAGE INTENTIONALLY LEFT BLANK

Approved for public release; distribution is unlimited

THE COLD GAS-DYNAMIC SPRAY AND CHARACTERIZATION OF MICROCRYSTALLINE AND NANOCRYSTALLINE COPPER ALLOYS

William J. Marple
Lieutenant, United States Navy
B.S., United States Naval Academy, 2008

Submitted in partial fulfillment of the
requirements for the degree of

MECHANICAL ENGINEER
AND
MASTER OF SCIENCE IN MECHANICAL ENGINEERING

from the

NAVAL POSTGRADUATE SCHOOL
December 2012

Author: William J. Marple

Approved by: Luke N. Brewer
Thesis Advisor

Sebastian Osswald
Second Reader

Knox T. Millsaps
Chair, Department of Mechanical and Aerospace Engineering

THIS PAGE INTENTIONALLY LEFT BLANK

ABSTRACT

This thesis presents research on the cold gas-dynamic spray process—a relatively new technology that may be utilized to create metal coatings in the solid state. While the thermodynamics and fluid mechanics of the cold gas-dynamic spray process are well understood, the effects of feedstock powder microstructure and composition on the deposition process remain largely unknown. In particular, this thesis aims to shed light on these effects as they pertain to common face-centered cubic metals and their alloys—notably copper and brass. Deposition efficiency, coating thickness per pass, hardness, porosity and compositional variance were all characterized as functions of spraying pressure, spraying temperature and feedstock particle composition in each of the materials. This thesis presents evidence that while brass can be deposited using cold gas-dynamic spray, the resulting material does not possess a dense, uniform microstructure. In fact, deposits made with Cu-90/10 wt.% Zn brass have more than 400% more porosity than standard copper coatings, possess extensive microstructural cracking and wide compositional variance from grain to grain.

THIS PAGE INTENTIONALLY LEFT BLANK

TABLE OF CONTENTS

I. INTRODUCTION....1
- A. MOTIVATION....1
- B. LITERATURE REVIEW....5
  - 1. The Cold Spray Deposition Process and Characteristics....5
  - 2. Utilizing Cu-Zn as a Model System for Understanding Cold Spray Deposition of FCC Alloys....10
  - 3. Cold Spray as a Method to Obtain Nanocrystalline Coatings....14
- C. HYPOTHESES....17
  - 1. Cold Spray of Microcrystalline Cu-Zn Alloys....17
  - 2. Cold Spray of Nanocrystalline Cu-Zn Alloys....17

II. EQUIPMENT INSTALLATION AND CALIBRATION....19
- A. INSTALLATION OF CENTERLINE (WINDSOR) SST MODEL SERIES C....19
- B. CALIBRATION OF CENTERLINE (WINDSOR) SST MODEL SERIES C....20
  - 1. THERMACH Powder Feeder....21
  - 2. Entraining Gas Flow....26
- C. COLD SPRAY DEPOSITION TESTING WITH THE MODEL SERIES C APPARATUS....27
  - 1. Powder Characterization, Experimental Setup, and Methodology....28
  - 2. Reproduction of the Benchmark Data Provided by Centerline SST....30
  - 3. Pressure and Temperature Relationships for Alumina/Aluminum Powder Mix....32
  - 4. The Effect of Pre-existing Substrate Roughness on Deposition Characteristics....34
  - 5. The Effect of Spray Nozzle Characteristics on Deposition....37

III. COLD SPRAY OF MICROCRYSTALLINE COPPER AND BRASS....43
- A. FEEDSTOCK POWDER CHARACTERIZATION....43
- B. EXPERIMENTAL METHODS....51
- C. RESULTS....55
  - 1. Deposition Efficiency and Coating Thickness Per Pass....55
  - 2. Deposit Hardness and Modulus of Elasticity....62
  - 3. Deposit Porosity....63
- D. DISCUSSION....67
  - 1. The Relationship between Deposition Efficiency and Changes in Pressure and Temperature....67
  - 2. The Effect on Zinc Content on Deposition Efficiency and Coating Thickness....71

3. The Relationships between Powder Zinc Content and Deposit Hardness and Modulus 73
4. The Relationship between Powder Zinc Content and Porosity 74
5. Compositional Variability as a Side Effect of the Cold Spray Deposition Process 76

IV. COLD SPRAY OF NANOCRYSTALLINE COPPER AND BRASS FEEDSTOCK POWDERS 81
A. FEEDSTOCK POWDER PREPARATION AND CHARACTERIZATION 81
B. EXPERIMENTAL METHOD 83
C. RESULTS 84
D. DISCUSSION 89

V. CONCLUSION 93
A. SUCCESSFUL INSTALLATION OF COLD SPRAY DEPOSITION SYSTEM AT NPS 93
B. SUCCESSFUL DEPOSITION OF BRASS 93
C. DEMONSTRATION OF COLD SPRAY OF CRYOMILLED COPPER AND BRASS 94

LIST OF REFERENCES 95

INITIAL DISTRIBUTION LIST 99

LIST OF FIGURES

Figure 1. Left: Damaged Ring Groove on Helicopter Mast Support, Right: Helicopter Mast Support Ring Groove after Repair with Cold Spray Deposition. From [2]. 3
Figure 2. Schematic of Cold Spray Process. From [2]. 5
Figure 3. Individual Particle after Impact with a Steel Substrate. From [15]. 6
Figure 4. Cross Sectional View of Cold Spray Coating. From [16]. 7
Figure 5. Copper Particle Velocity Distributions and their Associated Deposition Efficiencies. From [24]. 8
Figure 6. Cu-Zn Phase Diagram. From [31]. 13
Figure 7. Centerline SST Series C Cold Spray Apparatus at the Naval Postgraduate School. 20
Figure 8. Powder Feeder Air Flow Meter by King Instrument Company. 21
Figure 9. THERMACH Powder Feeder Vibrational Impactor Speed [RPM] Example. 22
Figure 10. Centerline SST Model Series Control Panel Interface. 23
Figure 11. Calibration Curves for Thermach Powder Feeder and SST Series C Control Panel [Pure Aluminum]. 24
Figure 12. Calibration Curves for Thermach Powder Feeder and SST Series C Control Panel [Pure Copper]. 24
Figure 13. Calibration Curves for Thermach Powder Feeder and SST Series C Control Panel [90–10wt.% Cu-Zn]. 25
Figure 14. Calibration Curves for Thermach Powder Feeder and SST Series C Control Panel [80–20wt.% Cu-Zn]. 25
Figure 15. Calibration Curves for Thermach Powder Feeder and SST Series C Control Panel [70–30wt.% Cu-Zn]. 26
Figure 16. Flow Chart of Equipment Gas Flows During Operation. 27
Figure 17. SEM Photograph of SST-A0050 [50 wt.% Aluminum/50 wt.% Alumina] Powder. From Centerline SST. 29
Figure 18. Cold Spray Deposition Pattern. 30
Figure 19. Deposition Efficiency and Coating Thickness Per Pass Vs. Spray Pressure for SST-A0050. 32
Figure 20. Deposition Efficiency Vs. Spray Temperature and Spray Pressure for SST-A0050. 33
Figure 21. Photograph of the Process of Modifying the Nozzle Stand-Off Distance. 37
Figure 22. Deposition Efficiency and Coating Thickness per Pass Vs. Nozzle Stand-off Distance for SST-A0050. 38
Figure 23. Non-Dimensional Chart Showing the Effect of Stand-Off Distance on Deposition Efficiency. From Pattison et al. [41]. 39
Figure 24. SEM Surface Photographs (1000x).Clockwise from Top Left: Pure Copper Powder, Cu-90/10 wt.% Zn, Cu-80/20 wt.% Zn and Cu-70/30 wt.% Zn. 45

Figure 25. Output X-Ray Spectra, Counts Vs. Energy, for Cu-90/10 wt.% Zn Deposit, Sprayed at 250 psi and 450 °C. 47
Figure 26. SEM Cross-Sectional Photographs (1000x) of the As Received Brass Powders, Clockwise from Top Left: Cu-90/10 wt.% Zn, Cu-80/20 wt.% Zn, Cu-70/30 wt.% Zn. 49
Figure 27. Left: Zinc X-Ray Counts / Copper X-Ray Counts vs. Distance, As Received Cu-70/30 wt.% Zn Powder. Right: Line Map from which Data on the Left was Retrieved. 49
Figure 28. Cross-Sectional Spectrograph Maps and SEM Image (1000x) for Cu-90/10 wt.% Zn Powder, As Received. Top Center: SEM Image. Bottom Left: Cu X-Ray Elemental Map. Bottom Right: Zn X-Ray Elemental Map.....50
Figure 29. Cross-Sectional Spectrograph Maps and SEM Image (1000x) for Cu-70/30 wt.% Zn Powder, As Received. Top Center: SEM Image. Bottom Left: Cu X-ray Elemental Map. Bottom Right: Zn X-ray Elemental Map. 51
Figure 30. Left: Optical Image of Pure Copper Deposit (Sprayed at 250 psi, 450 °C). Right: Sample of ImageJ Porosity Analysis on the Same Deposit. 55
Figure 31. Deposition Efficiency and Coating Thickness Vs. Zinc Content by wt.%, with a Spray Pressure of 250 psi and a Spray Temperature of 450 °C. 58
Figure 32. Deposition Efficiency and Coating Thickness Vs. Zinc Content by wt.%, with a Spray Pressure of 250 psi and a Spray Temperature of 300 °C. 58
Figure 33. Three Dimensional Surface Plot of Deposition Efficiency Vs. Spray Pressure and Temperature for Pure Copper Powder. 60
Figure 34. Three Dimensional Surface Plot of Deposition Efficiency Vs. Spray Pressure and Temperature for Cu-90/10 wt.% Zn Powder. 60
Figure 35. Three Dimensional Surface Plot of Deposition Efficiency Vs. Spray Pressure and Temperature for Cu-80/20 wt.% Zn Powder. 61
Figure 36. Three Dimensional Surface Plot of Deposition Efficiency Vs. Spray Pressure and Temperature for Cu-70/30 wt.% Zn Powder. 61
Figure 37. Average Hardness Vs. Zinc Content by wt.% for Deposits Sprayed at 250 psi and 450 °C, and 250 psi and 300 °C. 63
Figure 38. Average Young's Modulus Vs. Zinc Content by wt.% for Deposits Sprayed at 250 psi and 450 °C, and 250 psi and 300 °C. 63
Figure 39. Optical Microscopy Photos of Pure Copper Spray Deposits, Mag 25X. Left: 250 psi, 450 °C. Right: 250 psi, 300 °C. 64
Figure 40. Optical Microscopy Photos of Cu-90/10 wt.% Zn Spray Deposits, Mag 25X. Left: 250 psi, 450 °C. Right: 250 psi, 300 °C. 64
Figure 41. Optical Microscopy Photos of Cu-80/20 wt.% Zn Spray Deposits, Mag 25X. Left: 250 psi, 450 °C. Right: 250 psi, 300 °C. 65
Figure 42. Optical Microscopy Photos of Cu-70/30 wt.% Zn Spray Deposits, Mag 25X. Left: 250 psi, 450 °C. Right: 250 psi, 300 °C. 65
Figure 43. SEM Photos of Cold Spray Deposits, sprayed at 250 psi, 450 °C, Mag 200X. Clockwise from Top Left: Pure Copper, Cu-90/10 wt.% Zn, Cu-80/20 wt.% Zn, Cu-70/30 wt.% Zn. 66
Figure 44. Coating Porosity Vs. Zinc Content by wt.%. 67

Figure 45. Optical Photographs of Deposit/Substrate Interface, Showing Cracking at Higher Spray Temperatures, (100x). Top Left: Cu-90/10 wt.% Zn (250 psi, 450 °C). Top Right: Cu-90/10 wt.% Zn (250 psi, 300 °C). Bottom Left: Cu-80/20 wt.% Zn (250 psi, 450 °C). Bottom Right: Cu-80/20 wt.% Zn (250 psi, 300 °C). 69
Figure 46. Brittle-Type Microstructural Cracking in the Vicinity of Deposit/Deposit Interface Gaps, (100x). Left: Cu-80/20 wt.% Zn Sprayed at 250 psi [1.72 MPa] and 300 °C. Right: Cu-70/30 wt.% Zn Sprayed at 250 psi [1.72 MPa] and 450 °C.....71
Figure 47. Cu-90/10 wt.% Zn Deposit Sprayed at 250 psi [1.72 MPa] and 450 °C. Left: SEM Photograph, 500x. Right: Zinc Composition Map, 500x.....77
Figure 48. Cu-80/20 wt.% Zn Deposit Sprayed at 250 psi [1.72 MPa] and 450 °C. Left: SEM Photograph, 500x. Right: Zinc Composition Map, 500x.....78
Figure 49. Cu-70/30 wt.% Zn Deposit Sprayed at 250 psi [1.72 MPa] and 450 °C. Left: SEM Photograph, 500x. Right: Zinc Composition Map, 500x.....78
Figure 50. Microhardness vs. Cryomilling Time. From [40].....82
Figure 51. Crystallite Size Vs. Cryomilling Time. From [40]. 82
Figure 52. SEM Photographs of Cryomilled Deposits Sprayed at 250 psi [1.72 MPa] and 450 °C, 250x Magnification Left: Pure Copper. Right: Cu-90/10 wt.% Zn. 85
Figure 53. SEM Photographs of Cryomilled Deposits Sprayed at 250 psi [1.72 MPa] and 450 °C, 500x Magnification. Left: Pure Copper. Right: Cu-90/10 wt.% Zn.....85
Figure 54. Nano-indentation Results for Cryomilled Copper Powder Deposit. Top: Hardness. Bottom: Modulus of Elasticity.....87
Figure 55. Nano-indentation Results for Cryomilled Cu-90/10 wt.% Zn Powder Deposit. Top: Hardness. Bottom: Modulus of Elasticity.....88

THIS PAGE INTENTIONALLY LEFT BLANK

LIST OF TABLES

Table 1. Reference Spray Data from Centerline SST for Series C with SST-A0050 [50.wt% Aluminum/50 wt.% Alumina] Powder, April 2009. After Centerline SST. 31
Table 2. Obtained Spray Data for Series C with SST-A0050 [50.wt% Alumina/50 wt.% Aluminum]....31
Table 3. Deposition Efficiency and Coating Thickness per Pass for a Sandblasted Substrate and a Smooth Substrate in Otherwise Common Spray Setups. 35
Table 4. Deposition Efficiency and Coating Thickness vs. Nozzle Stand-Off Distance for SST-A0050 [50.wt% Alumina/50 wt.% Aluminum]. 38
Table 5. Modification of Nozzle Type for Series C with SST-A0050 [50.wt% Alumina/50 wt.% Aluminum]. 41
Table 6. Sieve and Batch Composition Analysis for Pure Copper, Cu-90/10 wt.%, Cu-80/20 wt.% and Cu-70/30 wt.% Zn Powders. From ACu Powder [44]....44
Table 7. Observed Mean Particle Size and Composition for Each Powder, As Received....46
Table 8. The Melting Points of Copper, Cu-90/10 wt.% Zn, Cu-80/20 wt.% Zn and Cu-70/30 wt.% Zn....52
Table 9. Cold Spray Parameters Utilized During Copper and Brass Experiments....52
Table 10. Spray Data for Pure Copper Powder....56
Table 11. Spray Data for Cu-90/10 wt.% Zn Powder....56
Table 12. Spray Data for Cu-80/20 wt.% Zn Powder....57
Table 13. Spray Data for Cu-70/30 wt.% Zn Powder....57
Table 14. Hardness and Young's Modulus for Pure Copper, Cu-90/10 wt.% Zn, Cu-80/20 wt.% Zn and Cu-70/30 wt.% Zn Deposits....62
Table 15. Spray Data for Porosity in Pure Copper, Cu-90/10 wt.% Zn, Cu-80/20 wt.% Zn and Cu-70/30 wt.% Zn Cold Spray Deposits....66
Table 16. Multi-Point X-ray Data and Statistics for Cu-90/10 wt.% Zn and Cu-80/20 wt.% Zn deposits....77

THIS PAGE INTENTIONALLY LEFT BLANK

ACKNOWLEDGMENTS

I would like to thank Professor Douglas Seivwright and Dr. Chanman Park of the Naval Postgraduate School faculty for their incalculable effort and help with respect to the installation of the Centerline Cold Spray Model Series C equipment. Without the steadfast generosity of their time and expertise, the machinery would likely have never worked.

Additionally, I am indebted to Professor Joe Hooper and Prof. Sebastian Osswald, both of the Naval Postgraduate School, for their consistent guidance with my project and for their insightful wisdom into the proper planning and consideration of my thesis work.

Likewise, I am grateful to Professor Luke N. Brewer, also of Naval Postgraduate School, for his never-ending support—both when I desired it and when I did not desire it. I could not have written a coherent thesis without his constant presence in my work and in my graduate education—assuredly, I am a better engineer and military officer because of him.

I would also like to extend my gratitude to Dr. Dong Jin Woo of the Naval Postgraduate School. He was instrumental in helping me learn to operate the equipment used during the research presented in this thesis and dedicated multiple afternoons to provide support to my work.

Still further, I am indebted to Ian Ward, the West Region sales manager of ACu Powder, for his and his team's consistently superb customer service, as well as their steadfast attention to detail with respect to their documentation. Additionally, they demonstrated exceptional professionalism over a period of months by ensuring that we possessed all the tools necessary to our work—a rarity for a business that has already shipped their product out the door.

And last, I would like to thank the Office of Naval Research and the Naval Postgraduate School itself for providing the funding for this research.

THIS PAGE INTENTIONALLY LEFT BLANK

I. INTRODUCTION

A. MOTIVATION

In the modern world of metallurgy as it portends to mechanical components in operation, there are only two constants—occasional mechanical failures and the ever-steady threat from corrosion. These concerns are serious for the engineer and the operator—surface-based electrochemical corrosion, pitting and galvanic corrosion all can over time render mechanical components useless, or at the least impair their performance, and mechanical damage often will ruin the integrity of the component and prevent the part from performing its designed function. Over the years, a multitude of processes have been invented and optimized to allow for engineers and operators to prevent the occurrence of these constants in some cases, and to mitigate their effects in others. Regardless of these efforts however, components still corrode and they still exhibit structural failure at times—thus there exists an ever-pressing need for the ability to repair such structures to normal operating characteristics.

In modern engineering, it reasonably can be argued that the most reliable way to limit the corrosion of components made of metal and avoid the corresponding negative side effects is to apply a relatively thin surface coating to the material for which protection is desired. The reason surface coatings are often the most economical or practical manner by which corrosion can be combated is rather simple: In many cases, passivation via metallurgical composition choice is impossible—considerations other than those regarding corrosion such as cost or weight may dominate the design process and prevent the use of such materials. Generally speaking, the surface coating will be made from a material that limits the potential for corrosion to occur, while additionally maintaining the required performance characteristics of the component.

The potential uses for any such coatings that can be produced are quite large however, and are not limited strictly to corrosion protection. Surface coatings are employed equally well to increase mechanical durability and wear resistance—say, for instance, in bearings. They can also be used to create components that yield significantly

different thermal or electrical conductivities than the structural material underneath would yield. Such coatings could possibly be used, for instance, to create electrically conductive mechanical components, or could be used to create coatings that acted as a thermal insulator for the underlying component material, possibly inhibiting creep in a high temperature environment.

In particular, cold spray deposition is a promising technique for applying corrosion and wear-resistant coatings. Cold spray deposition is a process by which micron-sized metal powder particles are entrained in a heated supersonic gas flow, and then deposited upon a desired surface by means of ballistic impingement. Via cold spray, a multitude of coating materials can successfully be deposited onto a similarly large number of substrate materials at arbitrary thicknesses—chosen by the design engineer according the requirements. In 2011 DeForce et al. explored the utilization of cold spray to deposit Al-5 wt.% Mg coatings for the protection of magnesium alloys from corrosion, ultimately demonstrating that the cold spray process was indeed viable for producing corrosion-resistant coatings on ZE41A-T5 magnesium alloys. Coatings were produced that were significantly harder than the underlying material, had sufficient adhesion strength to the underlying material, and, furthermore, were galvanically compatible with the magnesium underneath [1].

Going further than corrosion and addressing the problems of mechanical failure, our second concern when considering mechanical components, cold spray deposition can be used to repair damaged material by replacing material loss due to corrosion or mechanical cracks in parts which have already failed—restoring them to operation. Repairing components, vice scrapping them and purchasing new ones, can save an incredible amount of money—a huge consideration for the Department of Defense in the current budgetary environment. Beyond cost considerations though, repairing components can minimize downtime of the operational unit, sometimes a larger concern than even cost. And last, by repairing mechanical parts vice replacing them, it is possible to minimize the scope of and the strain experienced by the supply chain—all the way from industry to the maintenance facility—restraining the need for warehouse space, supply personnel and delivery services.

Several authors have recently demonstrated the utility of cold spray deposition for the repair of mechanical parts. For instance, P. F. Leyman and V. K. Champagne showed conclusively in 2009 that cold spray system could be used to repair damaged 7075-T73 aluminum mast supports used in U. S. Army rotorcraft [2]. More than 50 mast supports had been rendered unusable by either pitting corrosion or by mechanical damage. Furthermore, the mast supports were completely unserviceable by any known method or process—essentially, the entire component was scrapped by the damage, requiring the purchase of new mast supports in order to keep the unit operational. Removing the damaged piece of the component, utilizing cold spray deposition to refill the damaged piece and then machining the support mast back to original specifications allowed for the reclamation of the component as a whole. A picture of the helicopter mast support before and after repair with cold spray deposition can be found in Figure 1. Likewise, in 2010, J. Villafuerte of CenterLine Windsor Ltd. and D. Wright of Accuwright Industries were able to practically demonstrate that in addition to aluminum alloys, aircraft components made from magnesium alloys could be repaired, re-machined and put back into service — meeting all FAA requirements [3]. A number of aluminum alloys were successfully used in this process, including AA6061 and AA7075, as well as other more exotic aluminum alloys.

Figure 1. Left: Damaged Ring Groove on Helicopter Mast Support, Right: Helicopter Mast Support Ring Groove after Repair with Cold Spray Deposition. From [2].

Cold spray deposition has been a focus of recent research because in both the creation of surface coatings and in the repair of mechanical failures, it has generally been recognized that traditional thermal spray (TS) (which includes techniques such as High Velocity Oxygen Fuel [HVOF] Spray, Plasma Spray and Wire Arc Spray) and classic welding have potentially serious shortcomings, either from a mechanical or an economical standpoint. Situations where conventional TS or welding is unacceptable include when high temperatures cannot be tolerated by the substrate, specific microstructural and mechanical properties in the feedstock are required to be retained in the coating, oxidation protection is necessary, ultra-thick coatings are needed, residual stresses must be eliminated from the final product and extremely high-density coatings are necessary.

Cold spray deposition offers a number of unique advantages over traditional techniques because during cold spray the material temperature is always at levels well below the melting point of the feedstock material. As a matter of fact, the term “cold spray” was originally given to the process due to the relatively low temperatures of the expanded gas stream that exits the nozzle in comparison to thermal spray. Due to the significantly lower temperature of the feedstock material during the deposition process, the adhesion of the feedstock material to the substrate as well as the cohesion of the deposited material is accomplished in the solid state [4]. As such, cold spray offers a unique advantage in that there is the possibility of retaining the microstructure and the mechanical properties of the particle feedstock. Furthermore, cold spray offers a number of additional advantages. First, thermal oxidation during spray deposition is mostly evaded; therefore, cold spray produces coatings that are more durable with better bond strength. Likewise, due to the low temperatures at which the coatings are deposited on the substrate, the formation of residual stress is largely avoided, especially at the interface between the substrate and the coating. Avoiding large residual stresses is critical because they often cause debonding of the deposited coating. This problem is compounded when the substrate material is different from the coating material. Still further, the shock-dominated physics of particle impacts during cold spray, gives rise to “material mixing at the interface and providing mechanical interlocking between the two materials [5].” Last,

in comparison with other thermal spray coatings, “deposits produced by cold spray are characterized by being less porous, having higher hardness and lower oxide concentration, and the Young’s moduli of cold spray deposits can be greater than 80% of bulk feedstock values [6].”

Given the distinct advantages that cold spray deposition offers as an industrial process, it can easily be inferred that such a process could greatly benefit the Navy and its associated contractors, given the scale and scope of high performance materials the naval environment demands—on and underneath the sea, as well as in the air. The Navy is constantly searching for new processes and techniques which can improve construction and repair capabilities while minimizing costs, complexity and time.

B. LITERATURE REVIEW

1. The Cold Spray Deposition Process and Characteristics

Cold spray (CS) is a process whereby metal powder particles are entrained in a supersonic jet of heated gas and utilized to form a coating by means of ballistic impingement upon a suitable substrate [4, 7–9]. A schematic of this process can be found in Figure 2.

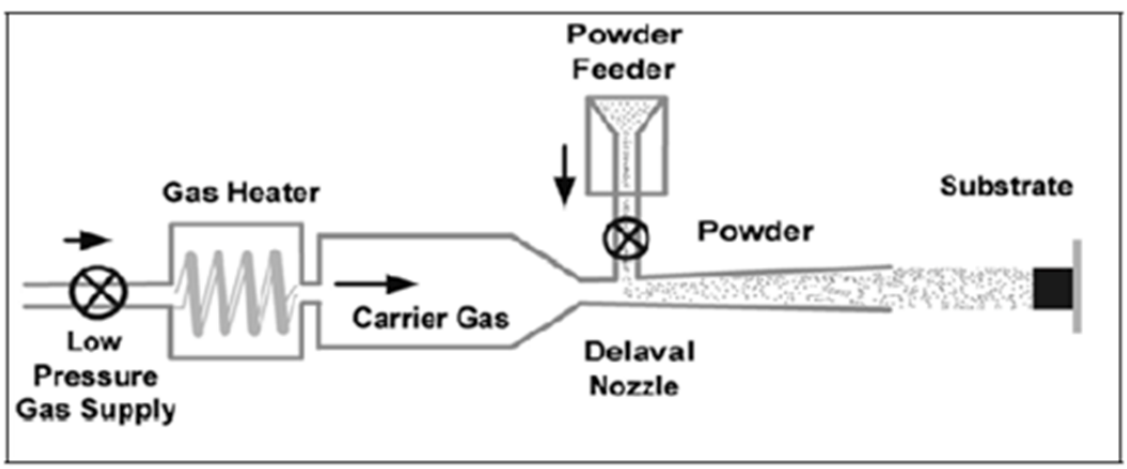

Figure 2. Schematic of Cold Spray Process. From [2].

The metal powders range in particle size from 5 to 50 microns and are accelerated by injection into a high-velocity stream of gas. The high-velocity gas stream is generated through the expansion of a pressurized, preheated gas through a de-Laval type converging-diverging nozzle. During expansion the gas flow is accelerated to supersonic velocities, with an accompanying decrease in pressure and temperature [10–12].

The powder particles, initially carried by a separate gas stream, are injected into the nozzle either prior to the throat or downstream of the throat. The particles are then accelerated by the main nozzle gas flow and are impacted upon a substrate after exiting the nozzle. Upon impact, the solid particles de-form and create a bond with the substrate. As the process continues, particles continue to impact the substrate and form bonds with the deposited material, resulting in a uniform coating with very little porosity and high bonding strength [13, 14]. A visual example of the de-formation and bonding experienced by a single powder particle can be seen in Figure 3 and a cross sectional view of a cold spray deposition coating can be found in Figure 4.

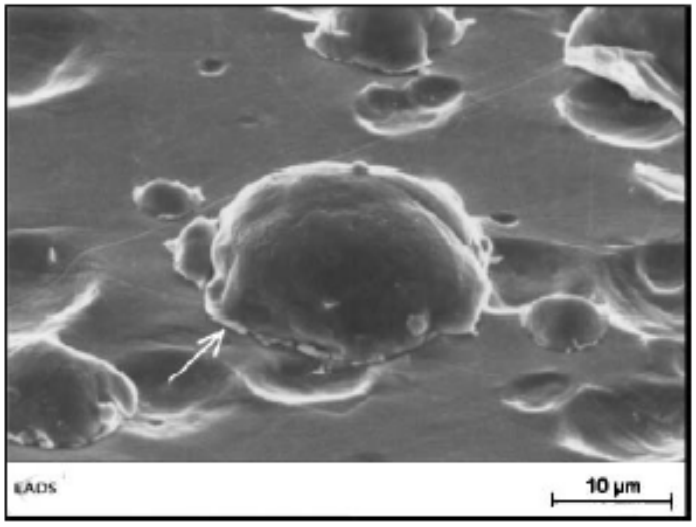

Figure 3. Individual Particle after Impact with a Steel Substrate. From [15].

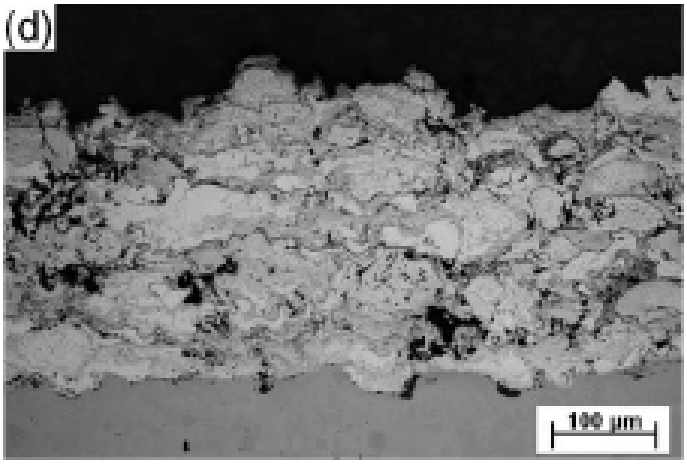

Figure 4. Cross Sectional View of Cold Spray Coating. From [16].

Cold spray was introduced to North America at the laboratory scale in the 1990s, and a U.S. patent was issued in 1994 (U.S. Patent No. 5, 302,414 [1994]) [17–20]. Cold spray deposition was initially developed, however, in the mid 1980's in the Soviet Union at the Institute for Theoretical and Applied Mechanics of the Siberian Division of the Russian Academy of Science in Novosibirsk. Interestingly enough, research of the process began as an offshoot of supersonic wind tunnel testing [21–23]. During experiments there in a supersonic wind tunnel with a particle-leaded flow, it was discovered that, from a particular particle velocity onwards, the abrasive effect of the particles reverses to an adhesion, and that this effect is in fact assisted by a rise in gas temperature.

This finite velocity is known as the critical velocity, and is paramount to the discussion of cold spray deposition as a process. If a particle is traveling above this critical velocity, then it will deposit and if it is travelling slower, it will simply bounce off—thus, if larger numbers of particles are travelling at speeds above the critical velocity, deposition efficiency will be significantly improved. Further, knowing the critical velocity for a specific powder will enable the operator to possess foreknowledge of the approximate deposition efficiency to be expected prior to the act of creating the coating [24, 25]. A graph constructed via experimentation with the deposition of copper powder by Gilmore et al. can be found in Figure 5 which demonstrates quantitatively the importance of the particle velocity in reference to the critical velocity on deposition

efficiency. This data shows that for copper deposition using helium gas at a temperature of 300C, the critical velocity is approximately 600m/s.

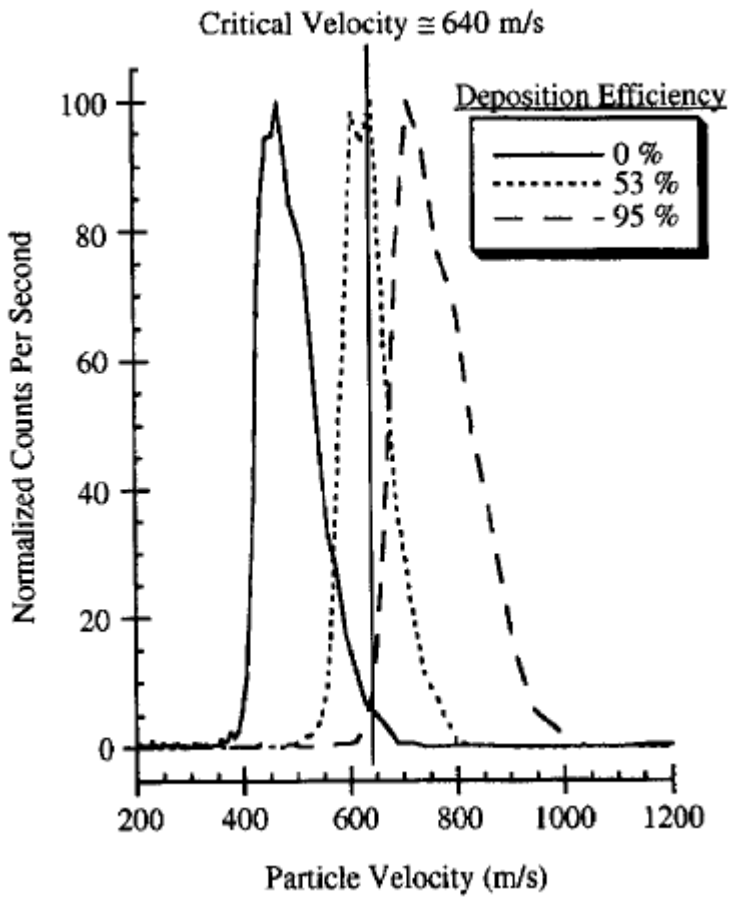

Figure 5. Copper Particle Velocity Distributions and their Associated Deposition Efficiencies. From [24].

There are a number of process parameters which can be controlled during the cold spray process, all of which have a direct effect on the efficiency of deposition and on the quality of the sprayed material. Generally speaking these cause and effect relationships hold true regardless of the feedstock material—the only exception is particle hardness, which is a direct attribute of the feedstock material. The parameters which may be manipulated can be grouped into three separate categories. First there is the thermodynamic conditions & characteristics of the spray including: molecular weight of the entraining gas, entraining gas flow pressure, entraining gas flow temperature, distance

from the nozzle apparatus to the substrate, and nozzle design. There are also key feedstock powder characteristics: particle size, particle morphology, and particle hardness. Lastly, there is the nature of the substrate which includes: substrate hardness and substrate temperature. Victor K. Champagne's book "The Cold Spray Materials Deposition Process" provides an extensive review of this information and a full reference list for the discussion of these parameters and their effects on the cold spray process in general and on the characteristics of the final coating [26].

The relative importance of these key cold spray process parameters has been thoroughly explored and documented for pure aluminum and copper materials. In addition, some work on aluminum alloys has also been performed. There are over one hundred papers thus far devoted to the study of cold spray with copper and aluminum used as the feedstock powders. Of these papers, it is particularly the ones that deal with copper that provide the background for this thesis.

With respect to copper in the pure form, the literature is rather extensive [6, 16, 27–30]. Cold spray deposition was demonstrated to be effective and to be perhaps more effective than thermal spray by Stoltenhoff et al. in 2006. During their experiments both helium and nitrogen were used as spraying gas, and relatively common spraying pressures, temperatures, and particle size and morphologies were used to allow for comparison with previous results in other materials. Basic parameters of copper cold spray coatings were obtained including hardness, bond strength, porosity, electrical conductivity, deposition efficiency and coating microstructure. Additionally the group presented discussion regarding annealing after the cold spray process and how such annealing affected the final microstructure and properties of the copper coating. In summary, this paper provides a solid benchmark for what to expect in cold spray deposited copper coatings based on common spray parameters. Ning et al. delved into the effects of powder properties on in-flight particle velocity and deposition effects in copper powders utilizing a low pressure cold spray process, with an entraining gas pressure of seven bars. In this paper a comprehensive estimation of the critical velocity of copper was made using the SprayWatch system and deposition efficiency was recorded for three different types of copper feedstock powder. These estimations of critical velocity allow

the operator to quantitatively adjust spray parameters before engaging in the cold spray process to best affect the final coating product as desired. Koivuluoto et al. presented work in 2007, which discussed the microstructure of copper cold sprayed coatings in depth. In their work, three different types of copper feedstock powders—in terms of microstructure—were used in order to provide comparison between different powder microstructures and their according effects on the final coating product—they found that copper produced dense coatings, but with occasional micro-voids in between splats. Heat treatment was also done on some of the samples to expand the value of the work. Additionally coating porosity and the corrosion characteristics of the coatings were studied as well—these characteristics were crucial for the authors to understand well because by their reasoning, ostensibly the reason why copper would be used in a coating would be to provide a material with excellent electrical conductivity and/or corrosion resistance.

2. Utilizing Cu-Zn as a Model System for Understanding Cold Spray Deposition of FCC Alloys

A casual search of the literature and academic databases will yield a significant amount of knowledge pertaining to the spray of copper in its pure from, as mentioned previously.

However, it should be noted that this knowledge is largely of engineering use. For example, the conclusions that can be found in the literature often read something like the following: if the user sprays at this temperature, these types of coating characteristics will emerge. Or with regard to material selection: the spray of highly alloyed steel does not lend itself to success when using the cold spray deposition method. The initial conditions and the end result are incredibly well understood, and the methods by which the process may be modified are also similarly well understood.

Despite the progress in its application, there is still little fundamental understanding of the exact science behind the cold spray method, particularly surrounding how the microstructure of the starting powder material influences its ability

to be sprayed. Many questions surrounding the microstructure-processing-final microstructure relationships remain to be answered:

- *If a material has substitutional alloying agents added, but is sprayed at a higher temperature, which relationship will dominate the process in comparison to the controlled example, and more importantly, why?*
- *How does substrate temperature vary as a control point if we vary the substrate material?*
- *Is it more important for low melting point substances?*

This thesis uses the binary alloy Cu-Zn as a model system for beginning to answer some of these questions. Copper in the pure form has already had extensive research performed with respect to the spray and deposition of the material, lending a wonderful starting point for research—and provides extensive comparative points in the literature for the results. By contrast, there are no open-literature reports of the cold spray deposition of brass alloys. Copper and zinc form a simple, substitutional solid solution with a single phase region for concentrations of less than thirty-five percent zinc by weight, as seen in Figure 6 below (obtained from ASM International, but original reference listed) [31]. In addition, the melting point of the alloy decreases with increasing zinc content, possibly lending insight into whether or not particle melting point has an impact on the deposition process. Lastly, the brass alloys are known for having low stacking fault energies which give rise to large strain hardening coefficients, a property that will give insight to the fundamental mechanics responsible for particle bonding.

Stacking faults as defined in materials science are essentially interruptions in the naturally occurring stacking sequence that occurs in all crystal structures, including those of metals. Stacking faults are the direct and observable result of dislocations—crystallographic defects or irregularities in a crystal structure. Because stacking faults decrease the amount of order within a crystal structure, they carry an associated energy penalty with them.

In many occasions, a perfect dislocation—which would yield a single stacking fault—dissociates into two partial dislocations, which tend to repel each other. This

creates a stacking fault with a particular width, instead of the infinitesimally thin (a single plane of atoms thick) stacking fault associated with perfect dislocations. The width of the stacking fault in this case is directly attributed to the value of the stacking fault energy (SFE) of that particular material. There must be an energy balance between the repulsive force that exists between two separate partial dislocations, and the attractive force which exists as a consequence of the surface tension created by the stacking fault itself. The net quantity of energy which remains after the summation of these opposing forces is the quantitative value of the SFE of the material in study. More simply put, SFE is the energy penalty which is paid to create a stacking fault in a crystal structure—a material property which is unique in every material.

When SFE is low, such as in Cu-Zn alloys, wider stacking faults occur because there is a smaller energy penalty to be paid for the associated defect in the crystal structure. These defects in the crystal structure prevent the movement of dislocations via the processes of cross-slip and climb—thus low SFE materials have the capacity to become very hard and brittle when cold worked.

When SFE is high, such as in aluminum, it becomes exceedingly difficult for a perfect dislocation to dissociate into two partial dislocations, and as such the material tends to deform only via dislocation glide. If dissociation into two partial dislocations does occur, then the stacking fault tends to be very thin, and carries a significant amount of energy within the fault. Because these materials leave cross slip and climb relatively unhindered as manners to achieve dislocation motion, cold work does not impart as strong of an effect on the hardness and brittleness of the material as seen in low-SFE materials.

Warren et al., Smallman et al., and Wagner effectively proved this concept and it's applicability to Cu and Cu-Zn alloys over half a century ago [32–34]. Via analysis of the cold working process it was estimated that the SFE's of Cu, Cu-10wt.%Zn, Cu-20wt.%Zn and Cu-30wt.%Zn were 74 mJm^{-2}, 60 $mJm^{-2,}$ 20 mJm^{-2} and 6 mJm^{-2}, respectively. Essentially, as more Zn is added by wt.% in a Cu-Zn alloy, the SFE energy decreases—and further decreases to an extremely low level.

As such, we can reasonably and logically deduce that as more Zn is added by wt.% to Cu in brass, that a larger number of and wider stacking faults will be present given the same number of dislocations in the crystal, and this will inhibit movement of dislocations during the cold work process. Accordingly, it would be rational to assume that cold worked Cu-Zn alloys will be significantly harder and crystallite size will be significantly smaller than those values found in pure Cu cold worked samples, with the disparity between the two increasing with larger amounts of added Zn. Logically, from these statements we can conclude that cold spray, the process of which severely plastically deforms the material and creates a large amount of dislocations, will create very hard coatings from materials with low SFE's—and it is possible that the particles will be so hard that either the deposition or the final coating is impacted negatively.

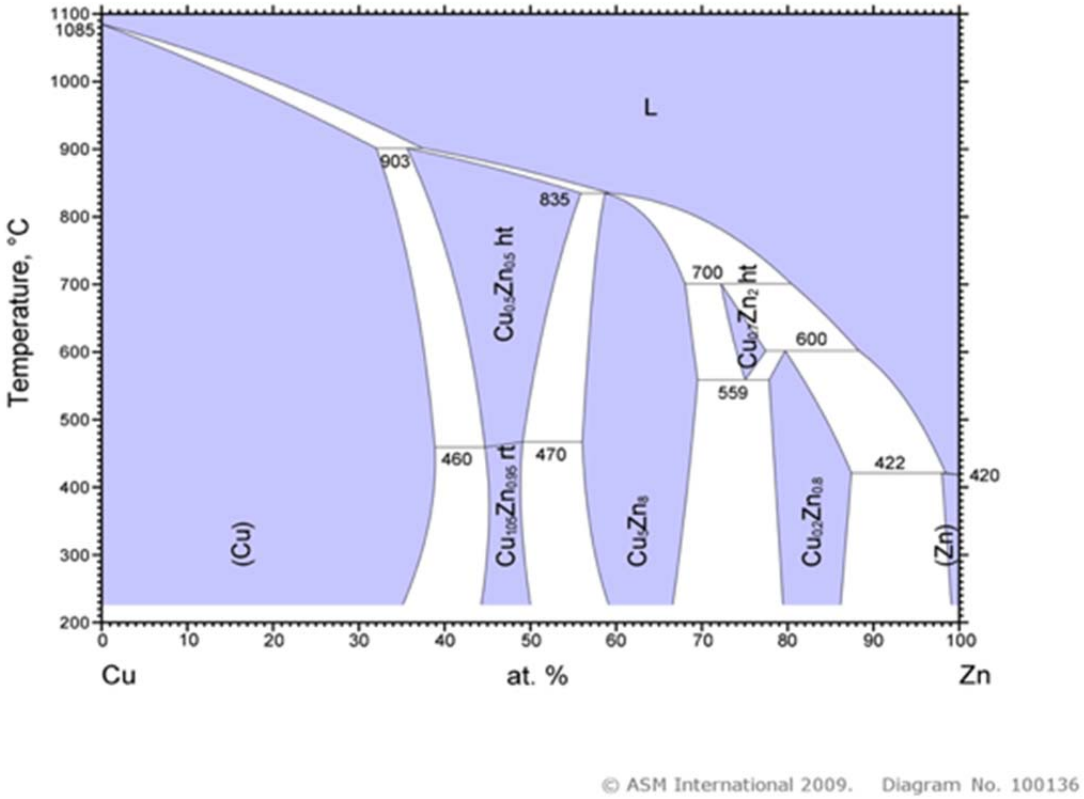

Figure 6. Cu-Zn Phase Diagram. From [31].

3. Cold Spray as a Method to Obtain Nanocrystalline Coatings

It is well known and understood that nanocrystalline materials possess increased hardness and strength compared with typical materials, and there is therefore much to be desired in very hard and strong cold sprayed coatings. Thus research into nanocrystalline cold sprayed coatings has been a relatively new but active area of interest.

Nanocrystalline aluminum was utilized in the cold spray process by Ajdelsztajn et al. in 2005, and the coating produced with this enhanced microstructure was compared directly to the coatings produced by the conventional microstructure [35]. It was determined that coating hardness could indeed be substantially increased via the use of nanocrystalline powder feedstock, but the use of such material also resulted in a substantially higher porosity with decreased density—a product of the increased hardness of the feedstock powder which limited the ability of the powder to deform on impact with the substrate, thus creating a bond between the powder and substrate.

Hall et al. in 2005 accomplished the same task of consolidating nanocrystalline aluminum via utilization of the cold spray deposition process, albeit with slightly different spray parameters and powder characteristics [36]. The same observations were made regarding porosity in nanocrystalline cold spray coatings, but during the course of their research, Hall et al. noticed significant grain refinement in their final coatings as a product of the cold spray process, in contrast to Ajdelsztajn et al. who noted a lack of grain refinement. The cause of this grain refinement in Hall et al.'s research was attributed to the significantly higher particle velocity—a product of their differing operating parameters.

In 2011, Zhang et al. prepared aluminum coatings using a mixture of nanocrystalline aluminum powder and conventional atomized aluminum feedstock powder [37]. The goal of this research was to produce a coating which has substantially higher hardness and strength like those found in the previously mentioned papers, but with a smaller impact on the porosity of the coating. Zhang et al. used the same materials and process utilized by Ajdelsztajn et al. so that direct comparison could be made with the previous experiment. In conclusion, it was found that a mixture of conventional

atomized and nanocrystalline aluminum powders allowed for the creation of coatings with similar although slightly lower densities and higher porosities, but even further higher strength than that found in previous work which utilized strictly nanocrystalline feedstock. This was explained by Zhang et al. as the product of similar microstructure in aggregate between all nanocrystalline and the mixed powder coatings, but far lower amounts of porosity in the mixed powder coating.

Recently research was conducted by Liu et al. at the University of Science and Technology in Beijing where instead of aluminum, nanocrystalline copper was studied as a feedstock material for the cold spray deposition process [38]. Similar results were found as those found in the aluminum studies mentioned previously. The hardness and strength of the nanocrystalline copper coating deposit were nearly twice as high as that found in the conventional copper powder cold sprayed deposit. However, no discussion of coating density or porosity was conducted by Liu et al., so our understanding of the properties of nanocrystalline copper coatings is limited in contrast to Ajdelsztajn et al., Zhang et al. and their discussion into the feasibility and properties of nanocrystalline aluminum coatings.

Although research into the use of nanocrystalline powders for cold spray applications remains in relative infant stages, it has been demonstrated that nanocrystalline feedstock powders can be used successfully in the cold spray process to dramatically increase the hardness and strength of cold sprayed coatings—at least in the two most commonly studied materials, copper and aluminum. This could possibly lead to coatings which could fill needs for specific applications requiring increased hardness, such as in armors or in bearing surfaces—both applications that the Navy has a stake and interest in.

There is a desire to produce nanocrystalline powders from conventional gas-atomized feedstock in order to produce nanocrystalline coatings through cold spray deposition. There are a number of different methods that can provide the necessary powder microstructure, but as with all industrial processes, there is a very real requirement to maximize the economic and performance impacts, as well as a general need for consistency of output product. A potential answer to this problem can be found

in the process known as cryomilling, which is generally accepted in the literature at large as being the best way of accomplishing the task of creating nanocrystalline powders in a research environment. Cryomilling is a process which is remarkably similar to ball or impact milling—except that the milling apparatus is submerged in a bath of liquid nitrogen for the duration of the milling process. By maintaining the temperature of the mill—and the feedstock powder accordingly—near cryogenic temperatures (77 K), the heat generated by the milling process is removed. In conventional ball milling, the amount of heat generated is not trivial and is substantial enough to cause recovery and recrystallization within the powder microstructure, limiting the amount of cold work it is possible to add—thus placing a lower limit on the size of the grains possible to achieve with this process. By removing the heat generation created by the action of milling, the ability of the powder to engage in recrystallization and recovery is reduced to an absolute minimum, ensuring that the milling process produces the minimum grain size possible.

Powder evolution during cryomilling is similar to that documented for ball milling. A five step process has been outlined which includes particle flattening due to plastic deformation, particle welding, equiaxed particle formation, random welding of powder particles, and steady state deformation, during which a balance between fracture and cold welding is established as microstructural refinement progresses [39].

Bahmanpour et al. effectively demonstrated in 2011 that cryomilling would produce nanostructured powders with nano-scale crystallite sizes and homogenous microstructures in standard copper and copper/zinc alloys [40]. Hardened steel vials were loaded with powder under an argon atmosphere and milled for twelve hours to determine if there was a limit to crystallite size with respect to milling time, where it was recognized that nearly constant microhardness was obtained after approximately four hours of milling time, indicating that a near minimum crystallite size had been obtained. For pure Cu, Cu-10wt.%Zn, Cu-20wt.%Zn and Cu-30wt.%Zn these microhardness values were 2.4 GPa, 3.1 GPa, 2.9 GPa and 2.6 GPa, respectively—the reason why hardness decreased significantly from 10–30 wt.% Zn was unknown. Additionally, crystallite size as measured via X-ray diffraction (XRD) was determined to saturate after approximately four hours of milling time. For pure copper, Cu-10wt.%Zn, Cu-20wt.%Zn

and Cu-30wt.%Zn these crystallite sizes were approximately 15 [nm], 19 [nm], 18 [nm] and 9 [nm], respectively. A JEOL transmission electron microscope (TEM) at 200 kV was used to verify the homogeneity of the microstructure in the milled powder.

C. HYPOTHESES

1. Cold Spray of Microcrystalline Cu-Zn Alloys

Copper (Cu) is one of the most commonly utilized cold spray materials and via utilization of gas-atomized Cu as the feedstock material, working coatings can be produced—this has been extensively proven under a number of processing and powder parameters. Given that brass (Cu-Zn) exhibits a number of similar material properties, gas-atomized Cu-Zn powder feedstock should produce similarly effective working coatings through utilization of the cold spray process.

However, the stacking fault energy (SFE) of the 70/30 wt.% Cu-Zn alloy is extremely low at approximately 6 mJm^{-2}, an order of magnitude lower than the SFE of Cu at approximately 74 mJm^{-2}. Because of this, the strain hardening coefficient of Cu-Zn alloys will increase with increasing zinc content. Because of the increase in strain hardening during the spray and splat formation process, the feedstock particles will harden dramatically and this splat hardening will decrease the deposition efficiency. This relationship will hold true regardless of the fact that the melting point of Cu-Zn alloys decreases with increasing zinc content because the decrease in SFE is far more dramatic than the decrease in melting point, the deposit characteristics. As such, we predict that reduction in melting point will be inconsequential, and the increase in strain hardening rate will constrain the deposition efficiency of brass alloys as the zinc content increases.

2. Cold Spray of Nanocrystalline Cu-Zn Alloys

It has already been proven that deposits can be created with the cold spray deposition process via the use of nanocrystalline copper as the feedstock powder, albeit with significantly increased hardness and porosity in comparison to the use of microcrystalline feedstock powder. Thus, given the similarities between Cu and Cu-Zn

alloys, it should stand that nanocrystalline Cu-Zn alloys can similarly be successfully produced by the cold spray deposition method.

It has been shown that cryomilling of Cu-Zn alloys produces harder powders and smaller crystallite sizes than the cryomilling of pure copper by Bahmanpour et al., a function of the wt.% of added Zn—a logical outcome given an understanding of SFE's impact on cold work and temperature's effect on recovery and recrystallization. As such, the spray deposition efficiency of nanocrystalline Cu-Zn alloys will decrease with increasing zinc content due to the increased strain hardening coefficient. Furthermore, the deposits created by spraying nanocrystalline Cu-Zn alloys will be significantly harder, more porous and possess significantly more microstructural cracking—leaving a deposit with low bond strength.

II. EQUIPMENT INSTALLATION AND CALIBRATION

The research in this engineer's thesis was the first at the Naval Postgraduate School (NPS) to use cold spray deposition. A large portion of the work in this thesis was comprised of the installation, calibration, and testing of NPS' first cold spray deposition instrument. This chapter will describe the key aspects of this instruments installation and testing as necessary to understand the cold spray deposition data described in chapters III and IV.

A. INSTALLATION OF CENTERLINE (WINDSOR) SST MODEL SERIES C

All of the cold spray deposition completed during the process of this thesis was accomplished using Centerline—Supersonic Spray Technology's Series C apparatus, seen in Figure 7. The Series C model includes a glove box which houses both a manually operated and a robot controlled cold spray gun—allowing the operator the choice of creating deposits by hand or via pre-programmed instruction, respectively. Additionally, the system includes a wet particle filtration and scrubber system, used to filter the un-deposited powder particulate from the exhaust gas, preventing the escape of large amounts of possibly hazardous or explosive powder into the atmosphere. Still further, the apparatus also includes an electrical panel complete with a transformer, and a control box which contains two separate vibrational hoppers for delivering feedstock powder, allowing for the operator to casually switch between two different types of spraying feedstock. Finally, the Series C includes an additional and wholly separate THERMACH powder feeder that relies on computer timed rotational impact to deliver feedstock—providing the operator with a far more controlled and uniform powder feed rate if necessary.

Figure 7. Centerline SST Series C Cold Spray Apparatus at the Naval Postgraduate School.

B. CALIBRATION OF CENTERLINE (WINDSOR) SST MODEL SERIES C

In order to perform quantitative cold spray deposition experiments, several of the key pieces of equipment were carefully calibrated. The argon gas flow was calibrated using a simple flow meter in order to ensure precise and consistent gas flow would be delivered to the THERMACH powder feeder in accordance with specifications. Additionally the THERMACH powder feeder was calibrated so that precise, measured amounts of powder were delivered to the gas stream. Additionally, the main pressure delivery system was modified and calibrated to minimize flow losses in the system during operation while maintaining the ability to provide the maximum operating pressure allowed by the rated safety specifications.

1. THERMACH Powder Feeder

The first task undertaken during the calibration phase was the calibration of the THERMACH powder feeder and the associated gas flow required for its use. This calibration is important so that precise, measured amounts of powder were delivered to the gas stream.

Argon gas is used to support the powder feed so as to limit oxidation of the powder while within the feeder. A pressure regulator and gas flow meter were required to allow consistent feed of argon at 40 psi and 25 SCFM [air]. Because the densities of argon and air are different, and because gas flow meters are usually calibrated for a specific gas, gas flow meter, Figure 8, manufactured by King Instrument Company was installed and calibrated to compensate for differences between argon and air flow. This gas flow meter was rigidly mounted to the wall to allow for the user of the cold spray apparatus to easily reference the gas flow by visual inspection, even when operating on the other side of the equipment.

Figure 8. Powder Feeder Air Flow Meter by King Instrument Company.

The feed rate of the powder can be effectively monitored in two separate, yet mathematically relatable ways. First, the user can monitor the speed of the vibrational

impactor in the THERMACH feeder in RPM, depicted in Figure 9, or the user can similarly monitor the electronic feed rate from the control panel in percentage of maximum feed rate [%], as seen in Figure 10. Each setting on the control panel in [%] is directly correlated to some preset rotational speed [RPM] of the impactor. The table of control panel electronic feed rates [%] and their associated THERMACH [RPM] speeds were provided by Centerline technical support upon the author's request. It is critically important to note; however, that neither of these observable measurements of feed rate allows the user to know the actual mass feed rate—critical information necessary to allow for the calculation of the deposition efficiency.

Figure 9. THERMACH Powder Feeder Vibrational Impactor Speed [RPM] Example.

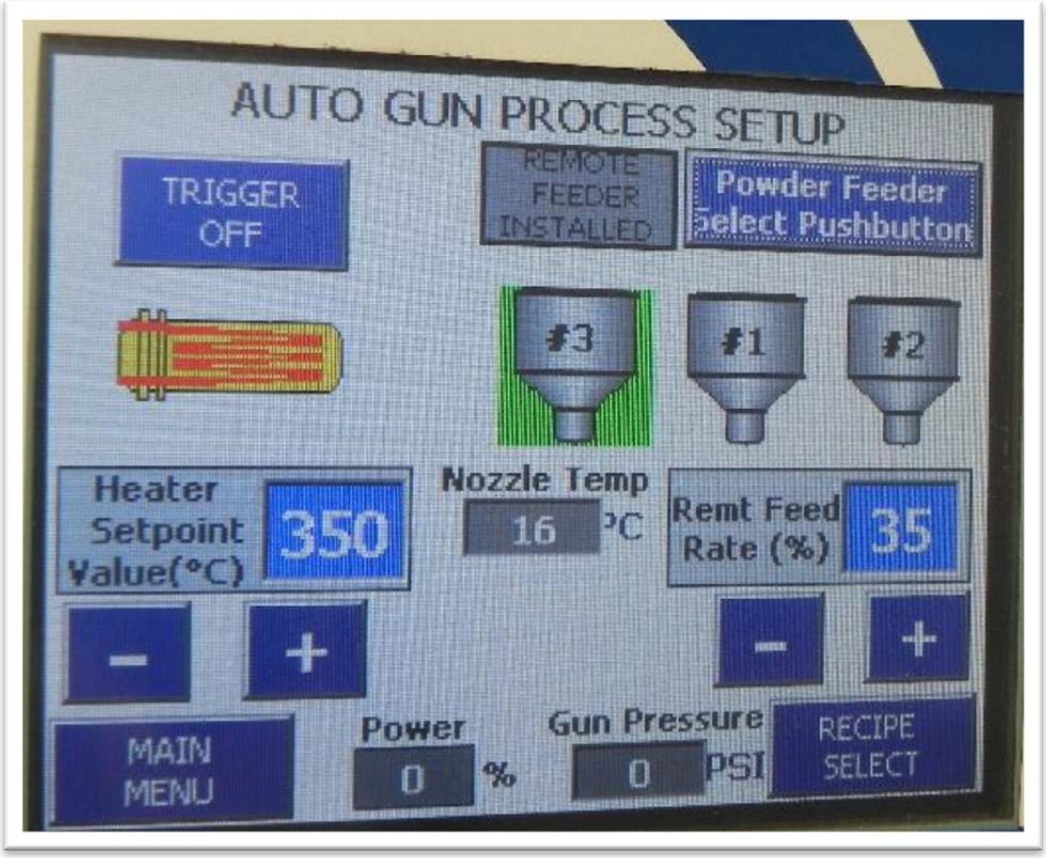

Figure 10. Centerline SST Model Series Control Panel Interface.

In order to accurately determine feed rates in mass terms, the THERMACH feeder was operated for a specific period of time—monitored by stopwatch—whereby the powder feedstock was diverted via plastic tubing into a detached HEPA filter instead of the entraining gas flow. The mass of the HEPA filter was measured before and after these runs, and the difference was noted as the total mass of feed for that run. Each run was conducted twice to obtain slightly more accurate results via mass averaging and to compensate for minute amounts of powder that escaped the improvised seat on the HEPA filter. This process was conducted for a number of predetermined set speeds (in RPM)—those known to coordinate with feed rate in % terms, the only parameter by which feed rate may be controlled by the user during operation.

Mass feed rate calibration curves were constructed by obtaining powder mass feed rates for specific feeder RPM's. These calibration curves showed that the powder

mass feed rate was quite linear with both rotational speed on the THERMACH feeder and with the electronic feed rate on the cold spray system control (Figures 11–15). Because the mass of the individual powders changes based on which particular element or alloy is used, this process was repeated for each of the five powders discussed in this thesis.

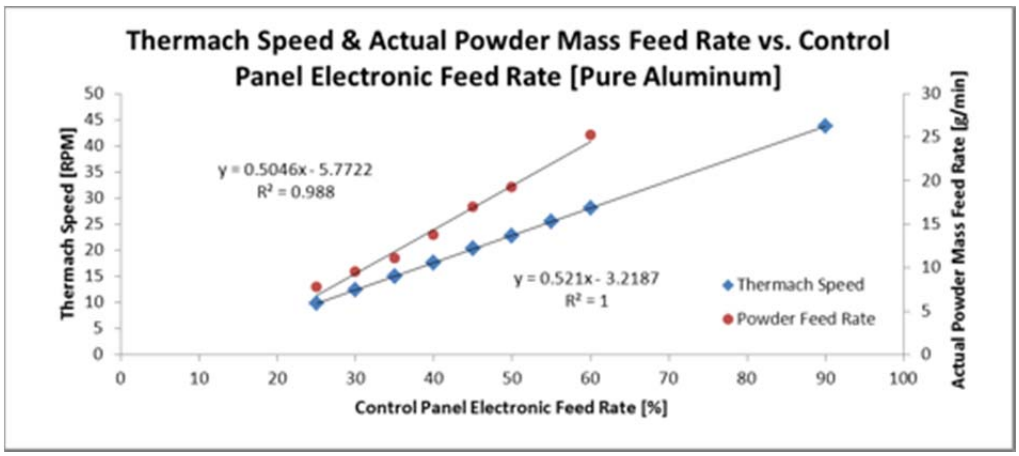

Figure 11. Calibration Curves for Thermach Powder Feeder and SST Series C Control Panel [Pure Aluminum].

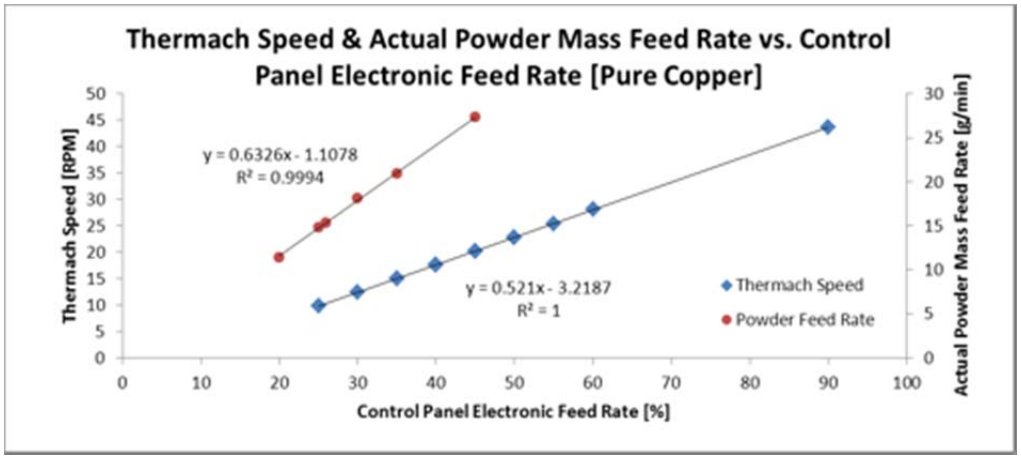

Figure 12. Calibration Curves for Thermach Powder Feeder and SST Series C Control Panel [Pure Copper].

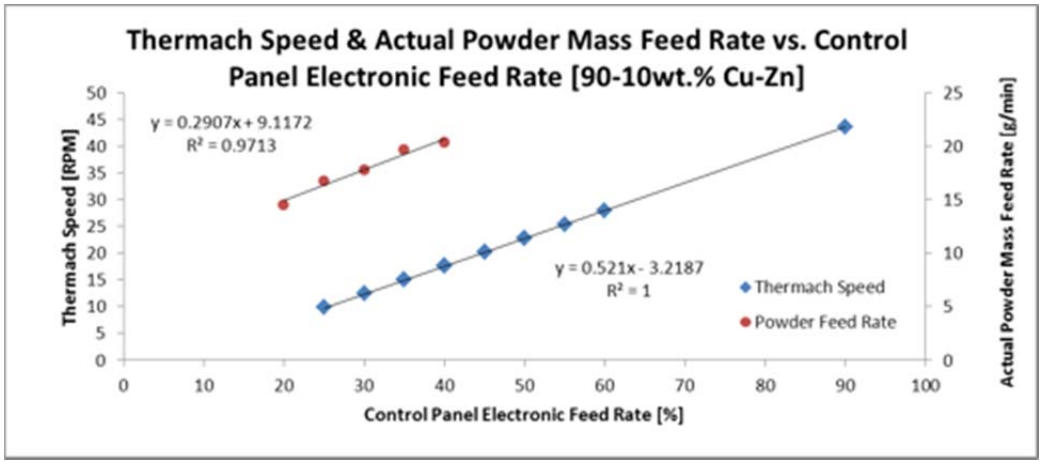

Figure 13. Calibration Curves for Thermach Powder Feeder and SST Series C Control Panel [90–10wt.% Cu-Zn].

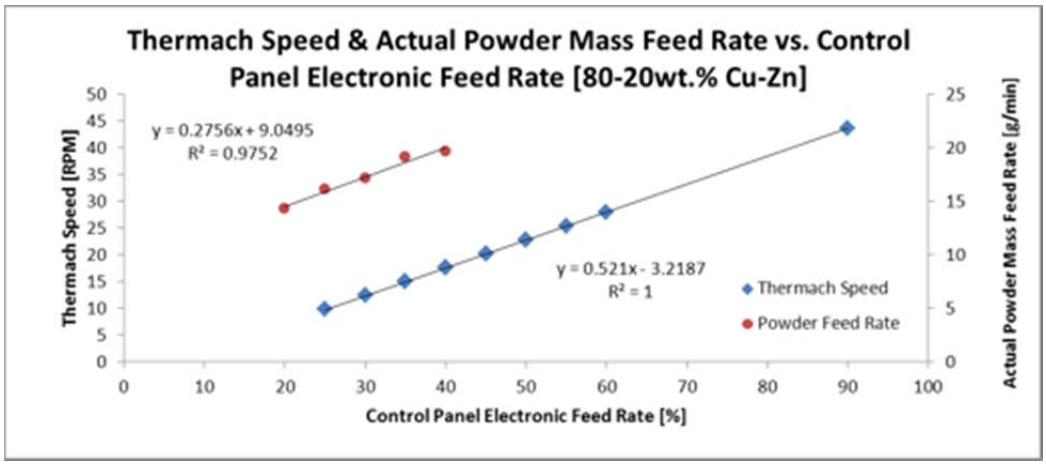

Figure 14. Calibration Curves for Thermach Powder Feeder and SST Series C Control Panel [80–20wt.% Cu-Zn].

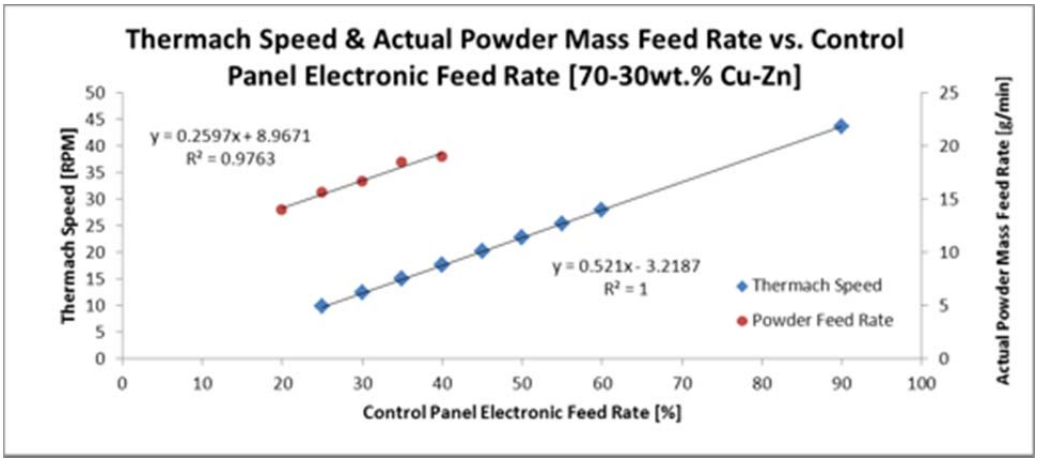

Figure 15. Calibration Curves for Thermach Powder Feeder and SST Series C Control Panel [70–30wt.% Cu-Zn].

2. Entraining Gas Flow

The exact pressures of the entraining gas flow are at the heart of the cold spray deposition experiment, and as such were carefully calibrated to allow for quantitative control of the deposition experiments. There exists within the control panel itself a pressure regulator that steps down the initial entraining gas pressure to its final value—disregarding minor losses experienced in the final stretch of piping that lies between the regulator and the nozzle. The system however is not burst-proof, and is limited by solenoid valve control to pressures of 300 psi [2.07 MPa] and lower by the manufacturer to provide an adequate safety margin for the installed piping and joints. Because of the electronic limit on the allowable pressure within the Series C apparatus, an additional pressure regulator must be used prior to the control panel and after the source bottle, as the source bottle often supplies at pressures between 400–2,500 psi, exposure to which would cause irreparable damage to the equipment. It is important to note; however, that during operation the flow will be supersonic, and as such there exists the very real possibility of friction choking the flow, thus limiting the maximum pressure achievable and exacerbating the losses experienced in the gas lines—ultimately limiting operational parameters. To alleviate this concern, pressure regulators and piping were chosen and installed so as to maximize the flow coefficient (C_V), while maintaining the required pressure performance characteristics to ensure losses were minimized and accordingly,

operational parameters could be maintained. In the end, the total losses throughout the system, from source bottle to nozzle, were measured to be approximately 50 psi [0.34 MPa] during operation at maximum operating nozzle pressure (300 psi [2.07 MPa]). For clarification, a flow chart can be found in Figure 16, which delineates the gas pressures found at different points during operation.

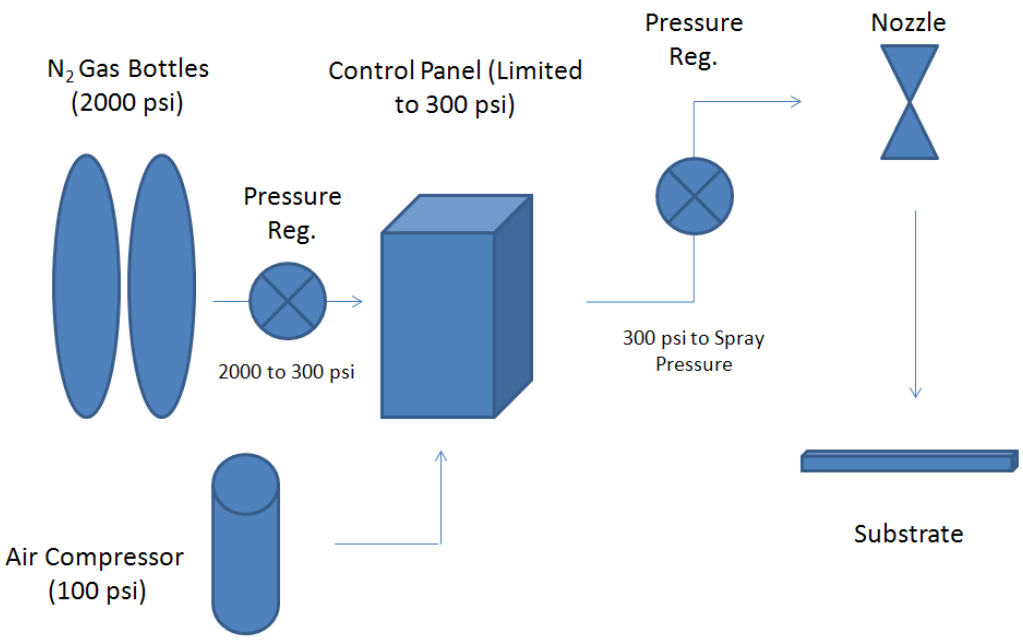

Figure 16. Flow Chart of Equipment Gas Flows During Operation.

C. COLD SPRAY DEPOSITION TESTING WITH THE MODEL SERIES C APPARATUS

Once the system was installed and calibrated, we performed a comprehensive series of deposition tests to confirm that the system was operating properly and to better understand how key system parameters (e.g. temperature, pressure, nozzle stand-off distance, etc.) affect cold spray deposition. The resultant deposition performance was compared against similar data from Centerline SST and the open literature. Based on this testing, it was confirmed that the installation was successful and that this instrument could be confidently used for the brass deposition experiments described in chapters III and IV.

1. Powder Characterization, Experimental Setup, and Methodology

A comprehensive series of deposition tests were undertaken with the Centerline SST Model Series C in order to confirm that the system was operating properly after installation and calibration. Additionally, it was pertinent to the setup of the brass experiments to quantify precisely how key system parameters (e.g. temperature, pressure, nozzle stand-off distance, etc.) would affect the final deposition characteristics. By maximizing deposition efficiency, the thickest deposits could be obtained—allowing for analysis techniques such as hardness indentation and coating thickness measurement to be easier to implement.

The principal cold spray process controls of temperature, pressure, nozzle stand-off distance and substrate roughness were investigated as they have been carefully examined in the literature for both copper and aluminum powders. For instance, J. Pattison et al. discussed in great detail the physics of the bow shock exiting the nozzle and the associated effects of such a shock by examining the consequences of shifting the nozzle stand-off distance [41]. It is important to note that the work of Pattison et al. utilized different nozzle designs, different entraining gases and different powders than used during the current calibration experiments. We did not modify the nozzle design for the Centerline instrument, instead using the commercial nozzles supplied with the instrument. In addition, we performed all of the experiments with commercial purity, nitrogen gas. We did not explore the effects of using helium as the entrainment gas due to its high cost.

The test depositions were made using a standard commercial 50 wt.% alumina/50 wt.% aluminum proprietary powder (SST-A0050), provided by Centerline SST. This powder, shown in Figure 17, possessed a non-spherical morphology and was verified to have a mean particle size of 21.5 µm, measured using a Horiba Laser Scattering Particle Size Analyzer (LA-950V2). The bright particles seen in the figure are aluminum oxide. This powder was chosen because it was the powder utilized in Centerline SST's calibration data, and the powder for which they had the most pertinent and extensive information.

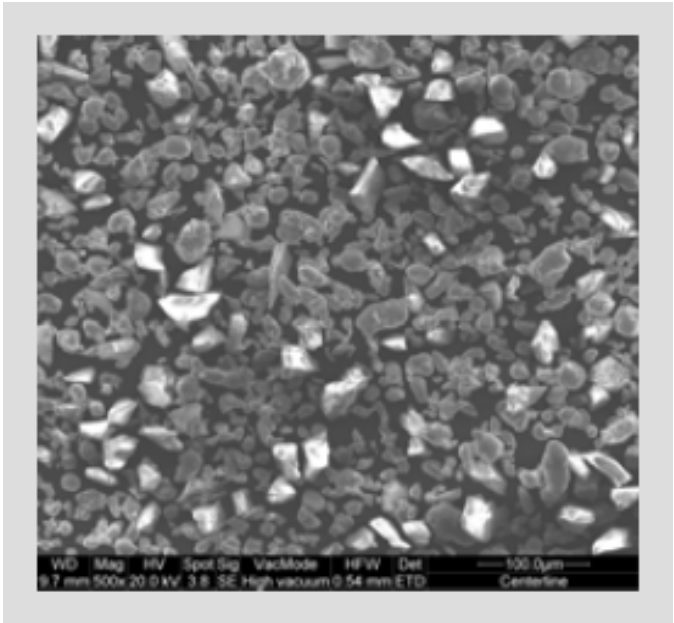

Figure 17. SEM Photograph of SST-A0050 [50 wt.% Aluminum/50 wt.% Alumina] Powder. From Centerline SST.

Tungsten carbide nozzles were used with a length of 120 mm and a nozzle orifice of 2 mm. All spray deposits were made on ¼" thick, 6061 aluminum substrates supplied by McMaster Carr. The spray pattern characteristics are described visually in Figure 18. Ten total passes were completed in each of the runs to form a single complete spray pattern of approximately 24 mm in width. Spray temperature and pressure were recorded via the manufacturer-installed electronic pressure and temperature gauges and the spray deposit thickness at the thickest cross section was measured with a digital micrometer. The equations necessary for calculating deposition efficiency are:

(1) $$DE = \frac{Mass_{Deposit}}{Mass_{SprayedPowder}}$$

(2) $$Mass_{Deposit} = Mass_{Substrate+Deposit} - Mass_{Substrate}$$

(3) $$Mass_{SprayedPowder} = FeedRate_{Powder} * TotalSprayTime$$

To obtain the total mass of the deposited material the mass of the substrate prior to spray was subtracted from the mass of the substrate after deposition—masses were measured with a precise digital scale. The total spray time was measured with a digital stopwatch. Powder feed rate was previously determined. After calculating deposition efficiency, the data was then compiled into a series of spreadsheets with Microsoft Excel, the details of which are contained in Tables 2, 3, 4 and 5. Each of the data tables has been segregated into its pertinent and independent discussion section for clarity of presentation.

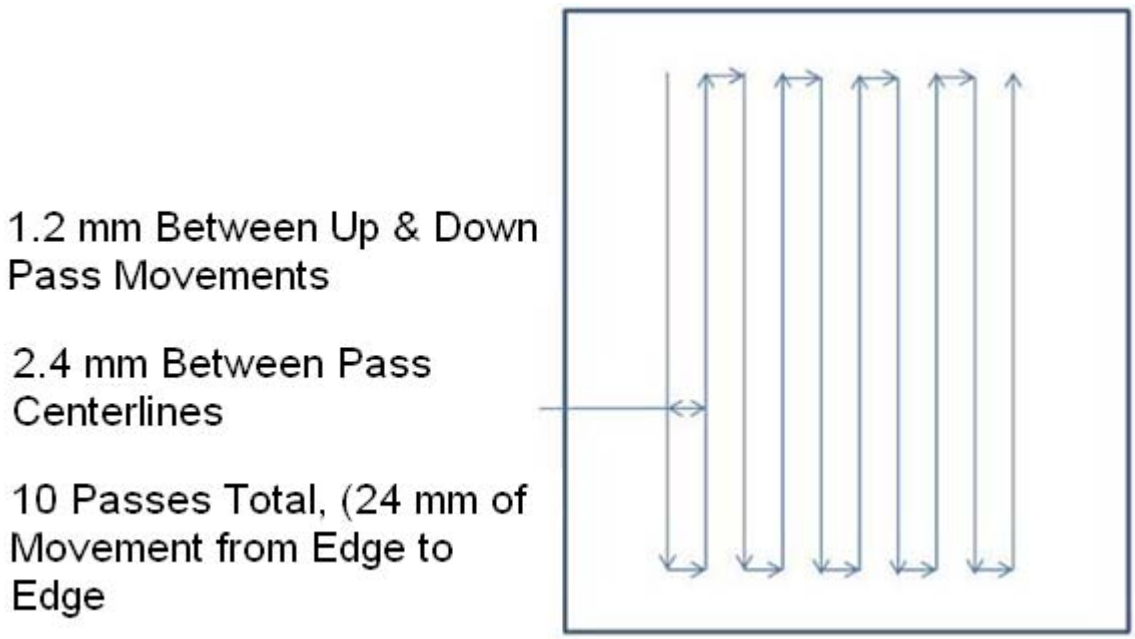

Figure 18. Cold Spray Deposition Pattern.

2. Reproduction of the Benchmark Data Provided by Centerline SST

The initial set of deposition tests were undertaken to attempt to reproduce the benchmark data for the Model Series C provided by Centerline SST, listed for reference in Table 1—as a way of ensuring our modification and calibration processes were indeed successful and our system operating as specified. Nine independent and separate test conditions were chosen—two of which were matched with the benchmark parameters, tests 3 & 4—in order to provide sufficient comparison with other parameters and to

provide sufficient data for obtaining pressure and temperature relationships with deposition efficiency. The spray parameters and associated deposition outputs obtained in the first round of testing can be found in Table 2—the parameters which were modified and the deposition outputs have been highlighted in the table in order to focus the reader on the important metrics.

Powder Material	SST-A0050
Gas (Air, N_2 or He)	N_2
Substrate Material	1018 Steel
Gun Type	Automatic
Gas Temperature (°C)	350
Gas Pressure (psi)	250
Powder Feed Rate (g/min)	15
Gun Stand-off Distance (mm)	12
Gun Traverse Speed (mm/s)	40
Gun Step Over per Pass (mm)	1.2
Deposition Efficiency (%)	39.5
Deposition Rate (g/min)	5.9
Hardness (HB)	46
Coating Thickness per Pass (µm)	889
Bond Strength (psi)	4426

Table 1. Reference Spray Data from Centerline SST for Series C with SST-A0050 [50.wt% Aluminum/50 wt.% Alumina] Powder, April 2009. After Centerline SST.

Test No.	**1**	**2**	**3**	**4**	**5**	**6**	**7**	**8**	**9**
Powder Material	SST-A0050	SST-A0050	SST-A0050	SST-A0050	SST-A0050	SST-A0050	SST-A0050	SST-A0050	SST-A0050
Gas (Air, N_2 or He)	N_2	N_2	N_2	N_2	N_2	N_2	N_2	N_2	N_2
Substrate Material	1018 Steel	1018 Steel	1018 Steel	1018 Steel	1018 Steel	1018 Steel	1018 Steel	1018 Steel	1018 Steel
Gun Type	Automatic	Automatic	Automatic	Automatic	Automatic	Automatic	Automatic	Automatic	Automatic
Gas Temperature (°C)	350	350	350	350	350	350	400	350	400
Gas Pressure (psi)	150	200	250	250	285	200	200	250	250
Powder Feed Rate (g/min)	15	15	15	15	15	15	15	15	15
Gun Stand-off Distance (mm)	12	12	12	12	12	12	12	12	12
Gun Traverse Speed (mm/s)	40	40	40	40	40	40	40	40	40
Gun Step Over per Pass (mm)	1.2	1.2	1.2	1.2	1.2	1.2	1.2	1.2	1.2
Deposition Efficiency (%)	5.7	9.2	14.7	13.5	16.9	9.2	11.4	14.7	17.8
Coating Thickness per Pass (µm)	210	320	450	420	530	320	360	450	610

Table 2. Obtained Spray Data for Series C with SST-A0050 [50.wt% Alumina/50 wt.% Aluminum].

3. Pressure and Temperature Relationships for Alumina/Aluminum Powder Mix

The effect of modifying pressure can be observed by re-evaluating tests 1–5 in the previous data, again, found in Table 2. A graphical representation of the data is presented in Figure 19. Gas temperature was held constant at 350 °C, while spray was conducted at a variety of pressures in 50 psi [0.35 MPa] increments. 285 psi [1.97 MPa] was chosen as the high pressure because of a high pressure safety trip-off which occurs at 300 psi [2.07 MPa]—in order to prevent reaching this limit during spray a moderate margin of tolerance was chosen. Every other parameter was held constant. Clearly, increases in pressure increase both the deposition efficiency and the final coating thickness, which concurs with the general literature. This occurs largely due to an increase in entraining gas density prior to the nozzle throat, brought on by the increased pressure of the gas supply.

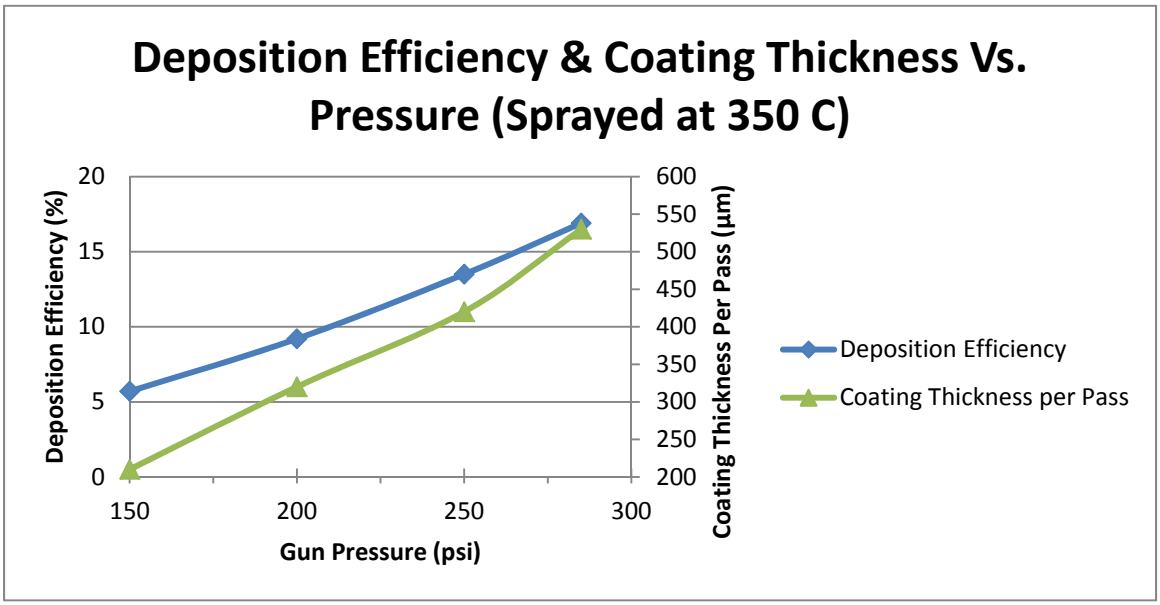

Figure 19. Deposition Efficiency and Coating Thickness Per Pass Vs. Spray Pressure for SST-A0050.

A similar procedure was adopted to evaluate the effect of altering entraining gas temperature, outlined in tests 6–9, the data of which is again contained in Table 2. In this set of test runs, temperature was modified and the other parameters including pressure

were held constant. This was completed for two separate pressure settings: 200 psi [1.38 MPa] and 250 psi [1.72 MPa].

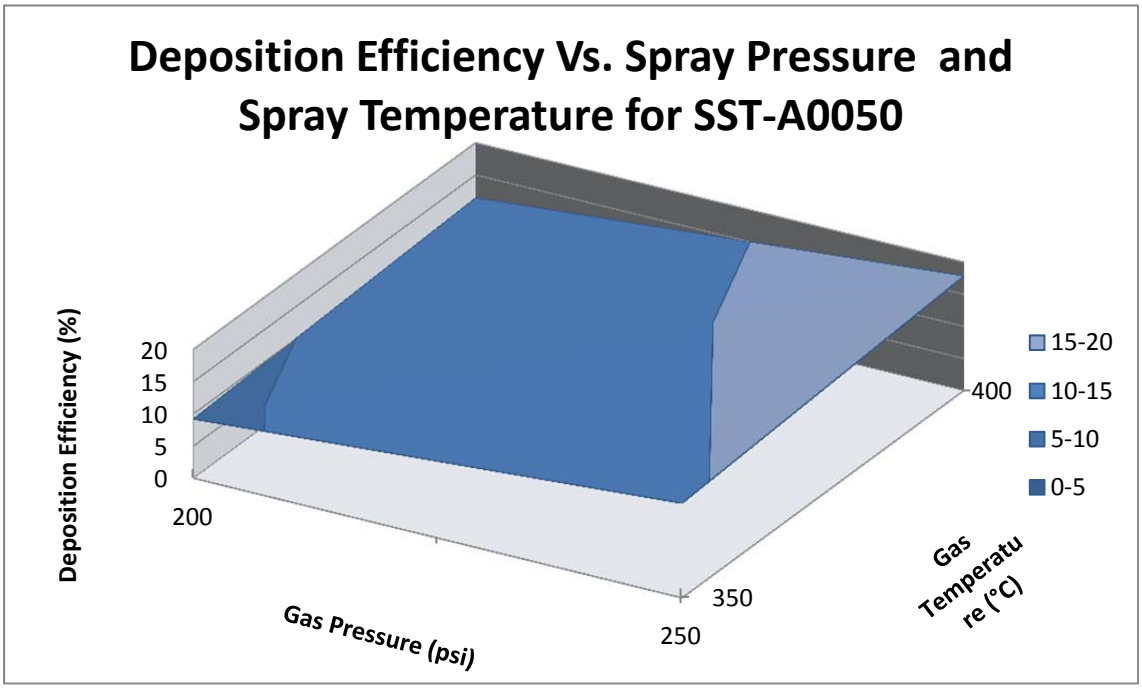

Figure 20. Deposition Efficiency Vs. Spray Temperature and Spray Pressure for SST-A0050.

As with pressure, increasing the temperature of the entraining gas also increased both the deposition efficiency and coating thickness (Figure 20). Again, our results were in agreement with the general disseminated literature, asserting further confidence in the proper working condition of the cold spray apparatus.

On a more interesting note, it would appear from the obtained data that pressure appears to be a bigger 'lever' than temperature. While increasing entraining gas temperature by 15% (50 °C) produced a 21% increase in deposition efficiency, increasing the entraining gas pressure by a similar 14% (35 psi) allows us to increase deposition efficiency by 26%. Thus, if limited operationally between having to choose between increasing either spray temperature or spray pressure, increasing the spray pressure will have the greater effect.

4. The Effect of Pre-existing Substrate Roughness on Deposition Characteristics

Beyond the effects of pressure and temperature, exploration of the effect of substrate surface roughness on the deposition efficiency and coating thickness was examined. Centerline SST engineers had notified Naval Postgraduate School that roughening the surface of the substrate via sandblasting or etching was critical to maximizing deposition efficiency, especially in those materials with relatively low bond strength—such as copper. Furthermore, they noted that deposit bond strength could be greatly increased by roughening the substrate surface prior to deposition, an effect which was not studied in depth. It is hypothesized however that improved deposit bonding occurs in samples that possess prior existing roughness of the substrate surface due to better interfacial mixing between the deposit and substrate material. To enhance the surface roughness of the substrate, 80 grit aluminum oxide particles purchased from Centerline SST (SST-G0002) were sprayed utilizing the manual configuration of the Model Series C cold spray apparatus at room temperature—with nitrogen gas at 150 psi [1.03 MPa] and a stand-off distance of approximately 20 mm. Table 3 displays the results during which the relationship between deposition efficiency and substrate surface roughness was considered. Test 10 involves the use of the sandblasted substrate and Test 11 involves the use of the standard smooth substrate.

Test No.	10	11
Powder Material	SST-A0050	SST_A0050
Gas (Air, N_2 or He)	N_2	N_2
Substrate Material	1018 Steel	1018 Steel
Substrate Surface (SB or Smooth)	SB	Smooth
Nozzle Type (WC or Polymer)	WC	WC
Gun Type	Automatic	Automatic
Gas Temperature (^oC)	350	350
Gas Pressure (psi)	250	250
Powder Feed Rate (g/min)	15	15
Gun Stand-off Distance (mm)	12	12
Gun Traverse Speed (mm/s)	40	40
Gun Step Over per Pass (mm)	1.2	1.2
Deposition Efficiency (%)	17.4	14.7
Coating Thickness per Pass (µm)	470	440

Table 3. Deposition Efficiency and Coating Thickness per Pass for a Sandblasted Substrate and a Smooth Substrate in Otherwise Common Spray Setups.

With no other changes to our spray set up, it was discerned that sandblasting the substrate surface prior to cold spray deposition produced a 15% increase in deposition efficiency, and approximately a 10% increase in the coating thickness per pass while spraying SST-A0050.

The exact values for deposition efficiency and thickness per pass are quite sensitive to the cold spray deposition system and the powders used. The rather extensive number of process parameters which may be modified can make direct comparison with data from the literature or taken on other cold spray systems quite difficult. As shown in Table 1, the reference data from Centerline SST taken in 2009 using SST-A0050 powder was substantially different from the current study. In fact, the deposition efficiencies reported by Centerline were approximately three times larger than those observed in the current study.

A number of sources for the discrepancies in deposition efficiency were identified. First, the powder size of Centerline's proprietary alumina/aluminum mix had changed substantially since the reference data was taken in 2009. The mean powder size was increased by some un-specified amount to the current mean of 21.5 microns. An

increase in particle size will lower particle spray velocities and thus deposition efficiencies. Additionally, Centerline SST intentionally used thin substrates during their benchmarking experiments so that the temperature of the substrate would be as high as possible during the run. Furthermore, the substrates were heated to relatively high temperatures immediately prior to spraying—again, higher substrate temperature making the material more malleable and thus increasing the deposition efficiency of the spray. These process choices were different from those used in the current testing, and as such, the deposition efficiencies here are reasonable, but lower than those reported by Centerline. It should be noted that engineers from Centerline personally visited NPS and verified that the NPS system was working correctly.

In contrast, the deposition efficiencies measured using the NPS system were as high, if not higher, than those observed in the work of Irrissou et al. from the National Research Council, Canada [42]. They reported in 2007 obtaining deposition efficiencies of 11.8% using a similar aluminum-alumina powder mixture—they also used a Centerline SST cold spray system, using a similar spray pattern. The operating parameters chosen by Irrisou et al. were somewhat different however, although reasonably similar. For their deposits, Irrisou et al. used a stand-off distance of 10 mm, a spray pressure of 90 psi [0.62 MPa], a spray temperature of 500 °C, nitrogen gas as the entraining medium and mild steel substrates that had been previously grit blasted. Additionally, their alumina particles had a different mean particle size than their aluminum particles, 25.5 µm and 36.2 µm, respectively, in contrast to a mean particle size of 21.5 µm in the SST-A0050 mixture which contained similarly sized alumina and aluminum particles. Taken in aggregate, Irrisou et al. used a 43% higher temperature, a 64% lower pressure and a 65% larger mean particle size for their aluminum powder. Thus, it would be reasonable all else being more or less the same to expect an appreciably smaller deposition efficiency given the relationships between spray pressure, temperature and particle size. That is precisely what was observed by Irrisou et al.—their deposition efficiencies were approximately 47% lower than what we observed. Ultimately, comparison with the work of Irrisou et al. provides further confirmation for the operating

parameters/deposit output relationships previously determined in this thesis, as well as confidence that the cold spray apparatus was indeed working properly.

5. The Effect of Spray Nozzle Characteristics on Deposition

The nozzle stand off distance was examined to determine whether the standard, 20mm, distance would provide optimal deposition efficiency. The nozzle stand-off distance was altered by simply changing the vertical position of the cold spray gun/nozzle apparatus in 10 mm increments—from 5 mm to 45 mm. Pressure and temperature were held constant at 250 psi [1.72 MPa] and 350 °C, respectively (Table 4). Figure 21 provides a visual depiction of how the nozzle stand-off distance was altered and how calipers were used to verify and measure the stand-off distance.

Figure 21. Photograph of the Process of Modifying the Nozzle Stand-Off Distance.

From the data set in Table 4, visually depicted in Figure 22, it can easily be seen that increasing stand-off distance will decrease deposition efficiency and coating thickness per pass. Furthermore, this relationship seems to be more or less linear, at least

in the range of observation. However, this graph does not depict the entire relationship—to more accurately describe the relationship between nozzle stand-off distance and deposition efficiency, we must turn to the literature.

Test No.	12	13	14	15	16
Powder Material	SST-A0050	SST-A0050	SST-A0050	SST-A0050	SST-A0050
Gas (Air, N_2 or He)	N_2	N_2	N_2	N_2	N_2
Substrate Material	1018 Steel	1018 Steel	1018 Steel	1018 Steel	1018 Steel
Gun Type	Automatic	Automatic	Automatic	Automatic	Automatic
Gas Temperature (°C)	350	350	350	350	350
Gas Pressure (psi)	250	250	250	250	250
Powder Feed Rate (g/min)	15	15	15	15	15
Gun Stand-off Distance (mm)	5	15	25	35	45
Gun Traverse Speed (mm/s)	40	40	40	40	40
Gun Step Over per Pass (mm)	1.2	1.2	1.2	1.2	1.2
Deposition Efficiency (%)	17.4	14.9	14	11.6	9
Coating Thickness per Pass (µm)	470	420	400	360	290

Table 4. Deposition Efficiency and Coating Thickness vs. Nozzle Stand-Off Distance for SST-A0050 [50.wt% Alumina/50 wt.% Aluminum].

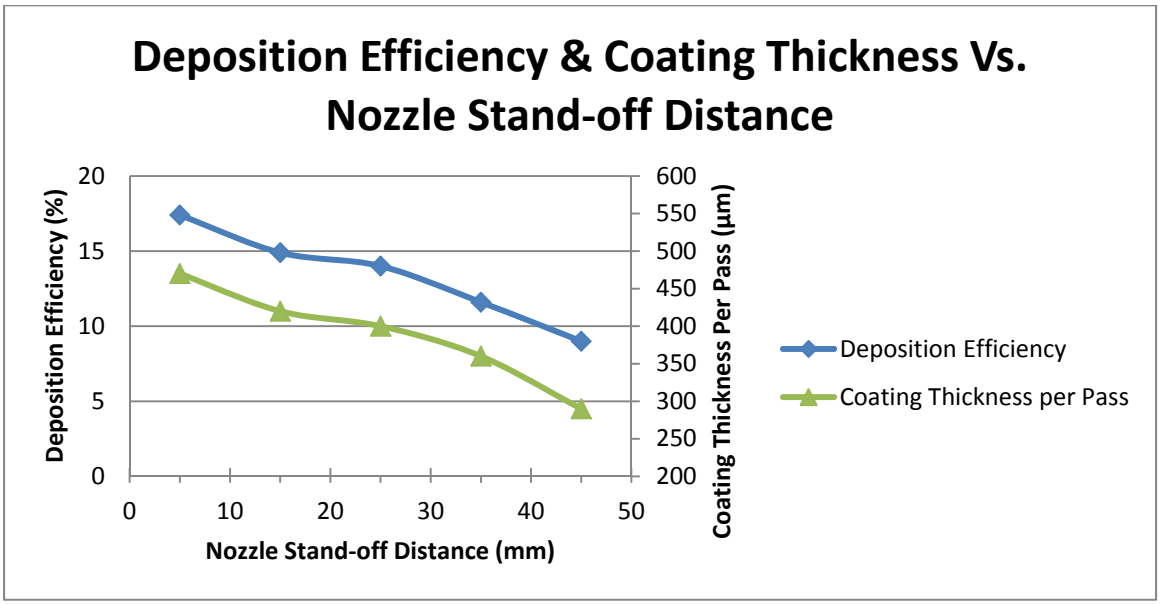

Figure 22. Deposition Efficiency and Coating Thickness per Pass Vs. Nozzle Stand-off Distance for SST-A0050.

In particular, J Pattison et al. describes, in detail, the effect of stand-off distance on particle velocity, and thus deposition efficiency [41]. Figure 23 provides an excellent visual summary of their work, and sets the background for the relationship we are trying to elicit. At very close distances between the nozzle and the substrate (Region 1), they demonstrate that increasing stand-off distance at first actually increases the velocity of the particles. This regime is dominated by the effects of the bow shock at the exit of the nozzle. The bow shock and stagnation bubble created by the incident flow out of the nozzle adversely impact the flow properties of the particles in transit, and expose the incident particles to massive changes in drag force—as the particles slow due to these forces, many will have their velocity fall below critical velocity, with an according reduction in deposition efficiency. Thus, as stand-off distance increases, the effects of the bow shock are attenuated and particle velocity increases along with deposition efficiency. In Region 2, particle velocity continues to increase, and reaches an optimum—where gradual particle acceleration due to increasing entraining gas velocity finds a balance with the drag experienced by the particles. And finally, in Region 3, as gas velocity begins to decrease and the cumulative drag force on the particles begins to dominate the fluids model, particle velocity begins to decrease—and with it deposition efficiency.

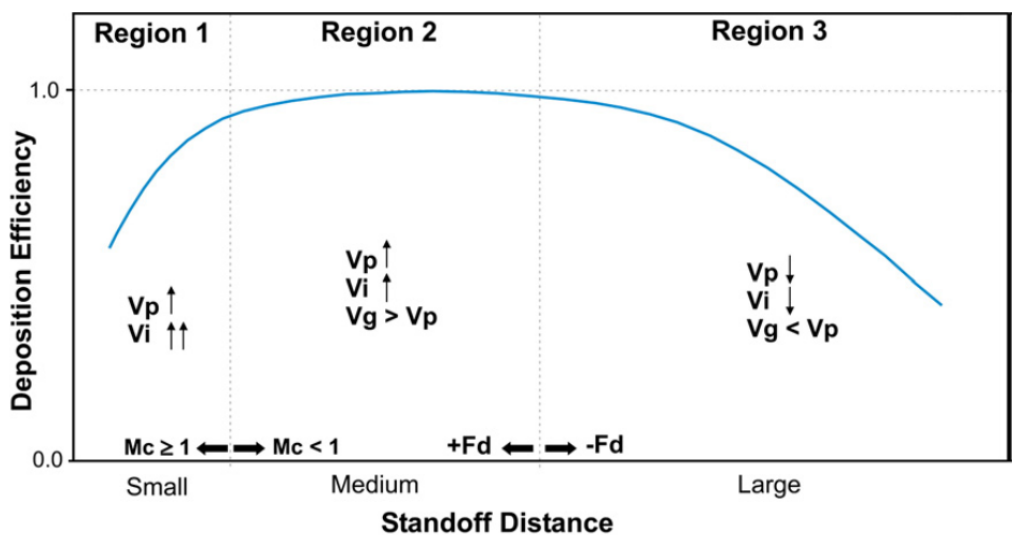

Figure 23. Non-Dimensional Chart Showing the Effect of Stand-Off Distance on Deposition Efficiency. From Pattison et al. [41].

It is critical to note that these stand-off distances reference the exit of the diverging section of the de-Laval type nozzle. However the nozzles produced by Centerline SST and used in our relationship testing are 120 mm in length—although the precise nozzle geometries are unknown, it would be reasonable to expect that a significant portion of the length of the UltiLife and UltiFlow nozzles are simply in place to minimize spread of the spray pattern, and are not part of the diverging section of the nozzle. Because of this, the use of Centerline SST's nozzles places us in the tail-end area of Region 3 in the above curve—which explains the relationship dynamics seen in testing, notably the more or less linear decrease in deposition efficiency with increasing stand-off distance. A future point of research may be to alter the length of the nozzle by mechanical means in order to find the optimal region in the curve above.

Lastly, the choice of material type for the cold spray nozzle was explored. Centerline SST provides two different types of nozzles. First they offer the UltiLife nozzle, which is made from tungsten carbide, and is meant to enhance its durability. This type of nozzle is particularly important if hard or abrasive materials are being sprayed. They additionally offer the UltiFlow series of nozzle, which is manufactured using "a clog-resistant material that makes it ideal for applications that require spraying pure materials" [43]. Pure, soft metals, such as aluminum and zinc, are known to have problems with nozzle clogging during cold spray in the Centerline system. However, because the UltiFlow series of nozzle is made from polymer, the maximum rated temperature that can be used during spray operation with the nozzle is 350 °C, which may limit the operator depending on the application. Both nozzles were exactly the same with respect to geometrical design—each had a length of 120 mm and an orifice size of 2 mm. Test deposits were sprayed at a pressure of 250 psi [1.72 MPa] and a temperature of 350 °C, at a constant stand-off distance of 12 mm (Table 5).

Test No.	17	18
Powder Material	SST-A0050	SST_A0050
Gas (Air, N_2 or He)	N_2	N_2
Substrate Material	1018 Steel	1018 Steel
Nozzle Type (WC or Polymer)	WC	Polymer
Gun Type	Automatic	Automatic
Gas Temperature (^oC)	350	350
Gas Pressure (psi)	250	250
Powder Feed Rate (g/min)	15	15
Gun Stand-off Distance (mm)	12	12
Gun Traverse Speed (mm/s)	40	40
Gun Step Over per Pass (mm)	1.2	1.2
Deposition Efficiency (%)	17.4	14
Coating Thickness per Pass (µm)	470	400

Table 5. Modification of Nozzle Type for Series C with SST-A0050 [50.wt% Alumina/50 wt.% Aluminum].

The tungsten carbide nozzle (UltiLife) showed a small, but measurable, increase in deposition efficiency compared with the spray characteristics of the polymer (UltiFlow) nozzle. When using the UltiFlow polymer nozzle, deposition efficiency degraded by about 25%, in the case of the sandblasted substrates as well as the unmodified substrates. This degradation in deposition efficiency was both unexpected and is not fully understood. It is hypothesized that the UltiFlow polymer nozzle could have a large coefficient of thermal expansion in comparison to the UltiLife tungsten carbide nozzle—when the hot gas flow passes through the UltiFlow nozzle, this could cause the dimensions of the internal nozzle design including the throat diameter to change, thus altering the fluid mechanics of the nozzle and limiting the exit velocity from the nozzle.

THIS PAGE INTENTIONALLY LEFT BLANK

III. COLD SPRAY OF MICROCRYSTALLINE COPPER AND BRASS

While the thermodynamics and fluid mechanics of the cold gas-dynamic spray process are relatively well understood, the effects of feedstock powder microstructure and composition on the deposition process remain largely unknown except in limited special cases. This chapter will attempt begin to explore the effects of alloying on powder spray characteristics using the Cu-Zn alloy system in an attempt to comprehend the effects of cold spray deposition as it pertains to common face-centered cubic metals and their alloys. The evaluation and characterization of the feedstock powders is discussed in depth in Section A, while the experimental setup can is delineated in Section B. During the experiment, deposition efficiency, coating thickness per pass, hardness, porosity and compositional variance were all characterized as functions of spraying pressure, spraying temperature and feedstock particle composition in each of the materials. The experiment results and discussions are contained in Sections C and D, respectively.

A. FEEDSTOCK POWDER CHARACTERIZATION

To properly characterize the entire Cu-Zn single phase alloy model in our experiments (found at concentrations of less than approximately 40 wt.% Zn), four powders were purchased from ACu Powder in Union, New Jersey—620 Series pure copper powder (>99.5% purity), the 900 Series 90/10 wt.% Cu-Zn powder, the 800 Series 80/20 wt.% Cu-Zn powder and the 700 Series 70/30 wt.% Cu-Zn powder. Hereafter, these powders will be referred to by their nominal compositions to avoid any confusion. Table 6 contains the pertinent particle size and composition data as kindly provided by ACu Powder upon request—this information includes a sieve analysis for each of the powders and a batch compositional analysis [44]. The sieve analysis for the pure copper powder simply contained the particle size under which 10%, 50% or 90% of the particles were classified and not a full mesh analysis like the brass powders—for instance, Table 6 delineates that 90% of the pure copper powder particles were less than 45.01 microns in size. Each of the brass powders was verified via batch spectroscopy to be within +/- 2 wt.% of the nominal composition. The brass powders are manufactured using a diffusion-

alloying process, where fine copper powder is coated with zinc and then run through a furnace to allow diffusion of the zinc throughout the particle.

Powder Material	Greater Than (µm)	Less Than (µm)	% of Total	Composition Zn (wt.%)
Cu-90/10 wt.% Zn	149	177	0.2	9.94
	99	149	3.6	
	74	99	3	
	44	74	4.1	
		44	89.1	
Cu-80/20 wt.% Zn	149	177	0.5	18.84
	99	149	5.7	
	74	99	5.5	
	44	74	8.7	
		44	79.6	
Cu-70/30 wt.% Zn	99	149	1.6	31.8
	74	99	2.5	
	44	74	4.1	
		44	91.8	
Pure Copper	45.01		10	>99.5% Pure
	26.31	45.01	40	
	15.85	26.31	40	
		15.85	10	

Table 6. Sieve and Batch Composition Analysis for Pure Copper, Cu-90/10 wt.%, Cu-80/20 wt.% and Cu-70/30 wt.% Zn Powders. From ACu Powder [44].

These powders were chosen so as to minimize the spread of particle size and shape, mitigating the risk that experimental results could be modified by different particle sizes and morphologies. Each of the powders possessed a spheroid particle shape, with aspect ratios less than 1.2, as visually determined by scanning electron microscope (SEM) evaluation; however, it should be noted that the pure copper powder was more consistently spherical in shape in comparison to the more spheroid shaped brass powders. Scanning electron microscope photos of each of the powders can be found below in Figure 24, each taken at 1000x magnification.

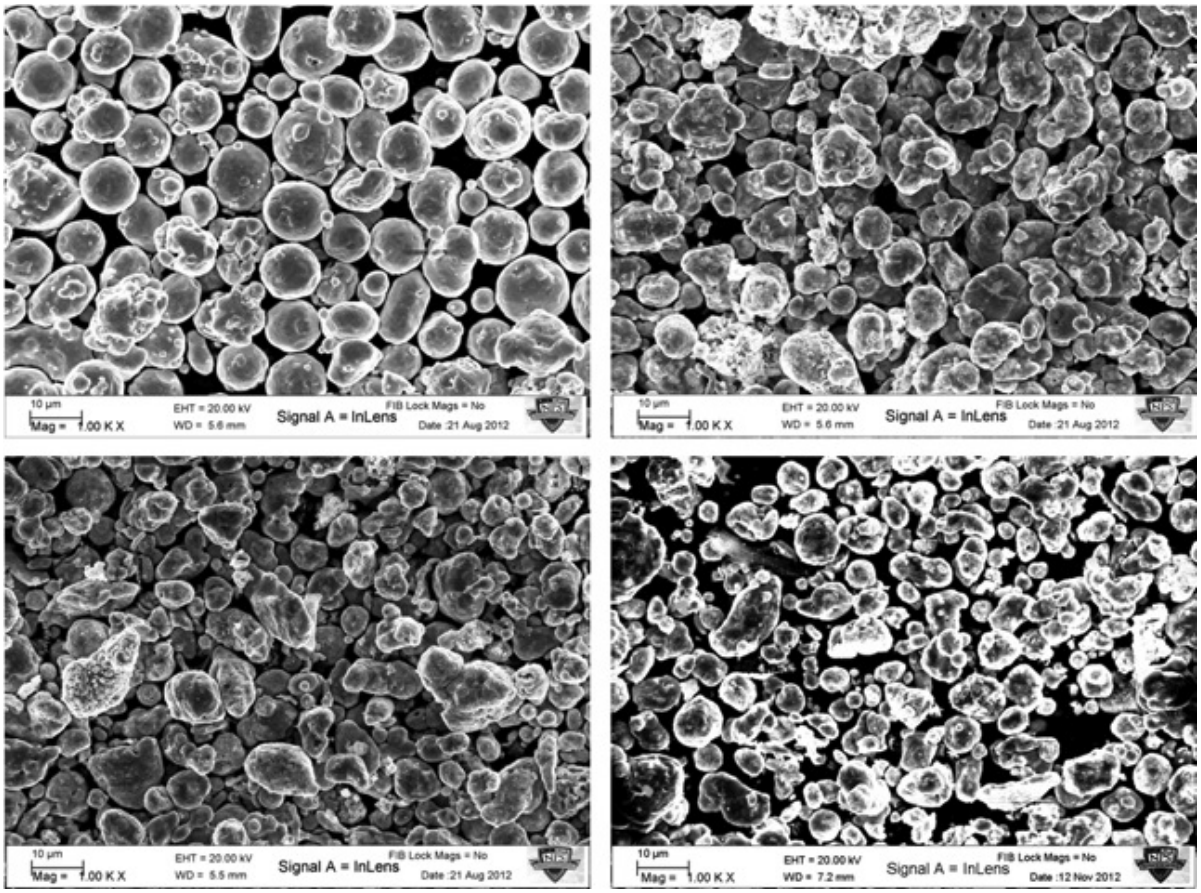

Figure 24. SEM Surface Photographs (1000x).Clockwise from Top Left: Pure Copper Powder, Cu-90/10 wt.% Zn, Cu-80/20 wt.% Zn and Cu-70/30 wt.% Zn.

A Horiba Laser Scattering Particle Size Analyzer (model no. LA-950V2) was utilized to verify the particle size distribution of each of the powders—the observed mean particle sizes of each of the powders are listed in Table 7, along with the powder compositions by weight percentage. This analysis provided greater detail than the sieve analysis acquired from ACu Powder, especially with respect to the distribution of particle size at magnitudes of less than 325 mesh (44 µm), but it should be noted that our particle size analysis was in strong agreement with ACu Powder's sieve analysis. Additionally, it is important to observe that the Cu-70/30 wt.% Zn powder had a mean particle size of anywhere between 40–60% smaller than the other powders which were procured.

Powder Material	Copper	Cu-90/10 wt.% Zn	Cu-80/20 wt.% Zn	Cu-70/30 wt.% Zn
Mean Particle Size (μm)	18.82	22.16	26.35	11.24
Composition, Cu / Zn (wt.%)	>99.5 (Pure)	90.61 / 9.39	78.93 / 21.07	68.34 / 31.66

Table 7. Observed Mean Particle Size and Composition for Each Powder, As Received.

The composition of each of the powders was determined via the use of the EDAX Spectroscopy system, manufactured by Ametek®, in conjunction with the Naval Postgraduate School's Zeiss Neon 40 model of scanning electron microscope. The EDAX Genesis software utilizes the ZAF matrix correction equation to quantify composition—by comparing the observed X-ray intensities versus expected X-ray intensities, both measured in counts, one can identify both the element being observed and the composition magnitude in comparison to other elements present. The equations below delineates the general equations the EDAX software uses in execution of this concept [45]:

(4) $$\frac{C_i}{C_{(i)}} = [ZAF]_i \frac{I_i}{I_{(i)}} = [ZAF]_i \, k_i$$

C_i = weight fraction of the element *i* of interest in the sample
$C_{(i)}$ = weight fraction of the element *i* in the standard

(5) $\frac{I_i}{I_{(i)}}$ = ratio of the unknown-to-standard intensities, also known as the "k-value"

$[ZAF]_i$ = matrix effects correction factor due to atomic number (Z), X-ray absorption (A), and X-ray fluorescence (F), which varies by element.

When performing the quantification of composition at a minimum twenty thousand counts were obtained, to minimize the error. Additionally, the Peak ID function was used to ensure that the software was identifying the correct elements (only Cu and Zn should be present, ignoring minute amounts of O). An example of the output spectra can be found in Figure 25. When considering only the surface of the particles, our analysis revealed that the composition of each of the powders was reasonably uniform. Five quantifications were performed for each of the feedstock powders, and all of the results were within +/- 1.40% of the average composition, again, listed in Table 6.

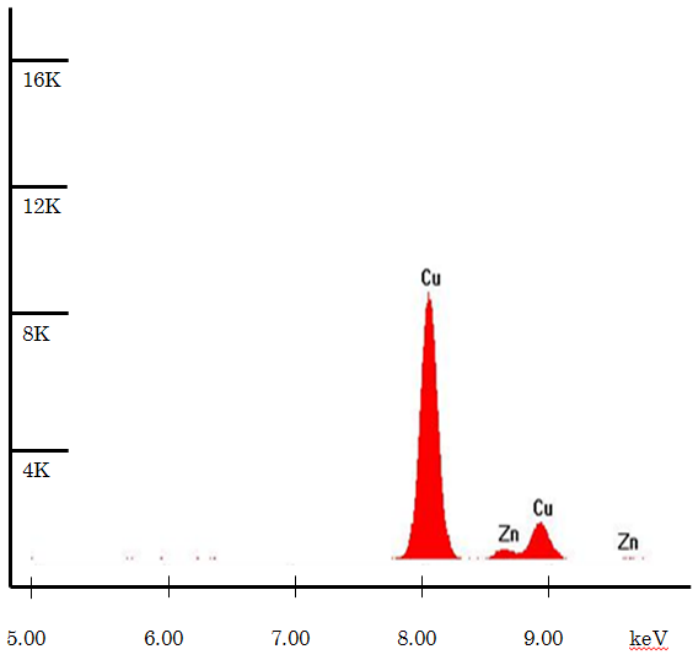

Figure 25. Output X-Ray Spectra, Counts Vs. Energy, for Cu-90/10 wt.% Zn Deposit, Sprayed at 250 psi and 450 °C.

In addition to characterizing the surface of the powders, the internal morphology and compositions of powder particles were also characterized. Cross sectional samples of the powders were produced by mixing the powders in epoxy molds with approximately equal amounts with cold mounting epoxy, poured into 1 ¼" mounting molds and left for fifteen minutes to cure. After curing, each of the sample mounts were sanded flat with a Buehler Ecomet 3 variable speed grinder-polisher using a sequence of 400, 600 1200, and 2000 grit grinding paper—each individual step being performed with water flow at a machine speed of 240 RPM, a sample pressure of 10 lbf and a total sanding time of 6 minutes. After ensuring the sample mounts were completely flat, each sample was polished on the same machine with 5 µm, 3 µm and 1 µm diamond grit, with the final polish being completed on the Buehler VibroMet 2 vibratory polisher in conjunction with 0.05 µm colloidal silica as the polishing media, which doubled as a very mild etching agent. After polishing, each sample was cleaned in a bath of methanol using a Buehler Ultramet 2005 ultrasonic cleaner for a duration 20 minutes, dried with a heat gun, and left overnight in a Pelco 2251 model vacuum desiccator which was kept at vacuum.

Quite interestingly, the internal morphologies of the Cu-Zn Series powders were markedly different than what was observed when considering only the surface of the powders. First, by viewing the cross sections of the individual powder particles, it was discovered that the all of the Cu-Zn series powders possessed substantial amounts of internal micro-porosity within the particles themselves (Figure 26). Even further, it was found that the composition of the powders was more variable than what the batch analysis conducted by ACu Powder, or the general surface analysis. Spot X-ray spectroscopy of ten independent locations within each of the images contained in Figure 26 revealed that composition of the Cu-90/10 wt.% Zn powder deviated in some places by as much 4.86 wt.% Zn from the nominal composition (48%), the Cu-80/20 wt.% Zn powder by as much as 6.26 wt.% (31%), and the Cu-70/30 wt.% Zn powder by as much 7.23% (24%). Each spectroscopy analysis was conducted with a minimum of ten thousand counts in order to minimize signal errors. Additionally, a line analysis was conducted on a number of particles in each series of powder. By plotting the number of zinc counts divided by the number of copper counts in evenly spaced points along the line gave a rough estimate of the uniformity of composition over a distance (Figure 27). The results showed that while there were some clear statistical outliers, the large majority of the composition was relatively constant within, fluctuating approximately within the range previously obtained by independent X-ray microanalysis. Clearly, the addition of further zinc aids the diffusion process during ACu Powder's production process, and allows for a more uniform powder. However, it should be noted that averages of the ten random spot compositions were all less than 2% off the previously obtained surface composition analysis—thus the powder was indeed reasonably uniform with respect to zinc distribution from particle to particle, but rather exhibited compositional non-uniformity within each particle itself. Spectroscopy maps for the Cu-90/10 wt.% Zn and Cu-70/30 wt.% Zn powder cross sections are exhibited in Figures 28–29, respectively, to provide a visual reinforcement of this finding—zinc concentrations are displayed in the green tint, while copper concentrations are displayed in the purple tint.

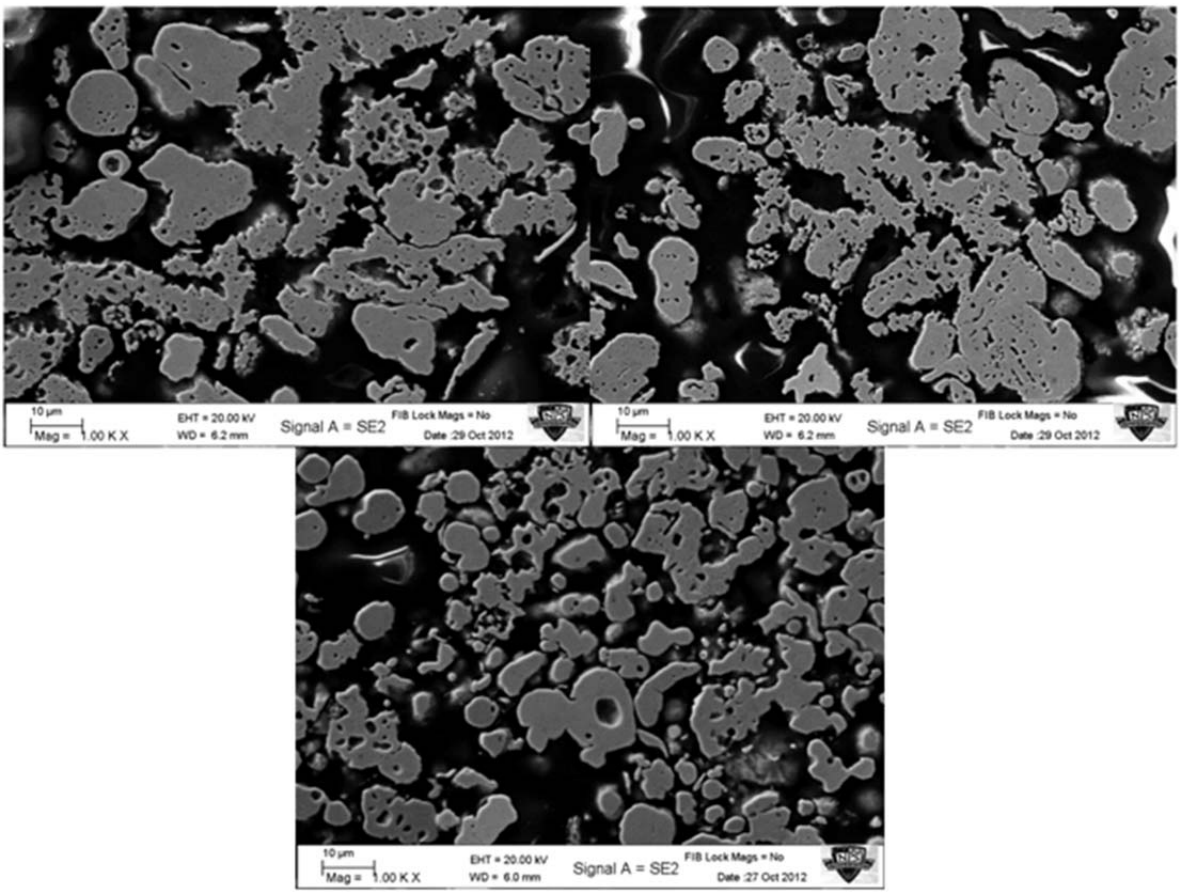

Figure 26. SEM Cross-Sectional Photographs (1000x) of the As Received Brass Powders, Clockwise from Top Left: Cu-90/10 wt.% Zn, Cu-80/20 wt.% Zn, Cu-70/30 wt.% Zn.

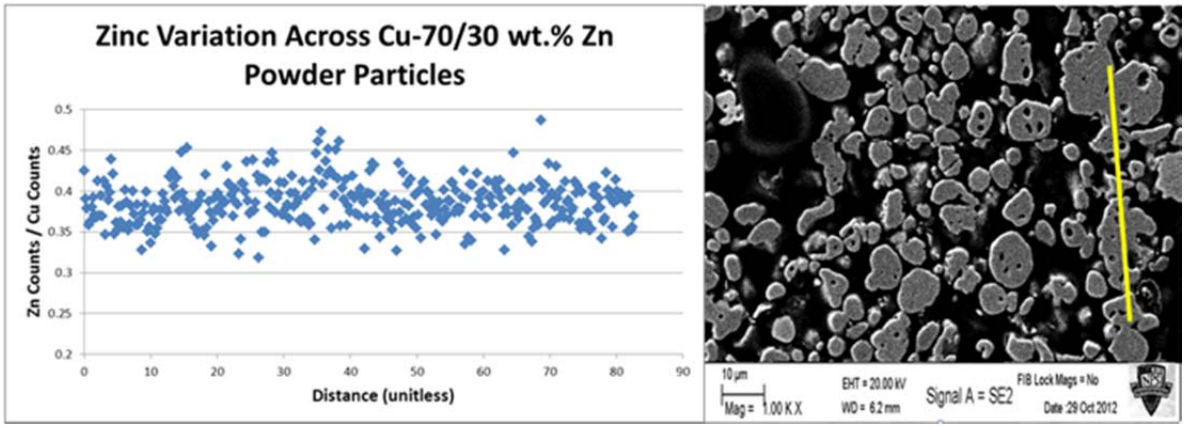

Figure 27. Left: Zinc X-Ray Counts / Copper X-Ray Counts vs. Distance, As Received Cu-70/30 wt.% Zn Powder. Right: Line Map from which Data on the Left was Retrieved.

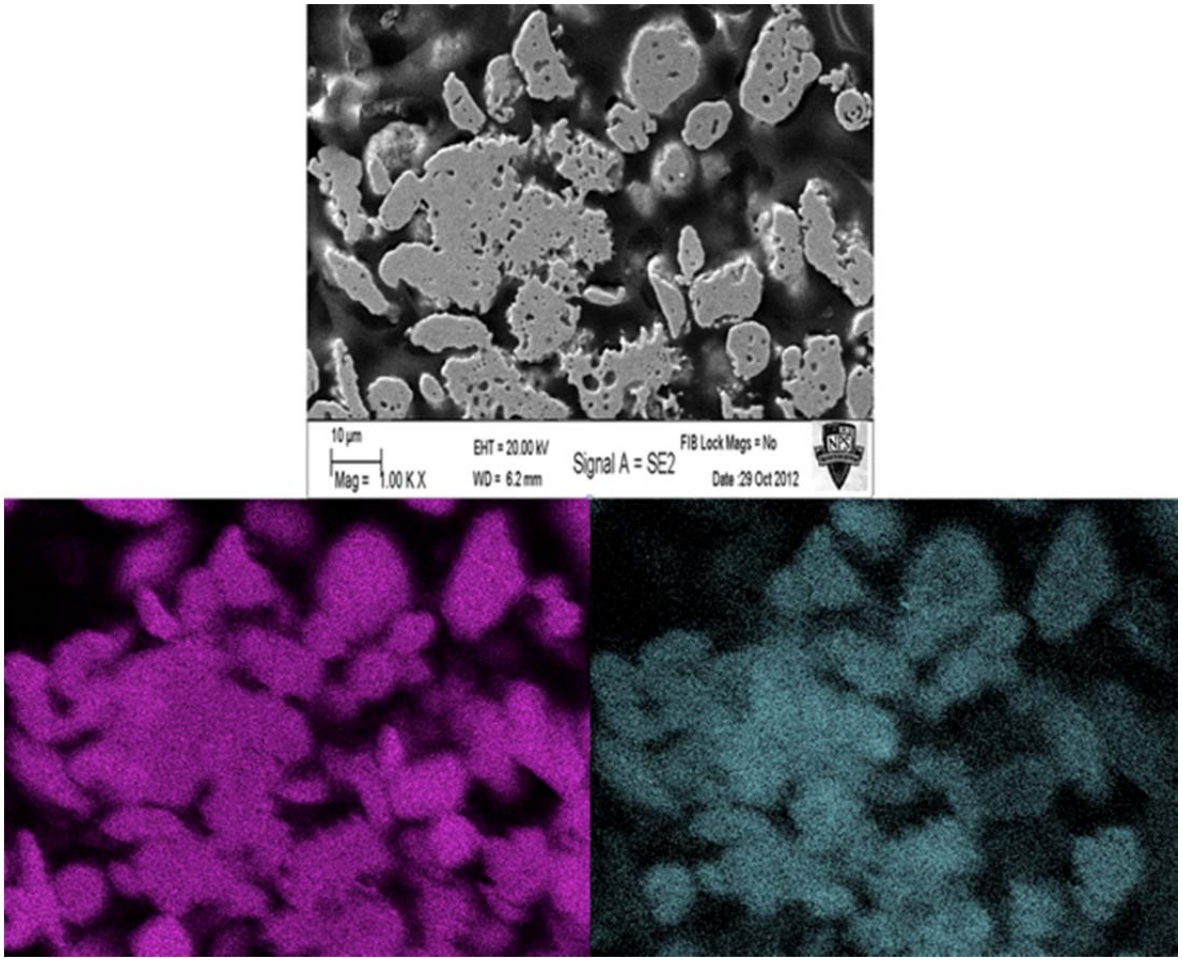

Figure 28. Cross-Sectional Spectrograph Maps and SEM Image (1000x) for Cu-90/10 wt.% Zn Powder, As Received. Top Center: SEM Image. Bottom Left: Cu X-Ray Elemental Map. Bottom Right: Zn X-Ray Elemental Map.

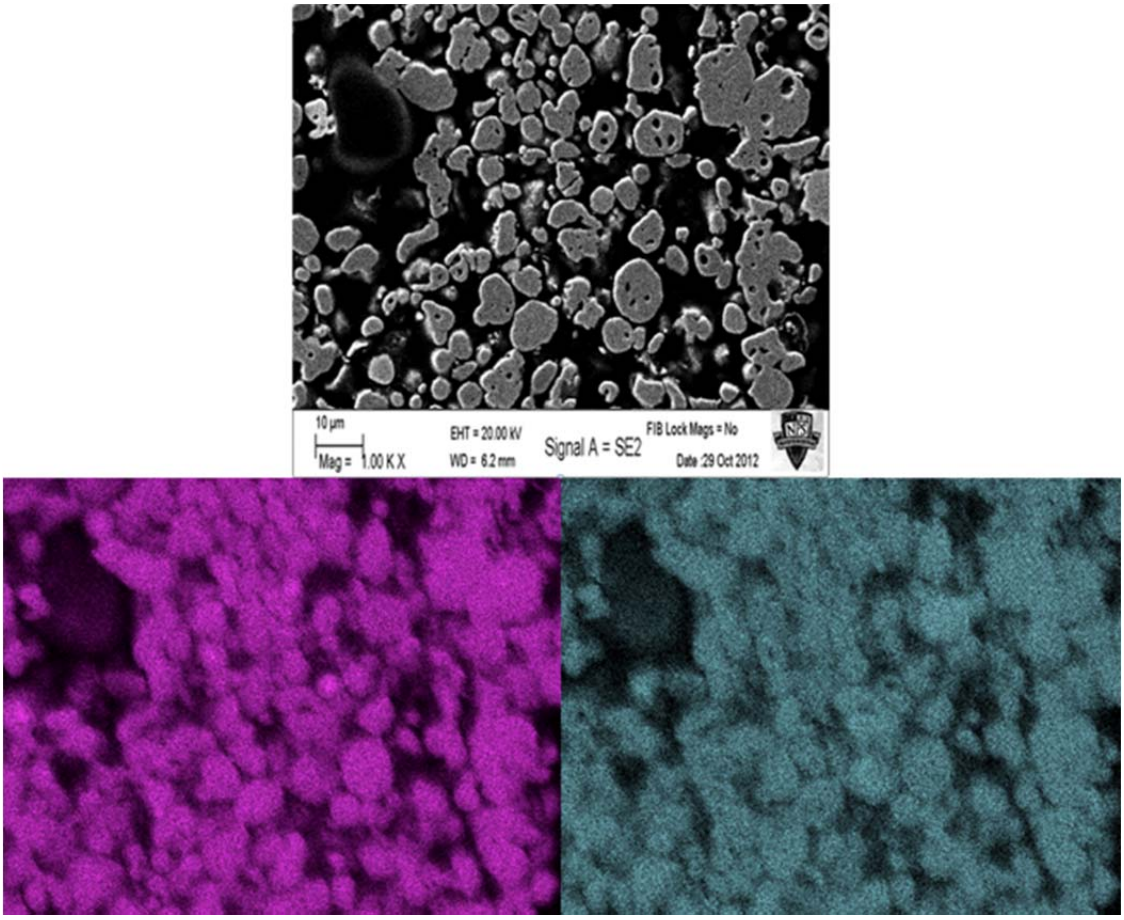

Figure 29. Cross-Sectional Spectrograph Maps and SEM Image (1000x) for Cu-70/30 wt.% Zn Powder, As Received. Top Center: SEM Image. Bottom Left: Cu X-ray Elemental Map. Bottom Right: Zn X-ray Elemental Map.

B. EXPERIMENTAL METHODS

Using the powders described in III.A, cold spray deposition was performed varying temperature and pressure. These cold spray experiments were performed with the system described in detail in chapter II. Other parameters, such as nozzle stand-off distance, nozzle material and substrate roughness, were kept constant and are listed in Table 9; The same spray pattern as delineated in the calibration experiments was chosen, with a gun step over per pass of 1.2 mm, a gun traverse speed of 40 mm/s and ten total passes. Two spray pressures (250 psi and 175 psi [1.72 MPa and 1.21 MPa]) were chosen along with two spray temperatures (450 °C and 300 °C). These temperatures represent a significant fraction of the melting point of each alloy as is shown in Table 8. For each

test, two identical spray patterns were conducted, the latter directly over the top of the previous. The spray pattern passes were conducted immediately right after each other, leaving very little time for the material to cool in between the deposition action of the individual spray patterns.

Powder Material	Copper	Cu-90/10 wt.% Zn	Cu-80/20 wt.% Zn	Cu-70/30 wt.% Zn
Melting Point (°C)	1085	1030	980	930
Melting Point (% of Cu)	100.00	94.93	90.32	85.71
350 °C (% of Melting Point)	32.26	33.98	35.71	37.63
450 °C (% of Melting Point)	41.47	43.69	45.92	48.39

Table 8. The Melting Points of Copper, Cu-90/10 wt.% Zn, Cu-80/20 wt.% Zn and Cu-70/30 wt.% Zn.

Gas (Air, N_2 or He)	N_2
Substrate Material	T-6061 Al
Substrate Surface (SB or Smooth)	SB
Nozzle Type (WC or Polymer)	WC
Gun Type	Automatic
Gas Temperature (^oC)	450, 300
Gas Pressure (psi)	250, 175
Powder Feed Rate (g/min)	21.94
Gun Stand-off Distance (mm)	15
Gun Traverse Speed (mm/s)	40
Gun Step Over per Pass (mm)	1.2
Gun Total Passes	10

Table 9. Cold Spray Parameters Utilized During Copper and Brass Experiments.

Deposition efficiency was recorded by measuring the mass of the total deposit plus substrate after spray, and dividing this quantity by the total amount of powder fed into the system throughout the spray—a quantity obtained by multiplying the known powder feed rate by the total spray time, which was measured by handheld stopwatch. Deposit thickness was measured via the use of a digital micrometer, and all measurements were taken from the side of the deposit which possessed the thickest section of coating (the area of the final spray pass). Because two spray passes were done

per each test, the deposition efficiency is an average of the two passes. Additionally, the coating thickness measured was divided in half to determine the coating thickness per pass.

After conducting the measurements for coating thickness and deposition efficiency, each sample was cut into 20 mm long samples with a Struers Secotom-10 diamond saw. The cross section of each sample was then hot-mounted into 1 ¼" diameter non-conducting epoxy pucks with a Buehler Simplimet 2 mounting press. Each sample mount was sanded flat with a Buehler Ecomet 3 variable speed grinder-polisher using a sequence of 400, 600 1,200, and 2,000 grit grinding paper—each individual step being performed with water flow at a machine speed of 240 RPM, a sample pressure of 10 lbf and a total sanding time of 6 minutes. After ensuring the sample mounts were completely flat, each sample was polished on the same machine with 5 µm, 3 µm and 1 µm diamond grit, with the final polish being completed on the Buehler VibroMet 2 vibratory polisher in conjunction with 0.05 µm colloidal silica as the polishing media, which doubled as a very mild etching agent. All polishing was conducted on Buehler Microcloths (P/N 40–7218). After polishing, each sample was cleaned in a bath of methanol using a Buehler Ultramet 2005 ultrasonic cleaner for a duration 20 minutes, dried with a heat gun, and left overnight in a Pelco 2251 model vacuum desiccator which was kept at vacuum.

Optical microscopy was conducted for each of the samples using a Nikon POTIPHOT 200 Series microscope and digital camera. Images were taken at the 25x, 100x, 200x and 500x magnification levels, largely detailing the microstructure of the deposits.

Hardness was measured via the utilization of a G200 Series nano-indenter, with a Berkovich diamond indenter tip, manufactured by Agilent Technologies Inc. Agilent Nanosuite software was used for indentation data analysis and compilation. In each hardness measurement sample, fifty data points were taken to ensure faulty data points could be removed while maintaining the ability to give a measurement of material hardness with a high confidence level. The parameters for the indents were as follows:

0.05 nm/s allowable drift rate, 3.0 hr maximum thermal drift time, 2000 nm surface approach distance, 200 nm/s surface approach velocity, 1000 nm indentation depth and 0.08 strain rate.

Porosity was measured using the software ImageJ, developed by the National Institutes of Health and available as freeware. Both optical and scanning electron images were uploaded into the software, where they were modified to binary format (black and white) after modifying the image boundaries to contain the area of interest. After completing that task, the installed software was used to evaluate the ratio of porosity (black) to deposit material (greyscale). A 25x magnification was used during every evaluation to limit any pronounced user-manufactured error. An example of how this software analyzes porosity can be found in Figure 30.

Lastly, SEM photographs of the deposit at the substrate/deposit interface were taken at 500x magnification, and composition analysis was performed utilizing the EDAX spectroscopy software in conjunction with Zeiss Neon-40 scanning electron microscope. For qualitative analysis, composition maps were generated by way of a 512x400 pixel resolution map, where the X-ray counts from each pixel were tallied for 400 µs—the procedure creating a single frame. Multiple frames were taken, 256 in total, and then overlapped over each other to provide a high fidelity and high contrast map—the process took approximately six hours for each map. To compliment these results and establish a quantitative perspective, twenty points in each area of concern were chosen for a more specific evaluation, where the number of total X-ray counts was increased to ten thousand, in order to minimize error. Ten of these points were in the general bulk material, and ten lay in close proximity (2 µm or less) to deposit porosity, the specifics of which are discussed in the following sections. Theses twenty points were utilized to generate the numeric statistics used for discussion.

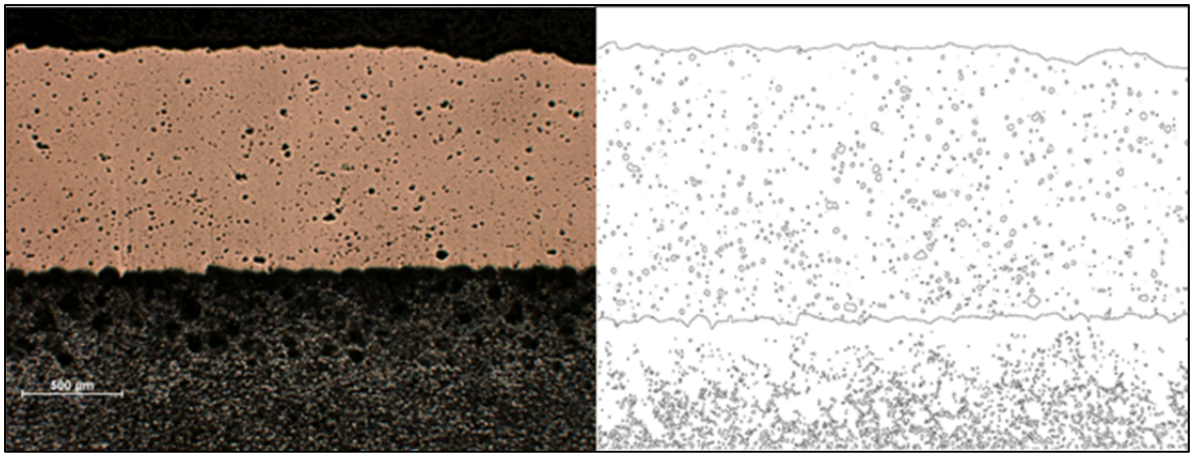

Figure 30. Left: Optical Image of Pure Copper Deposit (Sprayed at 250 psi, 450 °C). Right: Sample of ImageJ Porosity Analysis on the Same Deposit.

C. RESULTS

1. Deposition Efficiency and Coating Thickness Per Pass

All of the brass alloys were successfully deposited via the cold spray method. The resultant data for the spray experiments is listed for the pure copper, Cu-90/10 wt.% Zn, Cu-80–20 wt.% Zn and Cu-70/30 wt.% Zn powders in Tables 10, 11, 12 and 13, respectively. The deposition efficiency was found to be a strong function of zinc content (Figures 31 and 32). Deposition efficiency and coating thickness per pass increased by 67.6% and 57.4%, respectively, as zinc content was increased from 0–10 wt.%, but then decreased as zinc content was increased further. As zinc content was enlarged from 10–20 wt.% deposition efficiency and coating thickness per pass decreased by 29.8% and 22.4%, respectively, and from 20–30 wt.% the quantities decreased by a further 36.5% and 18.1%, respectively.

Test No.	1	2	3	4
Powder Material	Pure Copper	Pure Copper	Pure Copper	Pure Copper
Gas (Air, N_2 or He)	N_2	N_2	N_2	N_2
Substrate Material	SB T-6061 Al	SB T-6061 Al	SB T-6061 Al	SB T-6061 Al
Gun Type	Automatic	Automatic	Automatic	Automatic
Gas Temperature (^oC)	300	450	300	450
Gas Pressure (psi)	175	175	250	250
Powder Feed Rate (g/min)	21.94	21.94	21.94	21.94
Gun Stand-off Distance (mm)	15	15	15	15
Gun Traverse Speed (mm/s)	40	40	40	40
Gun Step Over per Pass (mm)	1.2	1.2	1.2	1.2
Deposition Efficiency (%)	5.9	23.1	18.1	33.6
Coating Thickness per Pass (µm)	95	370	320	610

Table 10. Spray Data for Pure Copper Powder.

Test No.	1	2	3	4
Powder Material	Cu-90/10 wt.% Zn	Cu-90/10 wt.% Zn	Cu-90/10 wt.% Zn	Cu-90/10 wt.% Zn
Gas (Air, N_2 or He)	N_2	N_2	N_2	N_2
Substrate Material	SB T-6061 Al	SB T-6061 Al	SB T-6061 Al	SB T-6061 Al
Gun Type	Automatic	Automatic	Automatic	Automatic
Gas Temperature (^oC)	300	450	300	450
Gas Pressure (psi)	175	175	250	250
Powder Feed Rate (g/min)	21.94	21.94	21.94	21.94
Gun Stand-off Distance (mm)	15	15	15	15
Gun Traverse Speed (mm/s)	40	40	40	40
Gun Step Over per Pass (mm)	1.2	1.2	1.2	1.2
Deposition Efficiency (%)	15.7	34.3	34.2	56.3
Coating Thickness per Pass (µm)	255	575	575	960

Table 11. Spray Data for Cu-90/10 wt.% Zn Powder.

Test No.	1	2	3	4
Powder Material	Cu-80/20 wt.% Zn	Cu-80/20 wt.% Zn	Cu-80/20 wt.% Zn	Cu-80/20 wt.% Zn
Gas (Air, N_2 or He)	N_2	N_2	N_2	N_2
Substrate Material	SB T-6061 Al	SB T-6061 Al	SB T-6061 Al	SB T-6061 Al
Gun Type	Automatic	Automatic	Automatic	Automatic
Gas Temperature (^oC)	300	450	300	450
Gas Pressure (psi)	175	175	250	250
Powder Feed Rate (g/min)	21.94	21.94	21.94	21.94
Gun Stand-off Distance (mm)	15	15	15	15
Gun Traverse Speed (mm/s)	40	40	40	40
Gun Step Over per Pass (mm)	1.2	1.2	1.2	1.2
Deposition Efficiency (%)	1.6	24.7	25.7	39.5
Coating Thickness per Pass (µm)	30	450	470	745

Table 12. Spray Data for Cu-80/20 wt.% Zn Powder.

Test No.	1	2	3	4
Powder Material	Cu-70/30 wt.% Zn	Cu-70/30 wt.% Zn	Cu-70/30 wt.% Zn	Cu-70/30 wt.% Zn
Gas (Air, N_2 or He)	N_2	N_2	N_2	N_2
Substrate Material	SB T-6061 Al	SB T-6061 Al	SB T-6061 Al	SB T-6061 Al
Gun Type	Automatic	Automatic	Automatic	Automatic
Gas Temperature (^oC)	300	450	300	450
Gas Pressure (psi)	175	175	250	250
Powder Feed Rate (g/min)	21.94	21.94	21.94	21.94
Gun Stand-off Distance (mm)	15	15	15	15
Gun Traverse Speed (mm/s)	40	40	40	40
Gun Step Over per Pass (mm)	1.2	1.2	1.2	1.2
Deposition Efficiency (%)	< 1.0	12.9	7.9	25.1
Coating Thickness per Pass (µm)	< 30	360	290	610

Table 13. Spray Data for Cu-70/30 wt.% Zn Powder.

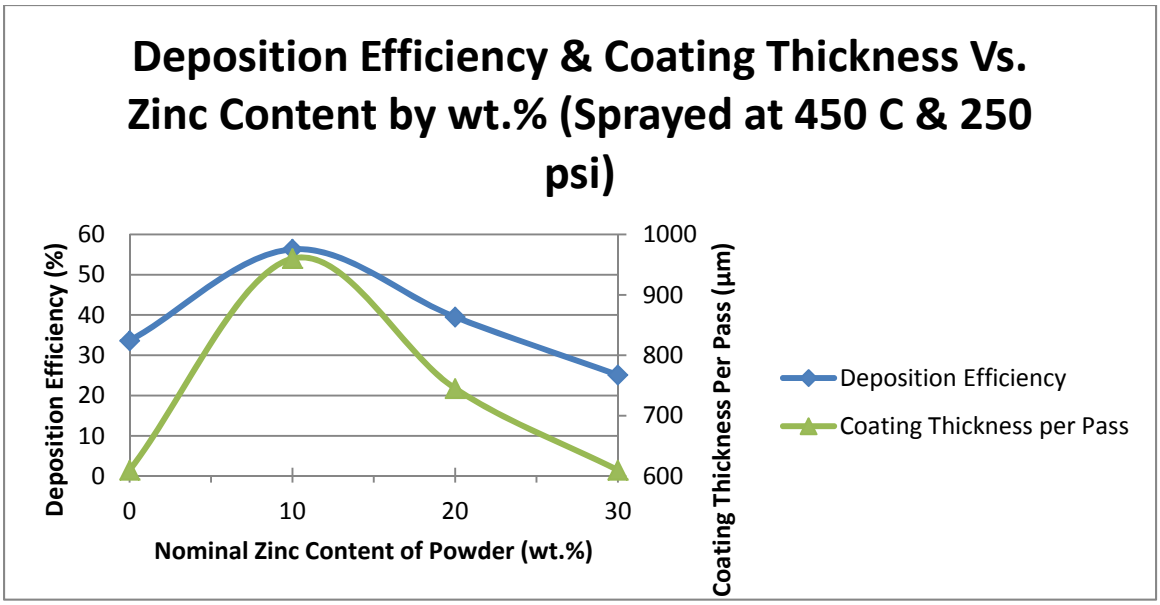

Figure 31. Deposition Efficiency and Coating Thickness Vs. Zinc Content by wt.%, with a Spray Pressure of 250 psi and a Spray Temperature of 450 °C.

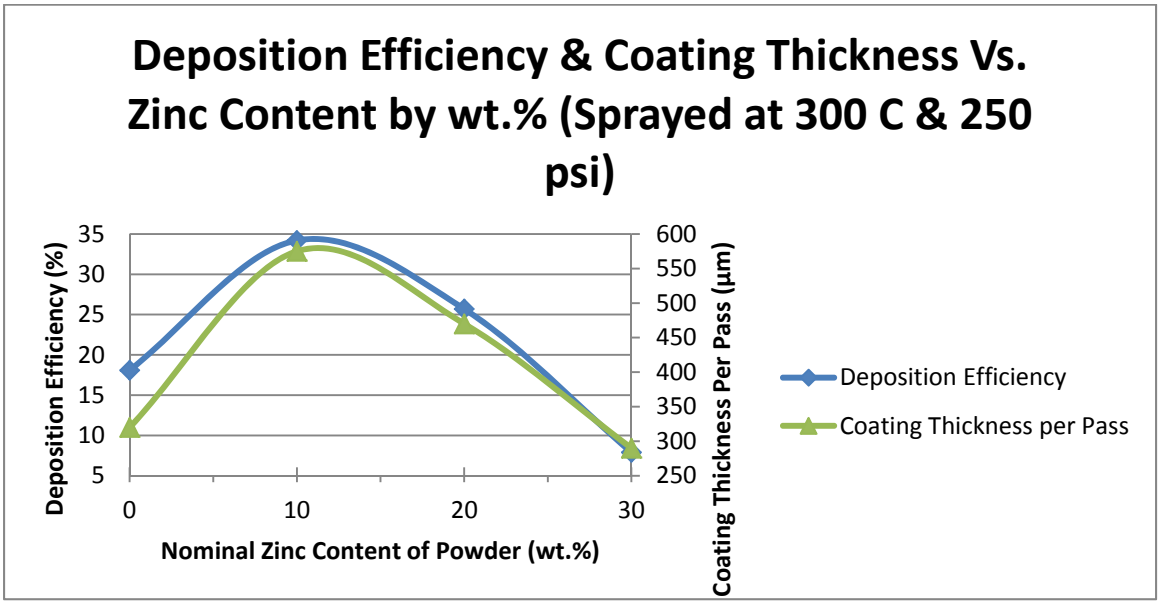

Figure 32. Deposition Efficiency and Coating Thickness Vs. Zinc Content by wt.%, with a Spray Pressure of 250 psi and a Spray Temperature of 300 °C.

For all of the feedstock powders used, regardless of zinc content and for all other parameters assumed constant, there is a clear and definitive increase in deposition efficiency and coating thickness when either gas pressure and/or gas temperature is increased. Figures 33–36 provide visual representation of the relationships between deposition output and spray pressure and temperature in 3-D surface plots. For a constant pressure of 250 psi [1.72 MPa], as gas temperature is raised from 300 °C to 450 °C, a 50% increase, deposition efficiency increases on average by 68.0% with a standard deviation of 13.3%, while coating thickness increases on average by 72% with a standard deviation of 13.6%. For a constant temperature of 450 °C, as gas pressure is raised from 175 psi [1.21 MPa] to 250 psi [1.72 MPa], a 43% increase, deposition efficiency increases on average by 56.5% with a standard deviation of 8.7% while coating thickness increases on average by 65.8% with a standard deviation of only 0.9%. Of special note however is that none of these calculations include the data points from the Cu-70/30 wt.% Zn deposits; this is because the Cu-70/30 wt.% Zn deposits were erratic and brittle while being sprayed, with small pieces and in some cases entire chunks of the deposit breaking off in mid-spray in the two middle-range spray conditions. This deposit behavior was not observed during the sprays of the other feedstock materials, although there were some instances of very slight, yet perceptible upon inspection, debonding of the deposit from the substrate in the Cu-80/20 wt.% Zn deposits, most notably at the lower pressure sprays conducted at 175 psi [1.21 MPa].

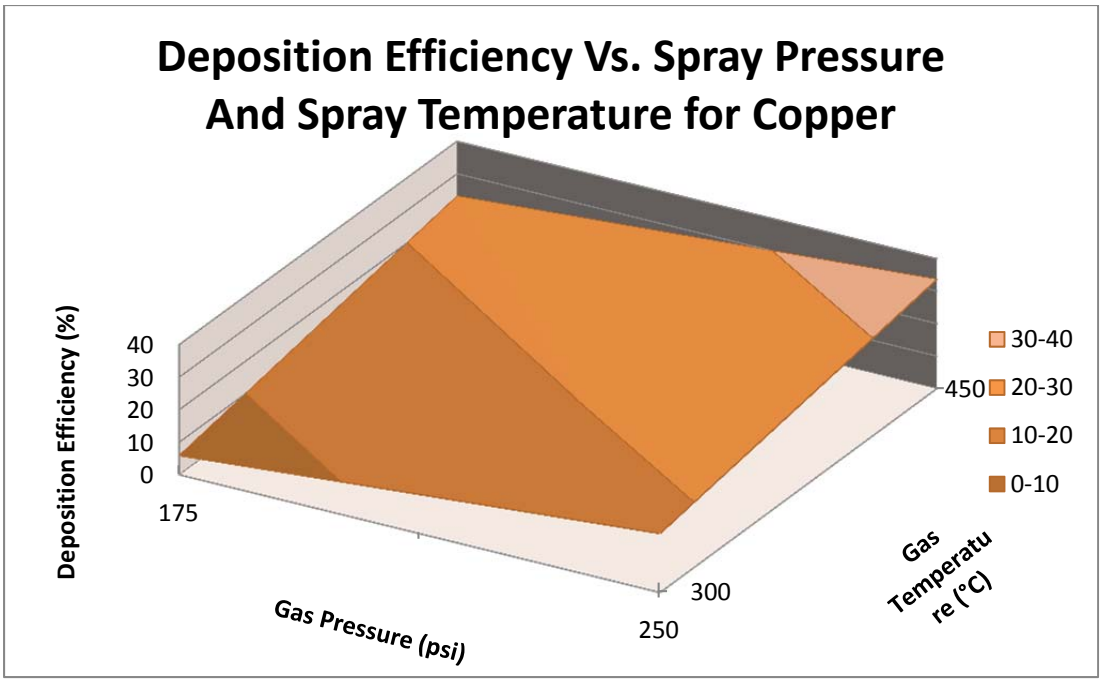

Figure 33. Three Dimensional Surface Plot of Deposition Efficiency Vs. Spray Pressure and Temperature for Pure Copper Powder.

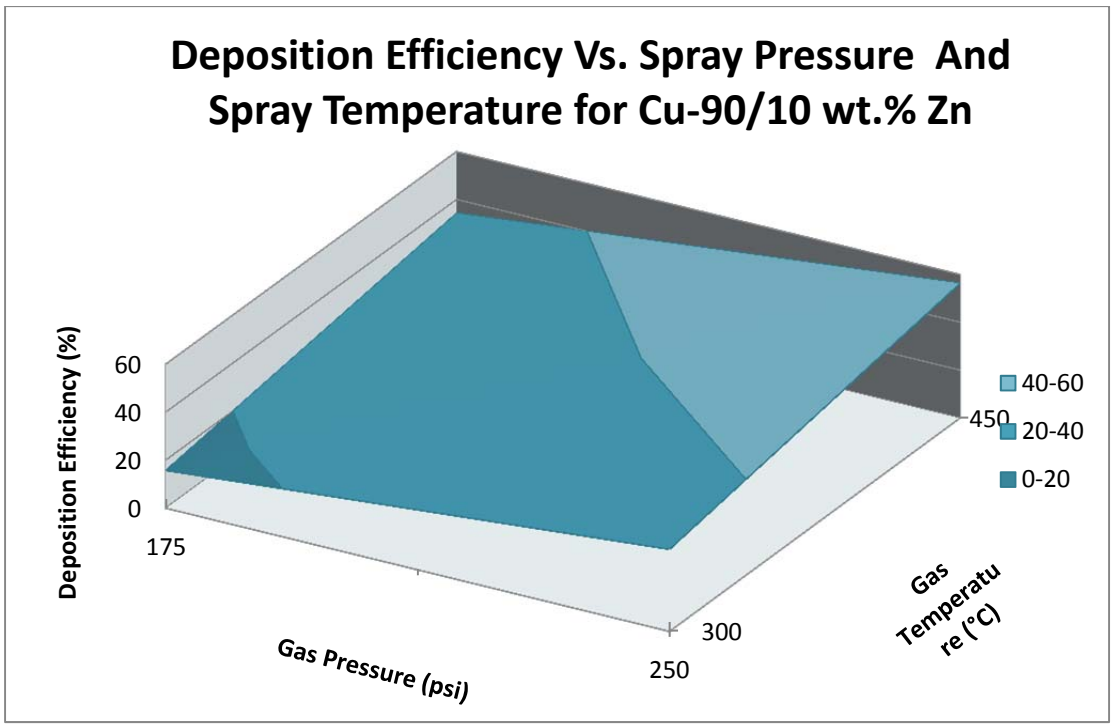

Figure 34. Three Dimensional Surface Plot of Deposition Efficiency Vs. Spray Pressure and Temperature for Cu-90/10 wt.% Zn Powder.

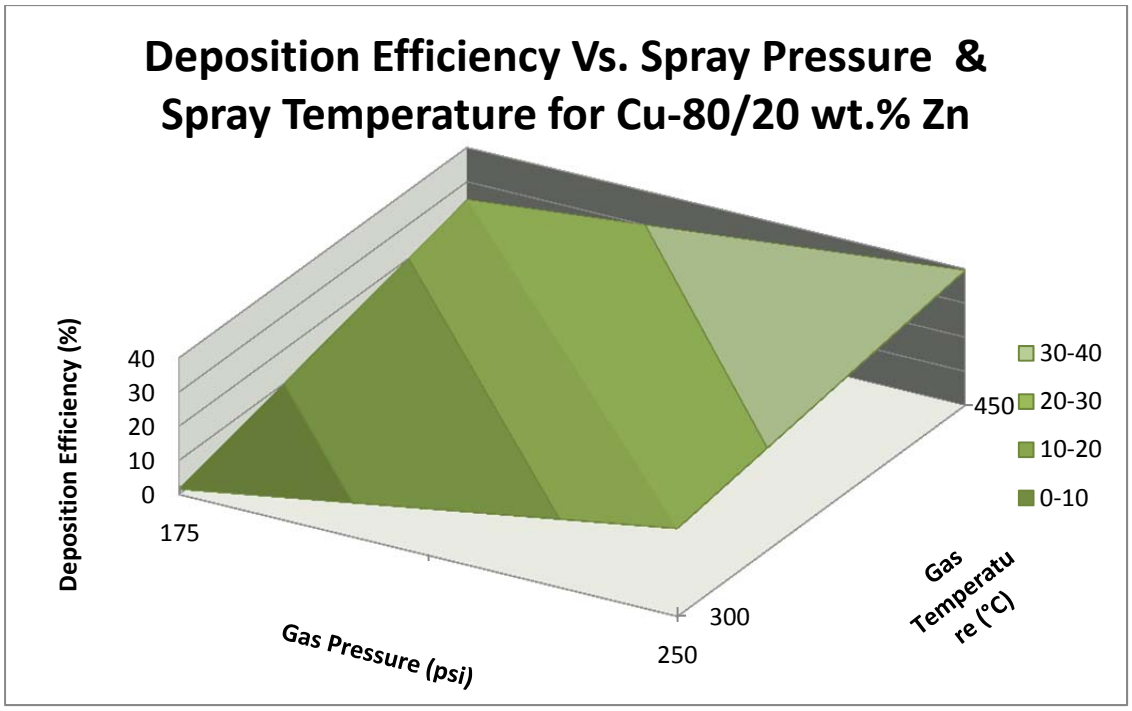

Figure 35. Three Dimensional Surface Plot of Deposition Efficiency Vs. Spray Pressure and Temperature for Cu-80/20 wt.% Zn Powder.

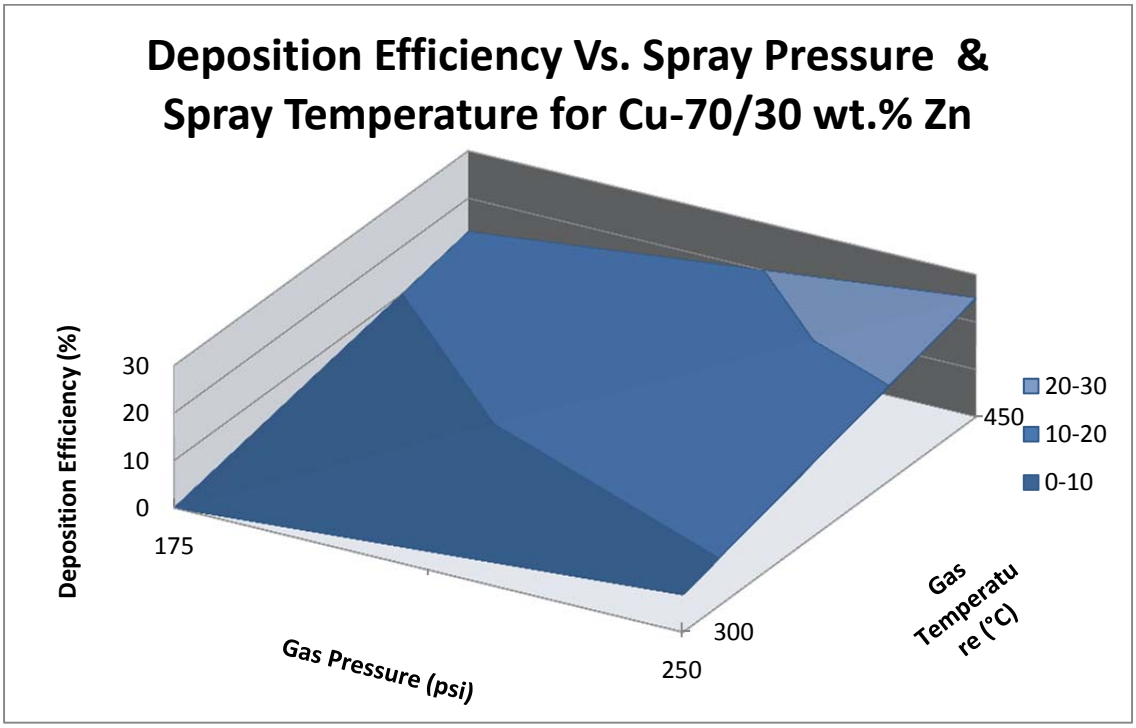

Figure 36. Three Dimensional Surface Plot of Deposition Efficiency Vs. Spray Pressure and Temperature for Cu-70/30 wt.% Zn Powder.

2. Deposit Hardness and Modulus of Elasticity

The deposit hardness increased systematically with increasing zinc content of the feedstock powder for the 450 °C case, while the 300 °C case presented a similar but less clear trend (Figure 37). The modulus of elasticity behaved in a similar manner as hardness, yet in the opposite direction, systematically decreasing with increasing zinc content in the 250 psi [1.72 MPa] and 450 °C spray conditions case (Figure 38). As zinc content increased, it became increasingly more difficult to obtain accurate data and there was increasingly larger material compliance issues when measuring hardness and modulus of elasticity. Table 14 contains the average hardness and young's modulus data obtained via nano-indentation for each of the deposits sprayed at 250 psi [1.72 MPa], both at 450 °C and 300 °C.

Test No.	1	2	3	4
Powder Material	Pure Copper	Pure Copper	Cu-90/10 wt.% Zn	Cu-90/10 wt.% Zn
Gas Temperature (°C)	450	300	450	300
Gas Pressure (psi)	250	250	250	250
Average Hardness (GPa)	2.75	2.43	3.01	2.61
Average Young's Modulus (GPa)	132.0	126.3	130.7	114.1
Test No.	5	6	7	8
Powder Material	Cu-80/20 wt.% Zn	Cu-80/20 wt.% Zn	Cu-70/30 wt.% Zn	Cu-70/30 wt.% Zn
Gas Temperature (°C)	450	300	450	300
Gas Pressure (psi)	250	250	250	250
Average Hardness (GPa)	3.21	3.11	3.31	2.67
Average Young's Modulus (GPa)	120.1	118.4	106.2	90.0

Table 14. Hardness and Young's Modulus for Pure Copper, Cu-90/10 wt.% Zn, Cu-80/20 wt.% Zn and Cu-70/30 wt.% Zn Deposits.

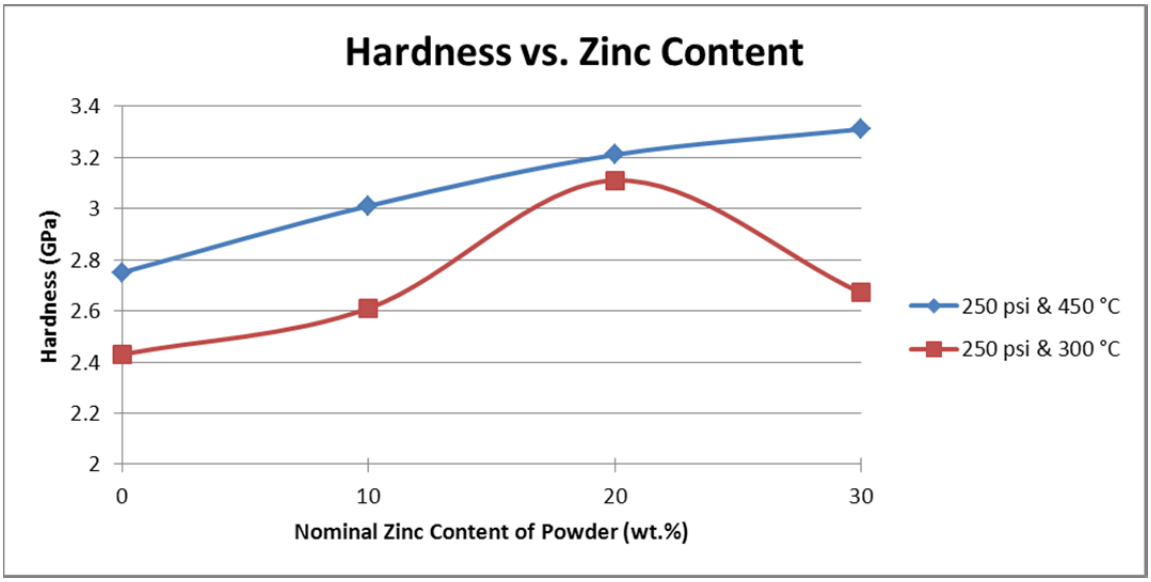

Figure 37. Average Hardness Vs. Zinc Content by wt.% for Deposits Sprayed at 250 psi and 450 °C, and 250 psi and 300 °C.

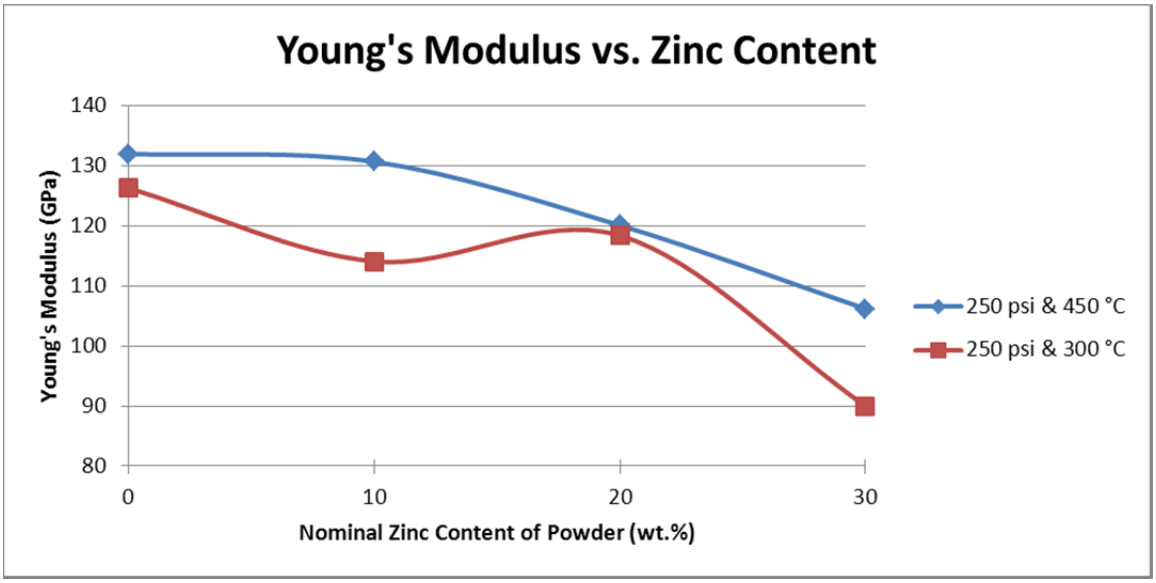

Figure 38. Average Young's Modulus Vs. Zinc Content by wt.% for Deposits Sprayed at 250 psi and 450 °C, and 250 psi and 300 °C.

3. Deposit Porosity

Deposit porosity was characterized by both optical and scanning electron microscopy (Table 15). Figures 39–42 provide optical microscope photos of the cross sections of the 250 psi [1.72 MPa] / 450 °C and 300 °C deposits, and Figure 43 provides

the scanning electron microscope photos of the 250 psi [1.72MPa] / 450 °C variants of the same. In every observable sample, the porosity as noted by the optical microscope far exceeded the porosity noted by the scanning electron microscope. Of particular note is the relationship between deposit porosity and zinc content by wt.%, illustrated by Figure 44, which does not present a linearly defined and clear trend. Notable is the result that in the 300 °C case, the trend line for deposit porosity mimics strongly the trend line previously seen in the hardness measurements of the same.

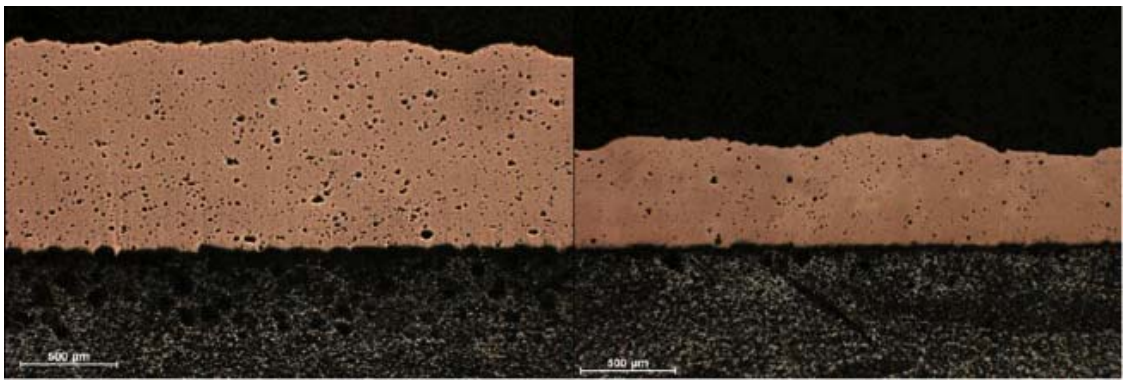

Figure 39. Optical Microscopy Photos of Pure Copper Spray Deposits, Mag 25X. Left: 250 psi, 450 °C. Right: 250 psi, 300 °C.

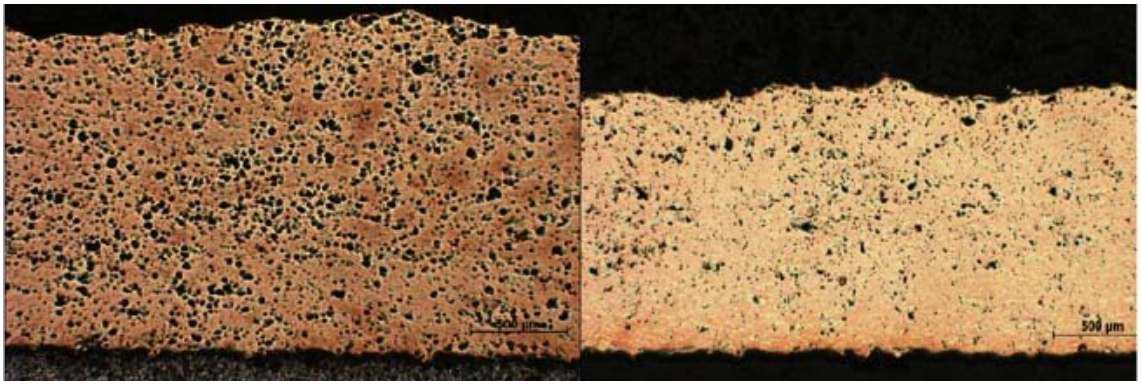

Figure 40. Optical Microscopy Photos of Cu-90/10 wt.% Zn Spray Deposits, Mag 25X. Left: 250 psi, 450 °C. Right: 250 psi, 300 °C.

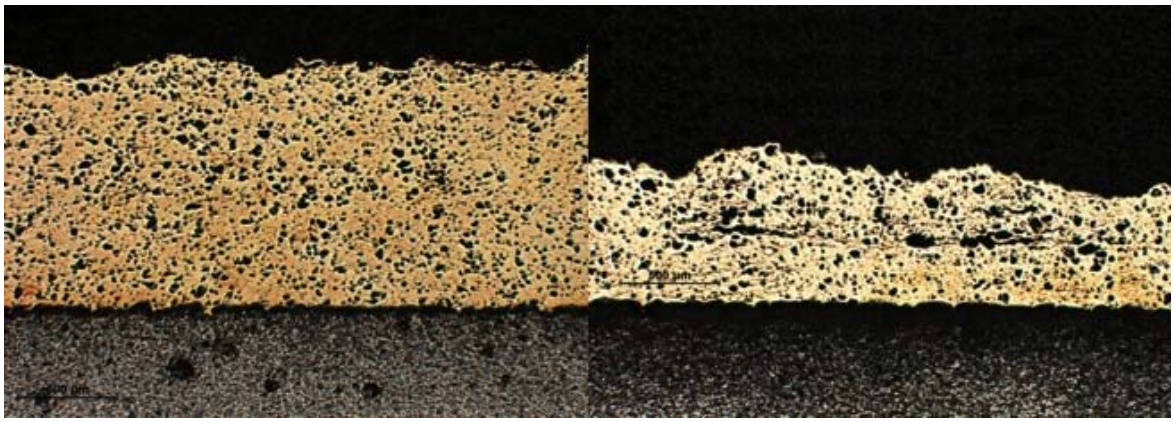

Figure 41. Optical Microscopy Photos of Cu-80/20 wt.% Zn Spray Deposits, Mag 25X. Left: 250 psi, 450 °C. Right: 250 psi, 300 °C.

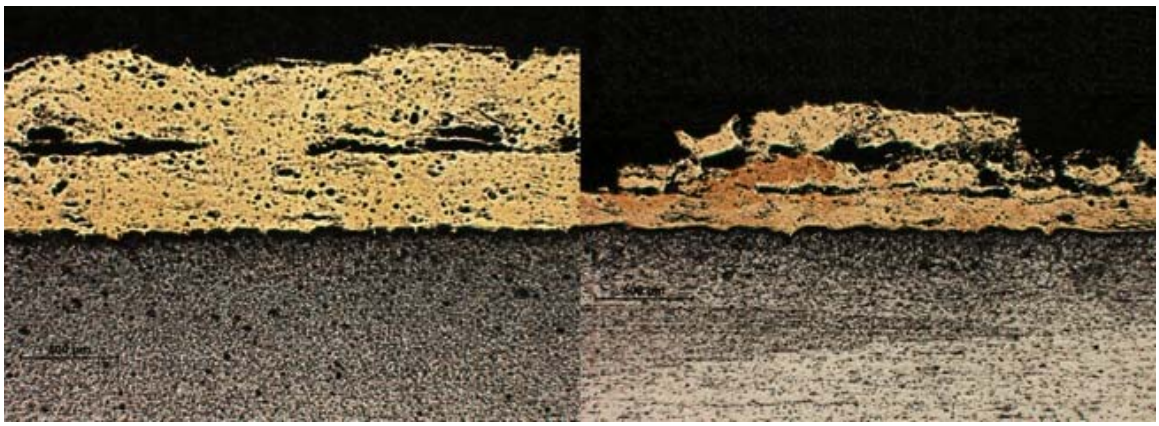

Figure 42. Optical Microscopy Photos of Cu-70/30 wt.% Zn Spray Deposits, Mag 25X. Left: 250 psi, 450 °C. Right: 250 psi, 300 °C.

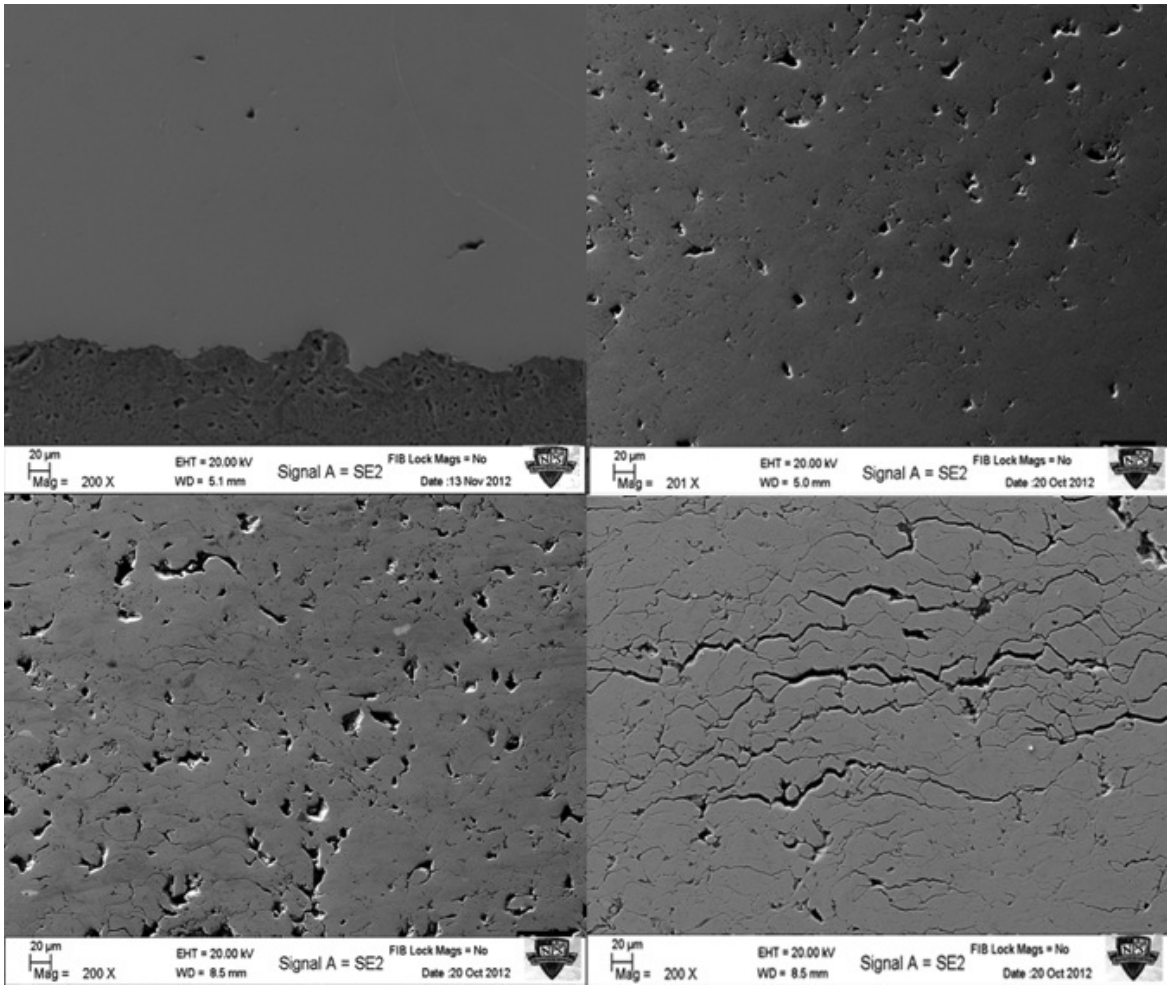

Figure 43. SEM Photos of Cold Spray Deposits, sprayed at 250 psi, 450 °C, Mag 200X. Clockwise from Top Left: Pure Copper, Cu-90/10 wt.% Zn, Cu-80/20 wt.% Zn, Cu-70/30 wt.% Zn.

Test No.	1	2	3	4
Powder Material	Pure Copper	Pure Copper	Cu-90/10 wt.% Zn	Cu-90/10 wt.% Zn
Gas Temperature (°C)	450	300	450	300
Gas Pressure (psi)	250	250	250	250
Porosity (% of Total Area)	4.94	3.65	25.63	11.9
Test No.	5	6	7	8
Powder Material	Cu-80/20 wt.% Zn	Cu-80/20 wt.% Zn	Cu-70/30 wt.% Zn	Cu-70/30 wt.%
Gas Temperature (°C)	450	300	450	300
Gas Pressure (psi)	250	250	250	250
Porosity (% of Total Area)	29.5	26.6	22.96	17.69

Table 15. Spray Data for Porosity in Pure Copper, Cu-90/10 wt.% Zn, Cu-80/20 wt.% Zn and Cu-70/30 wt.% Zn Cold Spray Deposits.

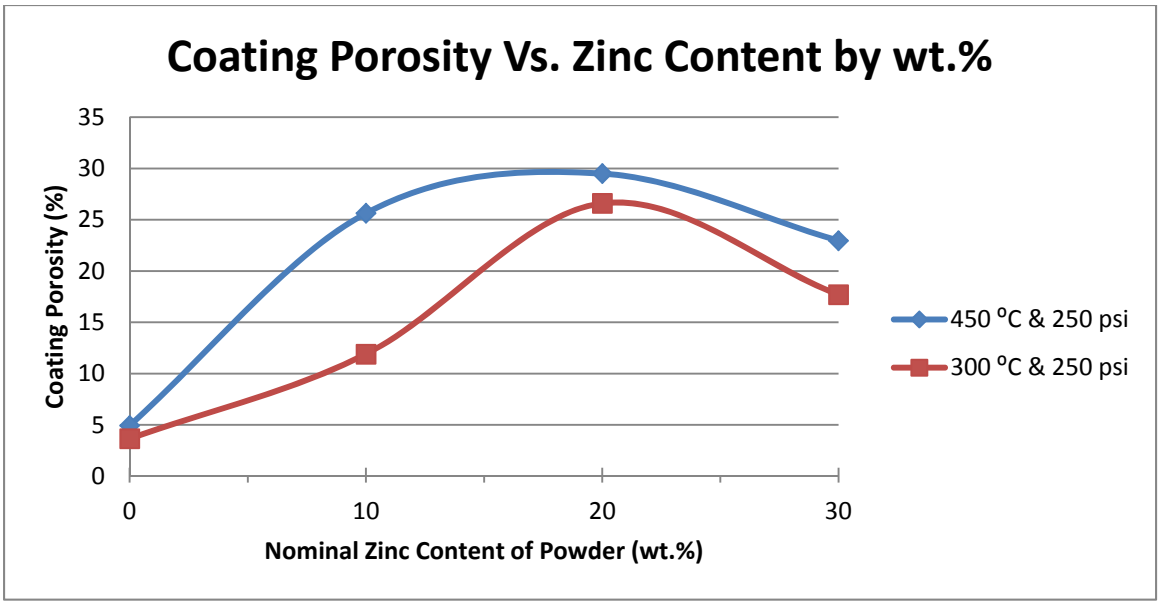

Figure 44. Coating Porosity Vs. Zinc Content by wt.%.

D. DISCUSSION

1. The Relationship between Deposition Efficiency and Changes in Pressure and Temperature

When considering the spray of pure copper or brass alloys, the relationships between deposition efficiency, coating thickness per pass, spray temperature and spray pressure are all consistent with the previously disseminated results obtained via the spray of Centerline SST's A-0050 powder mixture, as well as the general literature. Of special note, we see that temperature is slightly more of a "lever" than pressure is, providing a ratio of temperature increase to deposition efficiency increase of [1 : 1.36], while the similar ratio as defined with temperature increase provides a slightly smaller ratio of [1 : 1.31]. This is different from our pervious findings while conducting tests utilizing the A-0050 (aluminum-alumina) powder mixture, which found that pressure was the larger 'lever'. In either case, the difference between the two is likely within the statistical range for error in measurement—as such, our experiment concludes that each of the parameters, with all else held constant, is likely to be just as large of an impact on the output product as the other. However, because excess temperature may play a role in causing excessive residual stress as the deposit cools—degrading bond strength or causing full debonding of

the deposit from the substrate—the recommendation to prefer pressure increases over temperature increases if additional coating thickness or deposition efficiency is necessary, remains firm. Still further, upon reviewing the 3-D surface plots of deposition efficiency vs. spray pressure and spray temperature (Figures 33–36), that the change in deposition efficiencies in the feedstock powders all possess approximately the same slope, regardless of the operating parameter which was changed (pressure or temperature). This concurs strongly with the statistical evidence previously stated—that pressure and temperature in fact do act as similarly powerful 'levers' to increase deposition efficiency, and that the power of these parameters to change deposition efficiency is relatively constant regardless of the zinc content of the feedstock powder.

Microstructural cracking was observed at the deposit/substrate interface in all of the deposits sprayed at the higher temperatures of 450 °C. The left side of Figure 46 visually depicts this cracking in the Cu-90/10 wt.% Zn and Cu-80/20 wt.% Zn sample deposits, each sprayed at 250 psi [1.72 MPa]. This observation is in contrast to the deposit samples sprayed at 250 psi [1.72 MPa] and 300 °C, shown on the right side of Figure 45, which either did not exhibit such cracking at the deposit/substrate interface, or displayed such behavior at a greatly diminished qualitative magnitude. Because this microstructural cracking is temperature dependent, it is hypothesized that the interface cracking is occurring due to residual stress build-up upon deposit cooling—since aluminum has a very high thermal conductivity and a different thermal expansion coefficient than copper or brass, it is possible that the deposits are put under significant tensile stress while they cool back to room temperature. If this hypothesis is true, then the use of similar material substrates would diminish the magnitude of this problem, if not eliminate it completely. The following equation can be utilized to estimate the thermal residual mismatch, where σ_P^A is the residual stress of the coating material, $\Delta\alpha \bullet \Delta T$ is the thermal mismatch strain between the two materials, E^A is the modulus of elasticity of the coating material, E^B is the modulus of elasticity of the substrate material, ν^A is the Poisson's ratio of the coating material and t^A is the thickness of the deposit material [46]. In the case of Cu 90/10 wt.% Zn sprayed on 6061 Aluminum at 450 °C, this thermal mismatch residual stress is estimated to be 177.45 MPa.

$$(6) \Rightarrow \sigma_P^A = \frac{\Delta\alpha \bullet \Delta T \bullet E^A}{1-\nu^A}\left[1+\left(\frac{t^A}{t^B}\right)\left(\frac{\frac{E^A}{1-\nu^A}}{\frac{E^B}{1-\nu^B}}\right)\right]^{-1}$$

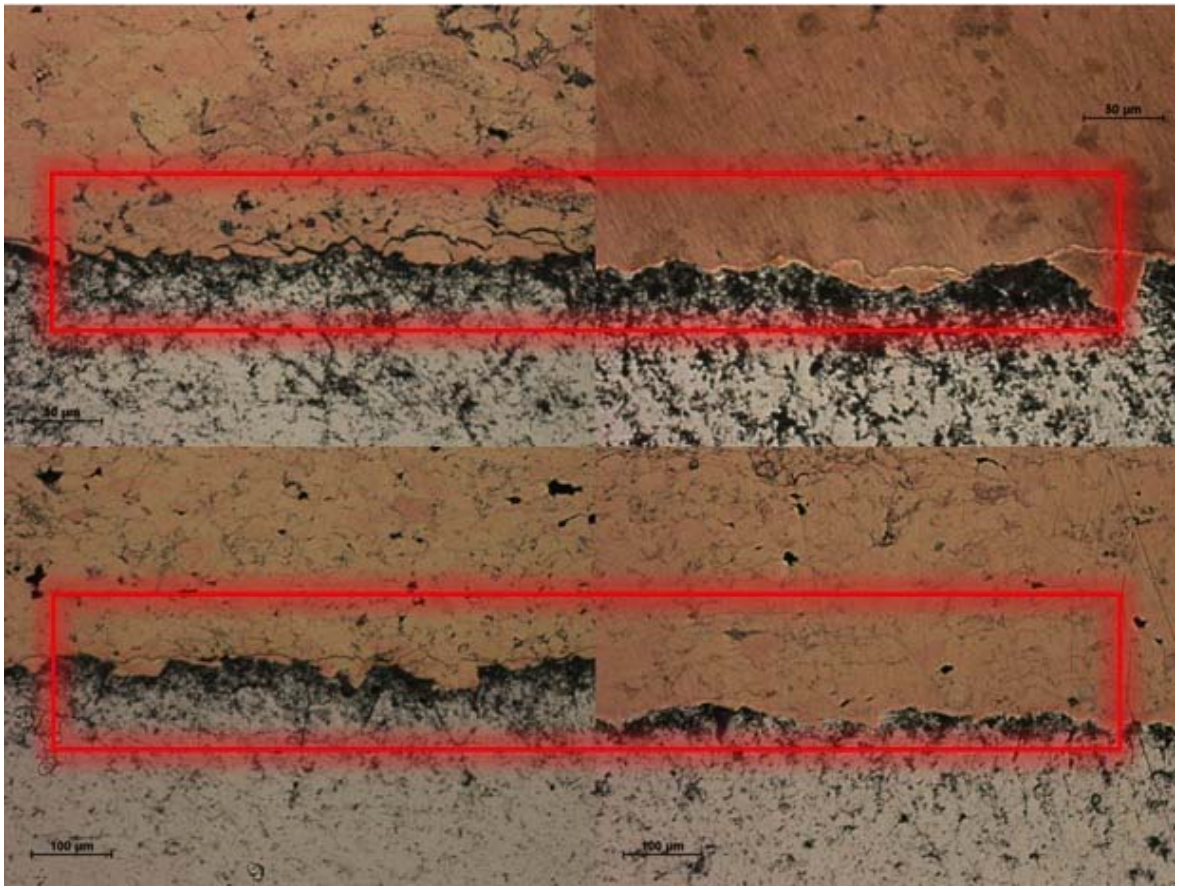

Figure 45. Optical Photographs of Deposit/Substrate Interface, Showing Cracking at Higher Spray Temperatures, (100x). Top Left: Cu-90/10 wt.% Zn (250 psi, 450 °C). Top Right: Cu-90/10 wt.% Zn (250 psi, 300 °C). Bottom Left: Cu-80/20 wt.% Zn (250 psi, 450 °C). Bottom Right: Cu-80/20 wt.% Zn (250 psi, 300 °C).

There is severe cracking at the deposit/deposit interface in the Cu-80/20 Zn which was sprayed at 250 psi [1.72 MPa] and the temperature of 300 °C and in both of the Cu-70/30 wt.% Zn deposits which were sprayed at 250 psi [1.72 MPa]—the cause of this cracking is unknown, but is hypothesized to be a combination of brittle fracture and

residual stresses. The deposit/deposit interface is defined as the plane where the second spray iteration was conducted on top of the other. All deposits were made using two, identical, sequential passes. For Cu-80/20 wt.% Zn and Cu-70/30 wt.% Zn deposits, almost complete separation of the two deposit layers occurs in a number of sections in the deposit coating, both of which are visible in Figure 46. Since this occurs in the Cu-80/20 wt.% Zn deposit sprayed at 300 °C and not in the sample sprayed at 450 °C (both utilizing a 250 psi spray pressure), then residual stresses cannot be the only culprit. Rather, it is hypothesized that the phenomenon is exhibiting itself because the powder and/or the coating is so hard that the powder particles are simply bouncing off the substrate and not depositing in large amounts, leaving behind large internal gaps or pores. This hypothesis is supported by the deposition efficiency results, which are very low for these materials—implying a significant amount of the powder is bouncing off the deposit instead of bonding. The observation of extensive brittle-type microstructural cracking in the vicinity of these large gaps that exist at the deposit/deposit interface further support this hypothesis. Lastly, the measured hardness of the Cu-80/20 wt.% Zn and the Cu-70/30 wt.% Zn deposits were approximately 16.7% and 20.4% greater, respectively, than the baseline pure copper deposit sprayed at the same pressure and temperature. Harder materials require much greater particle velocities to obtain the sufficient plastic deformation required to produce a coating. In agreement with our original hypothesis outlined in Chapter I, if the brass particles are indeed inhibiting dislocation motion and thus plastic deformation because of the very low stacking fault energy of brass, then it would be reasonable to assume that they require higher particle velocities to create deposits, and what deposit is created should be much harder than in standard copper.

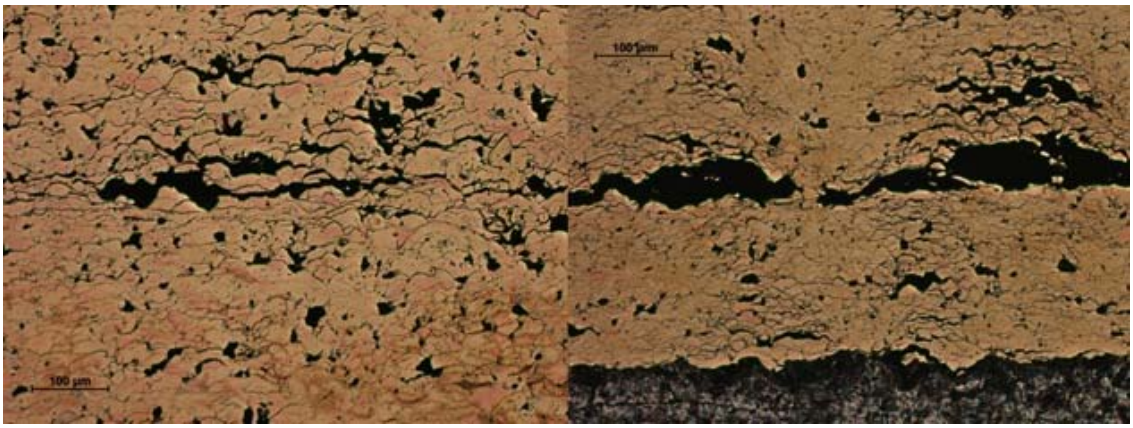

Figure 46. Brittle-Type Microstructural Cracking in the Vicinity of Deposit/Deposit Interface Gaps, (100x). Left: Cu-80/20 wt.% Zn Sprayed at 250 psi [1.72 MPa] and 300 °C. Right: Cu-70/30 wt.% Zn Sprayed at 250 psi [1.72 MPa] and 450 °C.

2. The Effect on Zinc Content on Deposition Efficiency and Coating Thickness

The zinc content has a large effect on the deposition efficiency of the spray medium, in addition to the coating thickness obtained per passing. As a matter of fact, modifying the zinc content simply from 0–10 wt.% had almost as strong of an effect on these two quantities as compared to raising the gas pressure by 43%, or the gas temperature by 50%. Increasing the zinc content of the material greater than 10 wt.% however decreases the deposition efficiency to levels equal to those seen in the pure copper powder in the case of the higher temperature spray (450 °C), and further degraded in the case of the low temperature control (300 °C). It was hypothesized originally in Chapter I that by raising the zinc content of the feedstock powder that the associated decreases in stacking fault energy (SFE), and thus increases in strain hardening coefficients, would dominate the process despite the fact that the melting point of the material was also lowering—allowing the material to be more malleable upon ballistic impact. It is well known that harder materials are more difficult to spray, and have degraded deposition efficiencies in comparison to softer materials [47]. Because significant dislocation motion is occurring during the spray, ballistic impingement and splat formation processes—due to the extreme forces being exerted on the individual particles—it would make sense that a material with a significantly higher strain hardening

coefficient would undergo a large amount of strain hardening. This would limit the movement of dislocations in the impingement and splat formation processes and ultimately lead to lowered deposition efficiencies by route of particle hardening. Our data suggests that this relationship is partially true. At zinc contents above 10 wt.%, the evidence would seem to suggest that the hypothesis is indeed correct, due to the dramatic erosion of deposition efficiency as zinc content increases above that level. However, the relationship does not hold true in the range between 0 and 10 wt.% of total zinc within the alloy. Thus, the evidence would seem to suggest that at zinc levels lower than approximately 10 wt.% in a Cu-Zn alloy, the increase in malleability due to the lowering of the alloy melting point does indeed dominate the process despite the decrease in stacking fault energy and associated increase in the strain hardening coefficient. At zinc contents above this level however, the evidence would suggest that the reverse is true, and that strain hardening via plastic deformation tends to dominate the spray characteristics of the process. This is evidenced quantitatively by noting that the decrease in melting point from 0–10 wt.% Zn is approximately 5%, while the decrease in stacking fault energy is approximately 20%. However, from 10–20 wt.% Zn the decrease in melting point remains approximately 5% while the decrease in stacking fault energy is a much greater 66%.

Even further, this relationship overshadows other spray parameters as well—a notion most clearly observed when considering the deposition of Cu-70/30 wt.% Zn. The mean particle size of the Cu-70/30 wt.% Zn powder was 11.24 µm vs. 26.35 µm for the Cu-80/20 wt.% Zn powder. As such, all else being same, the Cu-70/30 wt.% Zn should have been far easier to spray, and should have exhibited much higher deposition efficiencies than the Cu-80/20 wt.% Zn. This cause-effect relationship was investigated and proven by Jodoin et al. in 2006, who found that particles velocities increased by approximately 15% when mean particle size was reduced by approximately 20% [48]. Because the only thing that changed between the two spray conditions was the zinc content of the powder and the mean particle size, it can be readily inferred that the effects of decreasing stacking fault energy, and thus increasing the strain hardening coefficient in the Cu-70/30 wt.% Zn case not only negated any benefit that should have been

recognized by the decrease in mean particle size, but still yet was so influential that deposition efficiency and coating thickness per pass decreased by a further 36.5% from the Cu-80/20 wt.% Zn case (250 psi and 450 °C).

3. The Relationships between Powder Zinc Content and Deposit Hardness and Modulus

If stacking fault energy is indeed dominating the spray process as outlined previously, then deposit hardness should increase with increasing zinc content of the feedstock powder, the observation of which would tend to confirm the hypothesis outlined in Chapter I. In addition, the deposits should be harder regardless of the role of stacking fault energy, due to solid solution strengthening—the most well-known effect of adding zinc in solution with copper. That is precisely what is observed (Table 14 and Figure 37). With respect to the 250 psi [1.72 MPa] and 450 °C spraying condition, as the nominal zinc content of the feed powder rises from 0–10 wt.%, 10–20 wt.% and 20–30 wt.% Zn, average hardness increases by 9.45%, 6.64% and 3.12%, respectively, with a total surge in deposit hardness of 20.36% from 0–30 wt.% Zn. More or less the same relationship is observed in the 250 psi [1.72 MPa] and 300 °C as well—however notably the trend line observed in Figure 44 loses much of its definition from 10 -30 wt.% Zn. In the 250 psi [1.72 MPa] and 300 °C case, the percentage of total indents which were errant in the 20 wt.% Zn case was 58%, and in the 30 wt.% case, 88%.

Conversely, a steady attenuation in the magnitude of the modulus of elasticity of the material is observed when increasing the nominal zinc content of the feedstock powder. With respect to the 250 psi [1.72 MPa] and 450 °C spraying condition, as the nominal zinc content of the feed powder rises from 0–10 wt.%, 10–20 wt.% and 20–30 wt.% Zn, average Young’s modulus reduces by 1.01%, 8.21% and 11.63%, respectively, with a total reduction in deposit modulus of 19.54% from 0–30 wt.% Zn. The same variability of the trend line is seen in the 20 wt.% Zn and 30 wt.% Zn samples created under the 250 psi and 300 °C spraying conditions.

The increase in hardness conforms to the mechanisms outlined in the hypothesis—if stacking fault energy decreases, leading to a surge in strain hardening as

the splat deforms and bonds during deposition, then general hardness of the deposit should increase with an enlargement of the nominal zinc content of the alloy. Furthermore, although changes in modulus are often concurrent with changes in hardness, it is not unexpected to see the modulus of elasticity reduced as the nominal zinc content of the alloy increases. The ASM Handbook notes that the modulus of pure copper is 115 GPa, while the modulus of Cu-70/30 wt.% Zn is 110 GPa [49]. What is important to mention however is that the observed moduli of the deposits are all appreciably greater than the moduli of their unaltered counterparts, by approximately 10%. Also, the hardness values of the deposits are all substantially greater than those of the standard bulk material.

4. The Relationship between Powder Zinc Content and Porosity

The manner by which porosity is quantified is very important to note when considering the observations on porosity, as the utilization of a different method can produce quantified porosity results that vary significantly from the peer-reviewed literature. As an example, when considering the pure copper powder used in the experiments, deposits were produced with limited porosity—4.94% and 3.65% in the 450 °C and 300 °C (both at 250 psi [1.72 MPa]) samples, respectively. However, Stoltenhoff et al. reported spraying copper deposits with "negligible porosity" in 2006, and Koivuluoto et al. in 2007 reported spraying copper deposits that "were found to be dense showing no signs of porosity or voids [16, 28]." However, it is critical to note that these studies undertaken by Stoltenhoff et al. and Koivuluoto et al. both used a scanning electron microscope to analyze the porosity of the deposits, while optical microscopy, in conjunction with the ImageJ software from the National Institutes of Health, was utilized to produce the porosity measurements previously stated. Optical microscopy, vice scanning electron microscopy, was chosen to evaluate deposit porosity because the inherent contrast provided by the optical microscopy method for reliably displays porosity on a polished surface when used in bright field mode. When done with a SEM, the porosity of the current samples was evaluated at 2.27% and 1.38%, which were decidedly lower and more in line with previous reports, although still quantifiable and noticeable.

The difference in these reported porosities is attributed to the utilization of much higher pressures—435.1 psi [3.0 MPa] and 406.1 psi [2.8 MPa] by Stoltenhoff et al. and Koivuluoto et al., respectively, as they otherwise used reasonably similar conditions when spraying copper powder. These pressures correspond to increases of 74% and 62% greater spraying pressures, respectively. It has been well noted in the literature that the use of higher pressure entraining gas or an entraining gas with a lower molecular weight, such as helium, leads to significantly higher particle velocities and thus more dense deposit characteristics.

The zinc content of the feedstock material had the large impact on the porosity of the output deposit. As seen in Table 10, the initial increase in zinc content from 0–10 wt.% leads to a notable increase in porosity from 4.94% to 25.63%, and 3.65% to 11.90% in the high and low temperature cases (450 °C and 300°C), respectively, representing 419% and 226% increases. The addition of further zinc from 10–20 wt.% increases the porosity further, but the rate of which is at a diminished magnitude, 25.63% to 29.50% and 11.90% to 26.60%, again for the high and low temperature cases, respectively. The rate of increase for each is this case was a much lower 15% and 123%, respectively—but by this point over a full quarter of the total area of each deposit was constructed entirely of voids. Finally, when zinc content is enlarged from 20–30 wt.%, the porosity actually decreases in magnitude, 29.50% to 22.96% and 26.60% to 17.69% for the high and low temperature cases, a 22% and 33% decrease, respectively.

The most likely source of the large scale porosity in the deposited brass coatings is the fact that the brass powder particles are large and strangely shaped. Although the brass powder particles appear on the surface to be detached, spheroid particles (Figure 24), closer inspection of the cross section images (Figure 26) shows that many particles are physically interconnected. This interconnected nature is particularly observed for the larger brass particles. The result is that instead of spraying individual particles of uniform size, we are spraying a larger distribution of particle sizes and shapes, many of which have a large central particle with semi-spherical “nodules” appended to it. When a particle with this shape impacts the substrate, it may adhere, but it will likely have large pores that are not fully collapsed by the impact. It should be noted that the particle size

of Cu-70/30 wt.% Zn was substantially smaller than the other brass compositions. It also had fewer inter-particle connections (Figure 26), and subsequently had much less porosity when sprayed (Figure 43).

The interconnected and complex particle shapes of the brass powders are mostly likely due to the current ACU process for making brass powders. In this process, the copper particles are formed using gas atomization, a common metal powder process that results in individual, spherical powder particles with a range of sizes. While, there is a strong correlation between the zinc content and the porosity in the cold spray deposits, but it is likely not causal. To create brass, the ACU process coats the particles with zinc and then anneals them to diffuse the zinc through the particles. It seems that during this process, many of the smaller particles fuse to the larger particles, thus creating the large, complex particles observed in Figure 26. We hypothesize that a light milling of these powders, to break the interconnections, or the use of brass powders formed directly through gas atomization would greatly reduce the observed porosity.

5. Compositional Variability as a Side Effect of the Cold Spray Deposition Process

The micro-scale variation in composition of the brass deposits was seemingly increased during or after cold spray deposition as observed by X-ray maps of the copper and zinc distributions (Figures 47–49). In addition, semi-quantitative X-ray analysis displayed a marked increase in the zinc content variation compared with the starting powders (Table 16). The SEM photographs of the deposit at the substrate/deposit interface (the large dark areas at the bottom of each photograph is the substrate in each case), as well as the composition maps are presented at 500x magnification. Immediately, one will notice from the zinc composition maps of the Cu-90/10 wt.% Zn and Cu-80/20 wt.% Zn deposits that the concentrations of zinc within the deposit are definitively non-uniform of a magnitude greater than that exhibited in the feedstock powder, qualitatively speaking. Quantitatively, we see that the standard deviation of zinc content jumped almost 100% in contrast to the as-received feedstock powder. From Table 16, in each case we observed that zinc in fact was present in far lower concentrations near pores than that seen in the feedstock powder, or in the general bulk deposit. Additionally we

observed that much higher concentrations of zinc were found in the general deposit than seen in the feedstock powder.

Powder Material	Cu-90/10 wt.% Zn	Cu-80/20 wt.% Zn
Overall		
Minimum wt.% of Zn	1.90	1.31
Maximum wt.% of Zn	22.37	38.10
Average wt.% of Zn	8.67	21.15
Standard Deviation	5.69	8.99
Bulk Deposit		
Average wt.% of Zn	11.88	26.50
Near Pores		
Average wt.% of Zn	5.72	15.73

Table 16. Multi-Point X-ray Data and Statistics for Cu-90/10 wt.% Zn and Cu-80/20 wt.% Zn deposits.

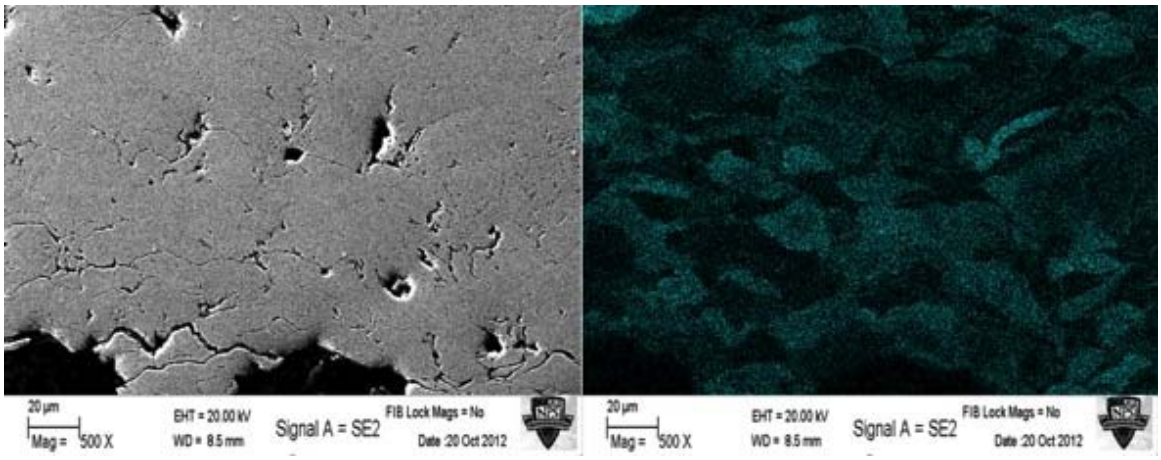

Figure 47. Cu-90/10 wt.% Zn Deposit Sprayed at 250 psi [1.72 MPa] and 450 °C. Left: SEM Photograph, 500x. Right: Zinc Composition Map, 500x.

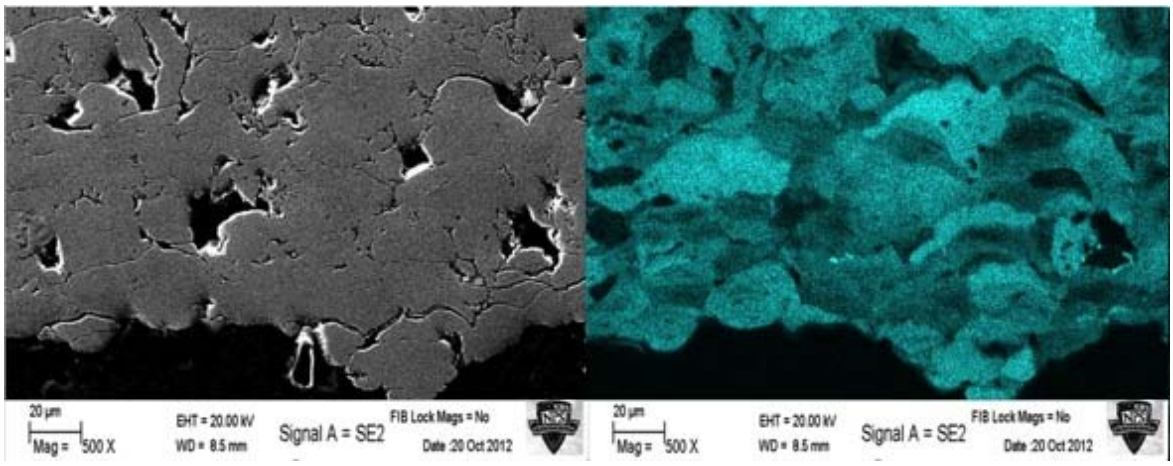

Figure 48. Cu-80/20 wt.% Zn Deposit Sprayed at 250 psi [1.72 MPa] and 450 °C. Left: SEM Photograph, 500x. Right: Zinc Composition Map, 500x.

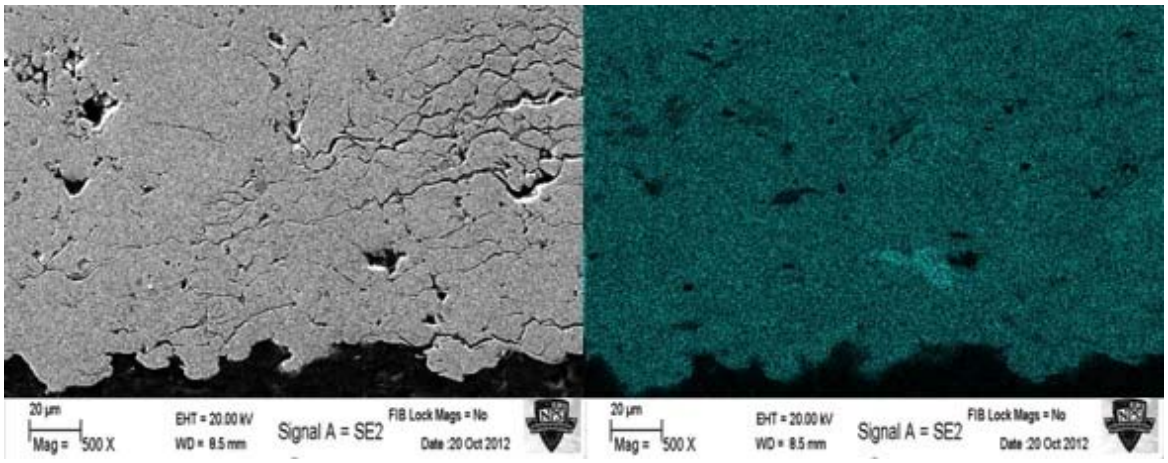

Figure 49. Cu-70/30 wt.% Zn Deposit Sprayed at 250 psi [1.72 MPa] and 450 °C. Left: SEM Photograph, 500x. Right: Zinc Composition Map, 500x.

The variation in zinc content is most likely due to zinc migration *after* cold spray deposition. There is not time during the deposition process itself (less than one millisecond) for diffusion-based zinc migration. There may be sufficient thermal energy and kinetics after deposition to hypothesize diffusion-based zinc transport. Zinc has an exceptionally high vapor pressure (14,000 mm-Hg at 350C [50]) and dezincification of brass is a well-known problem at temperature similar to those used during these cold spray experiments. Zinc could migrate to the surfaces of pores in the deposit and leave the deposited metal into the vapor phase. If the temperature of the deposit is able to

support a zinc diffusivity of 10^{-10} cm^2/s for 10 minutes (600 seconds) after deposition, then the zinc could migrate more than seven microns, enough to explain the observed change in micro-scale composition for the brass deposits. The large amount of strain during deposition will likely produce a high dislocation density which will enhance this effect. Deposition at lower temperatures and reduction in deposit porosity would reduce the migration of zinc in the deposited microstructure.

THIS PAGE INTENTIONALLY LEFT BLANK

IV. COLD SPRAY OF NANOCRYSTALLINE COPPER AND BRASS FEEDSTOCK POWDERS

A. FEEDSTOCK POWDER PREPARATION AND CHARACTERIZATION

Cryomilling was chosen as the appropriate method to prepare the nanocrystalline powder from the as-received powder largely because of the extensive previous research in the literature. In particular, Bahmanpour et al. produced results in 2011 by which pure copper, Cu-90/10 wt.% Zn, Cu-80/20 wt.% Zn and Cu-70/30 wt.% Zn were all cryomilled for a duration of twelve hours, and then microhardness and crystallite size were evaluated to determine at what total milling time one could conclude that each of the materials had reached the maximum hardness and minimum crystallite size pursuable by the cryomill method [40]. Graphs of the results can be found in Figures 50 and 51. Bahmanpour et al. determined via this research that crystallite size and microhardness became more or less constant in the range of four to six hours of cryomilling time, after which point minimal change was noted. The powders at that point were determined to have crystallite sizes of 20 nm or less, making them indeed nanocrystalline. Based on these results, powder was prepared using approximately 100 grams of both the pure copper and Cu-90/10 wt.% Zn powders, which was cryomilled for five hours to obtain assumed nanocrystalline powder, to be used in a cold spray deposition experiment. It was not verified by independent means that this powder was actually nanocrystalline, and as such the powder is will be referred to as “cryomilled” in this chapter.

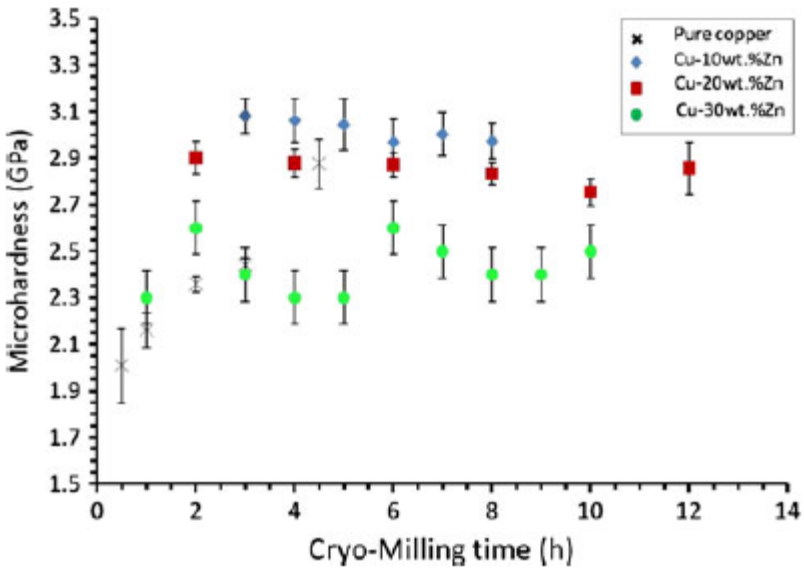

Figure 50. Microhardness vs. Cryomilling Time. From [40].

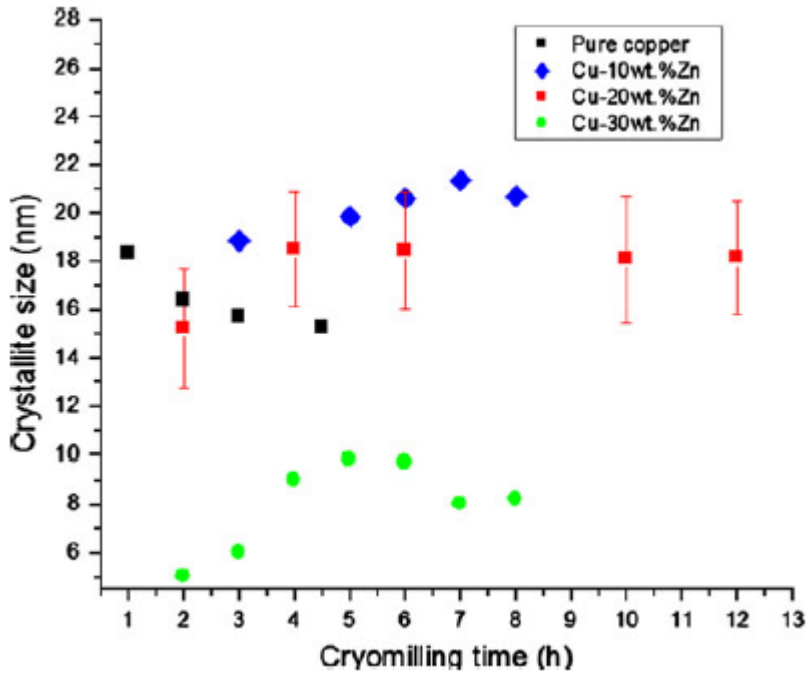

Figure 51. Crystallite Size Vs. Cryomilling Time. From [40].

The characterization of the as received powder prior to cryomilling can be found in Chapter III, Section A.

B. EXPERIMENTAL METHOD

A SPEX SamplePrep Freezer/Mill model series 6870 was utilized for the cryomilling process. 50 grams of the 620 Series copper powder was inserted into a SPEX SamplePrep series 6801 large grinding vial set—the vial itself is constructed of a polycarbonate shell with stainless steel end plugs with a stainless steel impactor contained within the vial. The vial loading process was accomplished in a glove box filled with argon gas at atmospheric pressure in order to prevent oxidation or corrosion contamination of the powder. The mill was then filled with liquid nitrogen to bring it to a temperature of 77 K, after which the mill was topped off at thirty minute intervals to ensure a consistent temperature of 77 K during the milling process.

Before starting the milling process, the vial and powder contained within was pre-cooled via submersion in the liquid nitrogen for a period of 15 minutes to confirm that the powder had reached the temperature of the mill (77 K). The 6870 Freezer/Mill was then operated at a rate of fifteen cycles per second for ten minutes, followed by a two minute cooling period during which the milling process was paused. This cycle was repeated until the total milling time reached five hours, after which the vial was removed from the mill and allowed to warm to ambient temperature. After ambient temperature was reached, the vial was placed again in the inert environment of the glove box and the powder was removed.

This process was done twice for both the pure copper and Cu-90/10 wt.% Zn powders, yielding a total of 100 g of usable powder of each type for cold spray deposition.

Cold spray deposition was carried out using the exact same spray pattern as discussed in Chapter III Section B. Only a single spray pressure and temperature combination was used, 250 psi [1.72 MPa] and 450 °C. The deposits were sprayed onto T-6061 aluminum substrates that had been subjected to the sandblasting procedure previously outlined.

Deposition efficiency was measured in the same manner as formerly noted, however coating thickness per pass was not possible to measure accurately with a digital

micrometer—due to the thin coatings produced. Thus, coating thickness per pass was estimated by visual inspection during optical microscopy.

The samples were cut, hot-mounted, sanded, polished, cleaned and desiccated as outlined beforehand in Chapter III Section B.

Optical microscopy was again performed on each of the samples by utilizing the Nikon POTIPHOT 200 light microscope in conjunction with a digital camera. Photographs were taken at the 100x and 200x magnification levels.

Hardness of the deposit samples was measured using the G200 nano-indenter manufactured by Agilent Technologies Inc. in conjunction with a Berkovich diamond tip. Fifteen sample points were chosen to average out the resulting hardness to prevent obfuscation of the resulting data by a statistical outlier. The parameters for the indents were as follows: 0.05 nm/s allowable drift rate, 3.0 hr maximum thermal drift time, 2000 nm surface approach distance, 200 nm/s surface approach velocity, 1000 nm indentation depth and 0.08 strain rate.

C. RESULTS

Both the copper and 90/10 cryomilled powders were successfully deposited using cold spray, albeit with low deposition efficiencies. The deposition efficiency for the cryomilled copper and Cu-90/10 wt.% Zn powders was 2.30% and 1.10% for each of the samples, respectively — notably minute. Coating thickness was unable to be measured with the micrometer used in the microcrystalline analysis—instead coating thickness was estimated via the use of the Zeiss Neon-40 scanning electron microscope. The cryomilled copper produced coatings thicknesses per pass of approximately 55 µm while the cryomilled Cu-90/10 wt.% Zn thickness per pass was measured to be approximately 35 µm. It should be stated that the coatings were highly irregular with respect to coating thickness from one part of the substrate to another. In some places the deposit was half of the thickness stated, and in some other positions it was twice as thick—the stated results was observed to be approximately the average over the area of viewing.

SEM photos of the cross section of each sample can be found in Figures 52 and 53 in 250x and 500x magnifications. In both figures the cryomilled copper deposit is on the left hand side, and the cryomilled brass the right hand side.

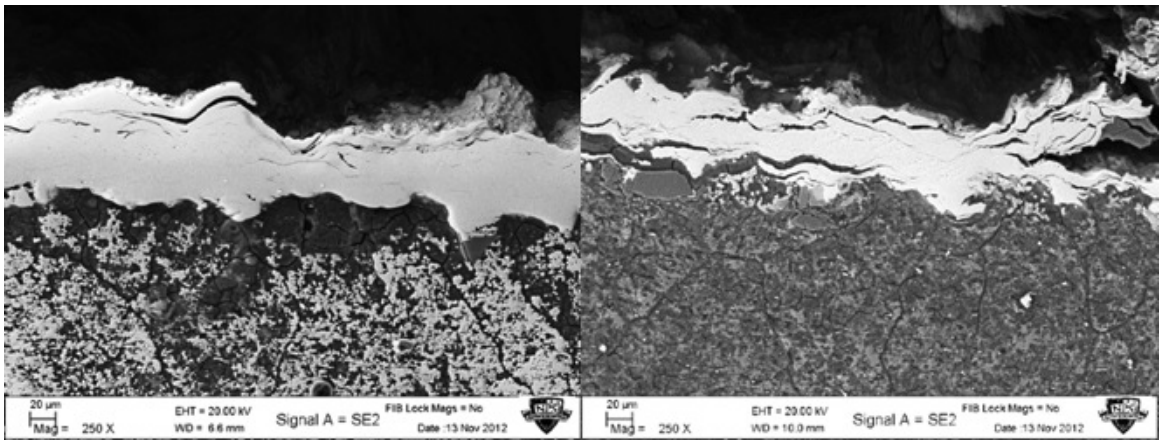

Figure 52. SEM Photographs of Cryomilled Deposits Sprayed at 250 psi [1.72 MPa] and 450 °C, 250x Magnification Left: Pure Copper. Right: Cu-90/10 wt.% Zn.

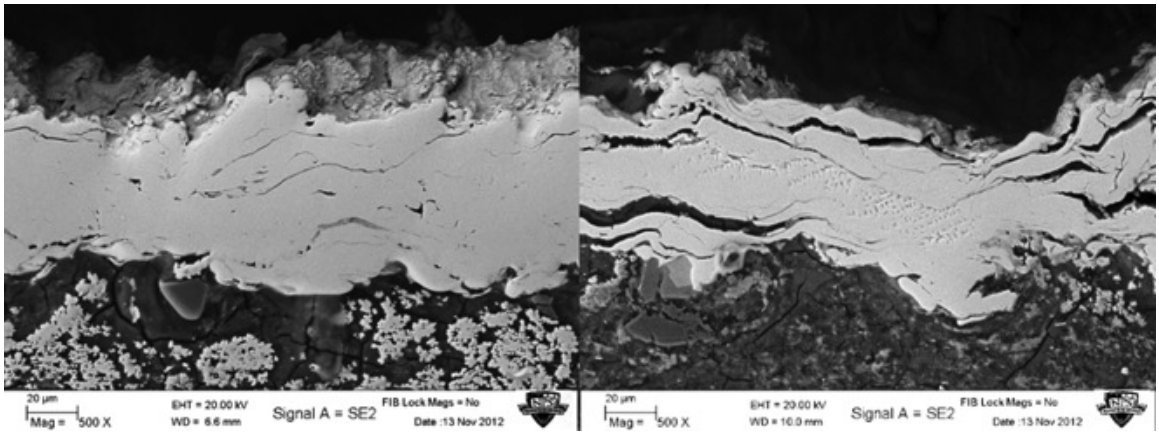

Figure 53. SEM Photographs of Cryomilled Deposits Sprayed at 250 psi [1.72 MPa] and 450 °C, 500x Magnification. Left: Pure Copper. Right: Cu-90/10 wt.% Zn.

Average hardness was measured to be 3.80 GPa in the cryomilled copper sample, and 3.31 GPa in the cryomilled brass sample. The standard deviations were 0.89 GPa and 0.29 GPa for each sample, respectively; however, only three measurements were possible to be obtained for each sample. Additionally the modulus of elasticity was measured to be 134.6 GPa and 100.8 GPa for each sample, respectively. In both cases, a limited

number of measurements could be obtained owing to compliance issues from the porosity in the coatings, which can be observed below in the graphs of hardness and modulus for both the cryomilled copper deposit as well as the cryomilled Cu-90/10 wt.% Zn deposit (Figures 54 and 55, respectively). The hardness and modulus values reported are averaged from depths between 150–250nm below the polished, cross-sectional surface.

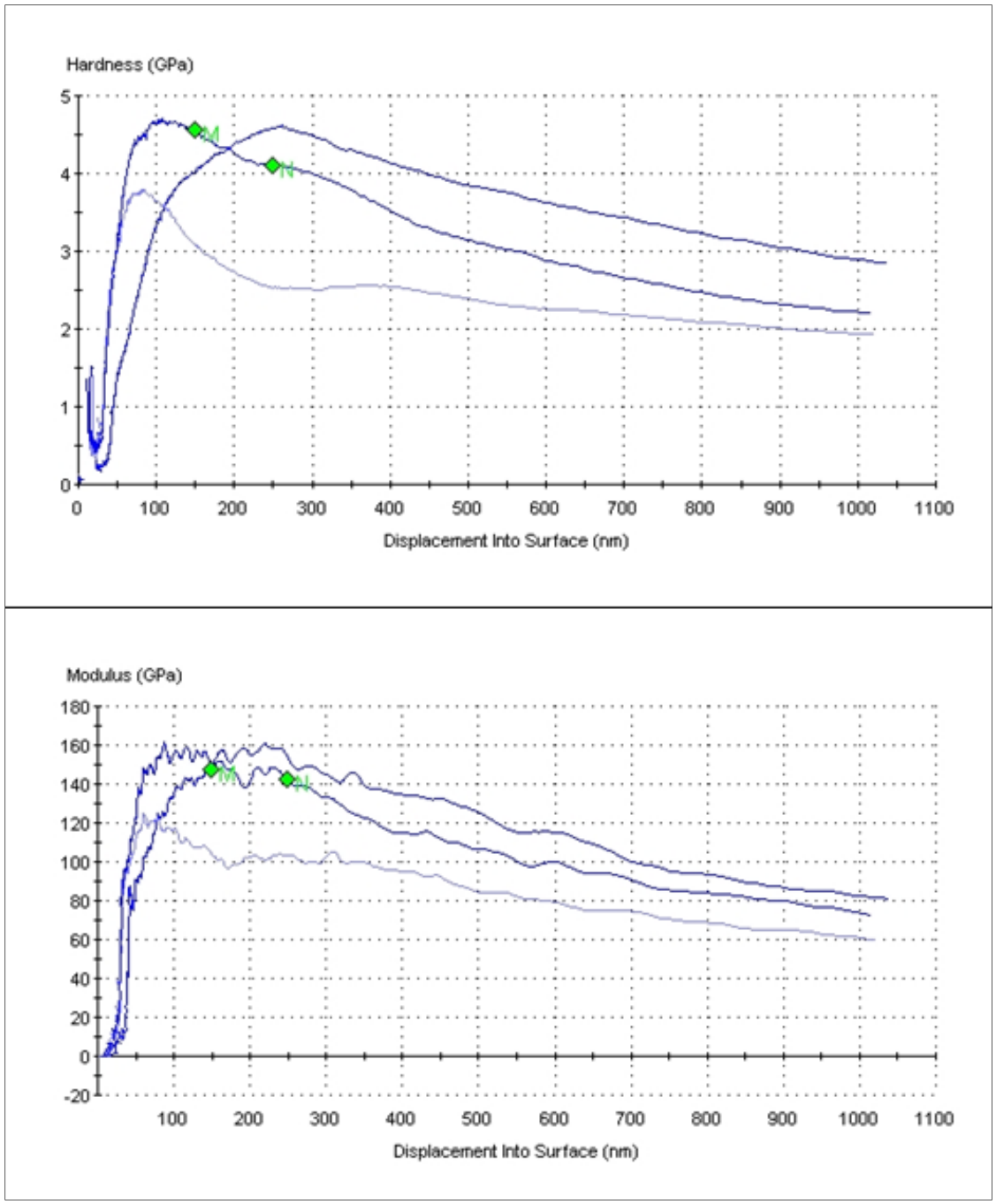

Figure 54. Nano-indentation Results for Cryomilled Copper Powder Deposit. Top: Hardness. Bottom: Modulus of Elasticity.

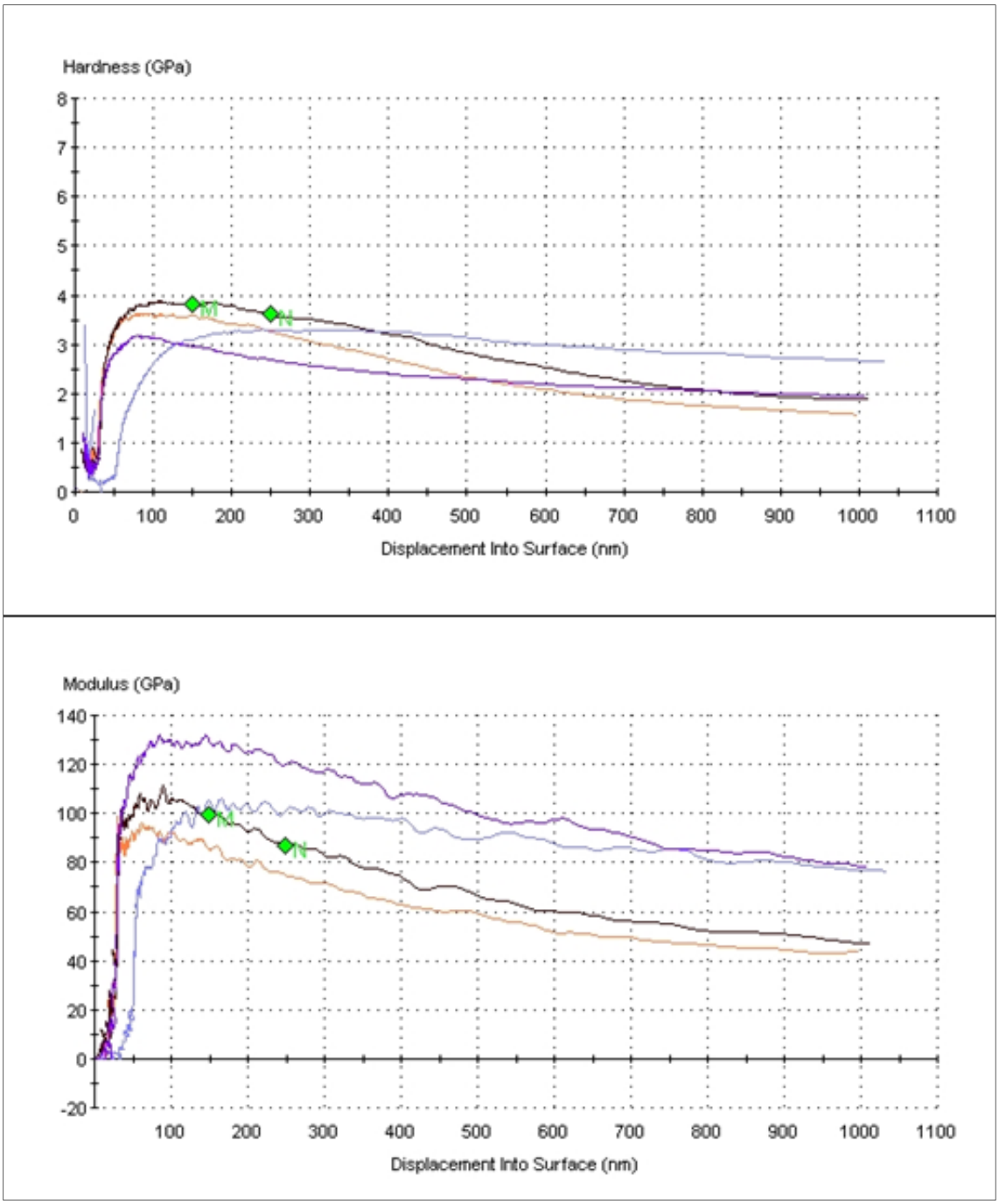

Figure 55. Nano-indentation Results for Cryomilled Cu-90/10 wt.% Zn Powder Deposit. Top: Hardness. Bottom: Modulus of Elasticity.

D. DISCUSSION

Ultimately, the most important result is strictly qualitative—it is in fact possible to utilize the cold spray deposition method to create coatings of nanocrystalline copper based alloys. Still yet, with such small deposition efficiencies, it should be noted that the use of helium as the entraining medium will likely be required to produce coatings of any appreciable thickness.

The results obtained with respect to coating thickness agree with those of Liu et al. who conducted experiments in 2012 with the deposition of cryomilled copper powder, although further information such as deposition efficiency and the utilized spray pattern would be required to confirm agreement with their work [51]. Liu et al. produced nanocrystalline copper coatings on polished T-6061 aluminum substrates from cryomilled powder via utilization of cold spray with a spray temperature of 300 °C, 2.0MPa [290 psi] of spray pressure, nitrogen as the entraining gas, a stand-off distance of 10 mm and a gun velocity of 5 mm/s—their coatings were reported as being dense, like the current results, but with a thickness of approximately 100–150 µm. At first sight, our results would tend to indicate a much lower deposition efficiency than that seen by Liu et al. given that we observed coatings of approximately 50 µm in thickness, after two complete spray passes, in contrast to Liu et al.'s single pass. However, Liu et al. utilized a 16% higher spray pressure, a closer stand-off distance and most importantly, a gun velocity of only 12.5% of ours—allowing for significantly more time for the deposit to build up as the gun sprayed onto the substrate. Still yet, Liu et al. did use a 33% lower spraying temperature and did not sandblast their T-6061 aluminum substrates prior to spray, both of which would tend to degrade performance, and the mean particle size of their powder is unknown. The cross sectional photographs of the deposits created by Liu et al. however look similar to ours in microstructure, which provides circumstantial evidence that we would obtain the same results provided we followed the same spraying procedures.

In contrast with the microcrystalline deposits, there is not a significantly large gap in the deposition efficiencies as additional amounts of zinc are alloyed with the copper in the cryomilled case. While this apparent difference in deposition behavior seems to

conflict the results report in Chapter III, it should be noted that the deposition efficiencies of both cryomilled powders are so small that it is somewhat difficult to measure precisely how much powder actually was deposited, or how thick the coating was in aggregate. It is suggested that deposition efficiency and coating thickness per pass be re-tested with the use of helium as the entraining gas, or with a much slower gun-raster velocity. The hypothesis stands that the trends identified previously between zinc content and stacking fault energy will hold true for cryomilled powders as well as the as-received.

Hardness was measured to be quite high in both the cryomilled copper and cryomilled Cu-90/10 wt.% Zn samples. Interestingly enough, the cryomilled copper deposit was a full 14.8% greater in magnitude than the cryomilled brass deposit. This finding directly contradicts the results found in the microcrystalline analysis, but does resemble the previously microhardness results of Bahmanpour et al. in. 2011, who observed decreasing microhardness in brass alloys that had been cryomilled as further zinc was added to the alloy from 0–30 wt.% [40]. It is still possible, given the small data sampling size, that the data presented is somewhat inaccurate—further hardness testing would be required to repudiate such an idea. The small sample size was due to difficulty in obtaining useful nanoindentation data, a product of poor material compliance while taking hardness measurements. In each of the hardness measurements, illustrated in Figures 54 and 55, the curve should be more or less flat as a function of depth. However, each measurement exhibits a downward slope after reaching a global maximum. This slope indicates that the material has a reasonably large compliance, which could be the function of internal cracking, brittle behavior or both. It is possible that this behavior could be avoided with thicker samples, which may be less prone to such behavior. Also important to note is that the hardness of each of the deposits were much greater in magnitude than the microcrystalline deposits—to be expected. In fact, the hardness of the nanocrystalline copper deposit was 38.1% greater than the microcrystalline deposit, and the nanocrystalline Cu-90/10 wt.% Zn was found to be 10% greater than its microcrystalline counterpart—despite the fact that both were sprayed in otherwise the exact same conditions. Interestingly enough, the measured hardness result obtained in the deposit made of cryomilled copper, 3.80 GPa, was much higher than that observed by Liu

et al. during their research, 3.02 GPa [51]. This hardness could have been caused by differing cryomilling parameters. Such excessive hardness exhibited in our cryomilled copper deposit may indeed explain some of the earlier stated discrepancy between Liu et al.'s and our own coating thickness observation—as harder powders are more difficult to deposit and harder surfaces more difficult to deposit on (after the initial copper/aluminum interface is made, the remaining splats must deposit on the existing copper layer).

Unlike in the microcrystalline deposits, there was no noticeable porosity within either of the cryomilled deposits. This may be due to the relatively small thickness of the coating—obscuring what would be present in a thicker coating. However, it is hypothesized that the cryomilled powders are so hard that they cause plastic deformation of the deposit as they strike the already bonded coating and in doing so are filling the voids in a peening type of phenomenon. Liu et al. found a large number of deformation bands in their nanocrystalline copper deposits, and attributed such behavior to the same peening process [51].

Further evidence for our original hypothesis with respect to stacking fault energy can be found in the observation of the coating microstructure however. From Figures 52 and 53, it is quite clear that while the cryomilled copper coating is relatively dense and largely intact, the cryomilled brass coating contains numerous large cracks throughout its microstructure—this cracking would tend to be evidence of a harder, more brittle material. This result would align with our previous statements with respect to zinc content, stacking fault energy and the associated strain hardening upon deposition of the material. However, we also must note that the hardness of the cryomilled brass deposit was found to be significantly less than the cryomilled copper deposit (12.9% less). As such, we would normally expect the cracking to at least show itself in the cryomilled copper deposit, if not be more severe in nature given the higher hardness and modulus of elasticity.

In order to more precisely answer these questions, it is suggested that X-ray diffraction and back-scatter diffraction be performed on the coatings after spraying thicker deposits with helium. Instead of using helium, slower gun travel speeds could be utilized in conjunction with nitrogen to build up a coating of sufficient thickness. This

will provide more information as to the exact crystallite size encountered in the deposits and hopefully provide the ability to better delineate the physical hardness of the material with a better confidence interval.

V. CONCLUSION

A. SUCCESSFUL INSTALLATION OF COLD SPRAY DEPOSITION SYSTEM AT NPS

In the course of this thesis, successful installation of Naval Postgraduate School's first ever cold gas-dynamic spray system was completed. The equipment was modified slightly to enable safe and reliable operation and was then calibrated for the use of a number of different powder materials, such as aluminum, copper and brass. Initial relationships between the thermodynamics and fluid mechanics of the spraying action and the resultant deposits were made using an aluminum/alumina powder mixture, providing a wealth of knowledge by which further experiments can be designed intelligently. The results of this testing were compared with similar literature and found to be in general agreement.

B. SUCCESSFUL DEPOSITION OF BRASS

Brass alloys were successfully cold spray deposited from a number of differing compositions of brass feedstock powder, including Cu-90/10 wt.% Zn, Cu-80/20 wt.% Zn and Cu-70/30 wt.% Zn. This is the first report for brass alloys using the cold gas-dynamic spray system.

Deposition efficiency initially increases by as much as 67% as zinc content increases from 0–10wt.%, but then decreases just as rapidly as zinc content continues to rise. The initial increase in deposition efficiency is attributed to the lowering of the melting point by approximately 5%, but the rapid decrease is attributed to the decrease in stacking fault energy and associated increase in the strain hardening coefficient. This mechanism suggests that materials with high strain hardening coefficients in general will produce thinner coatings for the same amount of powder, and in extremely high cases may prove unsuitable for use in the process.

Hardness was observed to increase with increasing zinc content. Hardness in the Cu-70/30 wt.% Zn deposit was measured to be 3.31 GPa, which is far greater than found in the bulk powder or in copper deposits. The relationship between hardness and zinc

content confirms the strong role played by the stacking fault energy of the material in producing the deposit characteristics.

The microstructure of the cold spray deposited brasses was quite complex. Importantly, the porosity observed in all of the brass deposits is far greater than that which was observed in copper deposits sprayed at the same conditions. In the case of Cu-90/10 wt.% Zn the observed porosity was over 400% greater in magnitude, with voids making up no less than 25% of the total cross sectional area. There was a strong correlation with higher spraying temperatures and higher porosity. It is hypothesized that this occurs due to zinc leaching out of solid solution, possibly in the vapor phase. In addition, composition was found to vary widely in the brass deposits, far greater than seen in the feedstock powder itself, which supports the idea of zinc migration.

C. DEMONSTRATION OF COLD SPRAY OF CRYOMILLED COPPER AND BRASS

Nanocrystalline deposits which were dense with no appreciable porosity were successfully created from cryomilled copper and Cu-90/10 wt.% Zn powders. The deposition efficiency of these powders is much smaller than their in their standard, microcrystalline forms, and the hardness of the cryomilled copper deposit approaches 4.0 GPa, 40% harder than its standard counterpart. While the nanocrystalline structure of the deposited material was not directly observed, this initial result is consistent with the successful deposition of nanocrystalline material, the first report of such a result for a copper alloy.

LIST OF REFERENCES

[1] B. S. DeForce, T. J. Eden and J. K. Potter, "Cold spray Al-5% Mg coatings for the corrosion protection of magnesium alloys," *Journal of Thermal Spray Technology*, vol. 20, no. 6, pp. 1352–1358, Dec. 2011.

[2] P. F. Leyman and V. K. Champagne, "*Cold spray process development for the reclamation of Apache Helicopter Mast Support*," Army Research Laboratory, Aberdeen, MD, Rep. ARL-TR-4922, Aug. 2009.

[3] J. Villafuerte and D. Wright, "Practical cold spray success: Repair of Al and Ag alloy aircraft components," *Advanced Materials & Processes*, vol. 168, no. 5, pp. 53–55, May 2010.

[4] V. K. Champagne, *The cold spray materials deposition process: Fundamentals and applications*, Cambridge, UK: Woodhead Publishing, 2007, p. 1.

[5] V. K. Champagne, *The cold spray materials deposition process: Fundamentals and applications*, Cambridge, UK: Woodhead Publishing, 2007, p. 2.

[6] R. C. McCune et al., "Characterization of copper layers produced by cold gas-dynamic spraying," *Journal of Thermal Spray Technology*, vol. 9, no. 1, pp. 73–82, Jan. 2000.

[7] A. Papyrin, "Cold Spray Technology," *Advanced Materials & Processes*, vol. 160, no. 3, pp. 49–51, 2001.

[8] T. H. Van Steenkiste et al., "Kinetic Spray Coatings," *Surface and Coatings Technology*, vol. 111, pp. 62–71, 1999.

[9] T. Stoltenhoff , H. Kreye and H. Richter, "An analysis of the cold spray process and its coatings," *Journal of Thermal Spray Technology*, vol. 11, no. 4, pp. 542–550, 2002.

[10] R. Dykhuisen and M. Smith, "Gas dynamic principles of cold spray," *Journal of Spray Technology*, vol. 7, no. 2, pp. 205–212, 1998.

[11] V. F. Kosarev et al., "On some aspects of gas dynamics of the cold spray process," *Journal of Thermal Spray Technology*, vol. 12, no. 2, pp. 265–281, 2003.

[12] M. Grujicic et al., "analysis of the impact velocity of powder particles in the cold-gas dynamic-spray process," *Materials Science and Engineering A*, vol. 368, pp. 222–230, 2004.

[13] R. Dykhuisen et al., "Impact of high velocity cold spray particles," *Journal of Thermal Spray Technology*, vol. 8, no. 4, pp. 559–564, 1999.

[14] M. Grujicic et al., “Computational analysis of the interfacial bonding between feed-powder particles and the substrate in the cold-gas dynamic-spray process,” *Applied Surface Science*, vol. 219, pp. 211–227, 2003.

[15] J. Vlcek et al., “A systematic approach to material eligibility for the cold-spray process,” *Journal of Thermal Spray Technology*, vol. 14, no. 1, pp. 125–133, 2005.

[16] C. Stoltenhoff et al., “Microstructures and key properties of cold-sprayed and thermally sprayed copper coatings,” *Surface and Coatings Technology*, vol. 200, pp. 4947–4960, 2006.

[17] C. J. Li and W. Y. Li, “Deposition characteristics of titanium coatings in cold spraying,” *Surf. Coat. Technol.*, vol. 167, no. 2–3, pp. 278–283, 2003.

[18] A. P. Alkhimov et al., “Gas dynamic spraying study of a plane supersonic two-phase jet,” *J. Appl. Mech. Tech. Phys.*, vol. 38, no. 2, pp. 324–330, 1997.

[19] R. C. Dykhuisen and R. A. Neiser, “Optimizing the cold spray process” in *Thermal Spray 2003: Advancing the Science and Applying the Technology*, B. R. Marple and C. Moreau, Ed., Orlando, FL, 2003.

[20] A. N. Papyrin et al., “On the interaction of high speed particles with a substrate under cold spraying,” in *International Thermal Spray Conference*, E. Lugschieder and C. C. Berndt, Ed., Essen, Germany, 2002.

[21] P. Alkimov, V. F. Kosarev and A. N. Papyrin, “A method of cold gas-dynamic deposition,” *Sov. Phys. Dokl.*, 1990, vol. 35, no. 12, pp. 1047–1049, trans. American Institute of Physics, 1991.

[22] A. P. Alkimov et al., “Gas Dynamic Spraying Method for Applying a Coating,” U.S. Patent 5 302 414, Apr., 12, 1994.

[23] A. O. Tokarev, “Structure of aluminum powder coatings prepared by cold gas-dynamic spraying,” *Met. Sci. Heat Treat.*, vol. 38, no. 3–4, pp. 136–139, 1996.

[24] D. L. Gilmore et al., “Particle velocity and deposition efficiency in the cold spray process,” *Journal of Thermal Spray Technology*, vol. 8, no. 4, pp. 576–582, May 1999.

[25] J. H. Wu et al., “Critical and maximum velocities in kinetic spraying” in *Proceedings of the 2006 International Thermal Spray Conference*, Seattle, WA, 2006.

[26] V. K. Champagne, *The cold spray materials deposition process: Fundamentals and applications*, Cambridge, UK: Woodhead Publishing, 2007, p. 1.

[27] X. J. Ning, J. H. Jang and H. J. Kim, “The effects of powder properties on in-flight particle velocity and deposition process during low pressure cold spray process,” *Applied Surface Science*, vol. 253, pp. 7449–7445, Mar. 2007.

[28] H. Koivuluoto, J. Lagerbom and P. Vuoristo, “Microstructural studies of cold sprayed copper, nickel and nickel-30% copper coatings,” *Journal of Thermal Spray Technology*, vol. 16, no. 4, pp. 488–497, Apr. 2007.

[29] C. Borchers et al., “Microstructural bonding features of cold sprayed face centered cubic metals,” *Journal of Applied Physics*, vol. 96, no. 8, pp. 4288–4292, 2004.

[30] C. Borchers et al., “Formation of persistent dislocation loops by ultra-high strain-rate deformation during cold spraying,” *Acta Materialia*, vol. 53, pp. 2991–3000, 2005.

[31] M. Kowalski and P. J. Spencer, “Thermodynamic Re-evaluation of the Cu-Zn System,” *J. Phase Equil.*, vol. 14, pp. 432–438, 1993.

[32] B. E. Warren and E. P. Warekois, “Stacking Faults in Cold Worked Alpha-Brass,” *Acta Metallurgica*, vol. 3, no. 5, pp. 473–479, 1955.

[33] C. N. J. Wagner, “Stacking Faults by Low-Temperature Cold Work in Copper and Alpha Brass,” *Acta Metallurgica*, vol. 5, no. 8, pp. 427–434, 1957.

[34] R. E. Smallman and K. H. Westmacott, “Stacking Faults in Face-Centered Cubic Metal and Alloys,” *Philisophical Mag.*, vol. 2, no. 17, pp. 669–683, 1957.

[35] L. Ajdelsztajn et al., “Cold-spray processing of a nanocrystalline Al-Cu-Mg-Fe-Ni Alloy with Sc,” *Journal of Thermal Spray Technology*, vol. 15, no. 2, pp. 184–190, June 2006.

[36] A. C. Hall, L. N. Brewer and T. J. Roemer, “Preparation of Aluminum Coatings Containing Homogenous Nanocrystalline Microstructures Using the Cold Spray Process,” *Journal of Thermal Spray Technology*, vol. 17, no. 3, pp. 352–259, April 2008.

[37] Y. Y. Zhang et al., “Cold-Spray Processing of a High Density Nanocrystalline Aluminum Alloy 2009 Coating Using a Mixture of As-Atomized and As-Cryomilled Powders,” *Journal of Thermal Spray Technology*, vol. 20, no. 5, pp. 1125–1132, Sept. 2011.

[38] J. Liu et al., “Tribological behavior of cold-sprayed nanocrystalline and conventional copper coatings,” *Applied Surface Science*, vol. 258, pp. 7490–7496, 2012.

[39] E. J. Lavernia, B. Q. Han and J. M. Schoenung, “Cryomilled Nanostructured Materials: Processing and Properties,” *Materials Science Engineering A*, vol. 493, no. 1–2, p. 207, 2008.

[40] H. Bahmanpour et al., “Mechanial behavior of bulk nanocrystalline copper alloys produced by high energy ball milling,” *Journal of Material Science*, vol. 46, pp. 6316–6322, 2011.

[41] J. Pattison et al., “Standoff distance and bow shock phenomena in the cold spray process,” *Surface & Coatings Technology*, vol. 202, pp. 1443–1454, 2008.

[42] E. Irissou et al., “Investigation of Al-Al2O3 cold spray coating formation and properties,” *Journal of Thermal Spray Technology*, vol. 16, no. 5–6, pp. 661–668, 2007.

[43] Centerline SST. (2012, Nov. 14). [Online Text]. Available: http://www.supersonicspray.com/en/products_full?pg=SE44500&rp=13.

[44] “Sieve and Composition Analysis,” ACu Powder, Union, NJ, by request, Nov. 14, 2012.

[45] A. L. McGinnis, “Diffusion Couple Alloying of Refractory Metals in Austenitic and Ferritic/Martensitic Steels,” M.S. Thesis, MAE Dept., Naval Postgraduate School, Monterey, CA, 2012.

[46] L. N. Brewer et al., “Residual stress distributions in the solid solution Eutectic $Co_{1-x}Ni_xO/ZrO_2(CaO)$,” *J. Am. Ceram. Soc.*, vol. 86, no. 12, pp. 2188–2194, 2003.

[47] M. Yandouzi et al., “WC-based cermet coatings produced by cold gas dynamic and pulsed gas dynamic spraying processes,” *Surface & Coatings Technology*, vol. 202, pp. 382–390, 2007.

[48] B. Jodoin et al., “Effect of particle size, morphology, and hardness on cold gas dynamic sprayed aluminum alloy coatings,” *Surface & Coatings Technology*, vol. 201, pp. 3422–3429, 2006.

[49] *ASM Handbook, Vol. 2*, 9th Ed., ASM International, Materials Park, OH, 2012, pp. 274–300.

[50] J. D. McKinley and J. E. Vance, “The vapor pressure of zinc between 150° and 300°C,” *Journal of Chemical Physics*, vol. 22, pp. 1120–1124, 1954.

[51] J. Liu et al., “Tribological behavior of cold-sprayed nanocrystalline and conventional copper coatings,” *Applied Surface Science*, vol. 258, pp. 7490–7496, 2012.

INITIAL DISTRIBUTION LIST

1. Defense Technical Information Center
   Ft. Belvoir, Virginia

2. Dudley Knox Library
   Naval Postgraduate School
   Monterey, California

3. Prof. Nathaniel Luke Brewer, MAE Dept.
   Naval Postgraduate School
   Monterey, California

4. Prof. Knox T. Millsaps, Chairman, MAE Dept.
   Naval Postgraduate School
   Monterey, California

5. Program Officer, MAE Dept.
   Naval Postgraduate School
   Monterey, California